THE APPLICATION OF ECCENTRIC ROTATING CYLINDER APPARATUS FOR THE IMPROVED STUDY OF PARTICLE COAGULATION

A Thesis

by

CHUN WOO LEE

Submitted to the Office of Graduate Studies of
Texas A&M University
in partial fulfillment of the requirements for the degree of

MASTER OF SCIENCE

August 2003

Major Subject: Civil Engineering

THE APPLICATION OF ECCENTRIC ROTATING CYLINDER APPARATUS FOR THE IMPROVED STUDY OF PARTICLE COAGULATION

A Thesis

by

CHUN WOO LEE

Submitted to Texas A&M University
in partial fulfillment of the requirements
for the degree of

MASTER OF SCIENCE

Approved as to style and content by:

Timothy A. Kramer (Chair of Committee)	Bill Batchelor (Member)
George Jackson (Member)	Paul N. Roschke (Head of Department)

August 2003

Major Subject: Civil Engineering

ABSTRACT

The Application of Eccentric Rotating Cylinder Apparatus

for the Improved Study of Particle Coagulation. (August 2003)

Chun Woo Lee, B.S., Pukyung National University, Korea

Chair of Advisory Committee: Dr. Timothy A. Kramer

Concentric rotating cylinder and turbulent mixing devices have been frequently used in studying mixing and particle coagulation. However, these apparatus develop simple laminar flow (concentric rotating cylinders) or do not have well-defined flow (turbulent mixing devices). In this work, the eccentric rotating cylinder apparatus was investigated to find applicability for the improved study of coagulation based on the modified analytical solution of Ballal and Rivlin.

Various eccentricity ratios, rotation speeds and viscosities were simulated to obtain optimum operating conditions. Inertial forces working on the fluid increased as the eccentricity ratio and rotation speed increase. As inertial forces increase, the eddy developed in wide clearance was more skewed in the direction of rotation. Both root-mean-square velocity gradient ($\overline{G}$) and average principal strain–rate ($\overline{|a_{\max}|}$), were increased by increasing eccentricity ratio. $\overline{|a_{\max}|}$ values linearly increased as rotation speed increases, which suggested that $\overline{|a_{\max}|}$ value can properly represent mixing intensity. Comparison of $\overline{G}$ and $\overline{|a_{\max}|}$ revealed that $\overline{G}$ overestimated mixing intensity and its error increased as eccentricity ratio increases.

This study showed that the eccentric rotating cylinder apparatus has a non-uniform velocity distribution with well-defined fluid dynamics. Therefore, the eccentric rotating cylinder apparatus can be applicable as a model flocculator. However, in order to achieve reliable model predictability, the fluid Reynolds number must be below 200.

DEDICATION

This thesis is dedicated to my parents, brother, and wife, for their faith, enthusiasm, and enduring support, especially my father who always watches me in heaven.

ACKNOWLEDGMENTS

I wish to acknowledge my advisor, Dr. Kramer. You have shown great patience, support and enthusiasm, and I truly appreciate all the advice and discussion. Once you told me when I was in trouble in my research “Don’t give up and keep trying”. This became my motto in graduate school life. I also would like to extend my sincere thanks to Dr. Batchelor and Dr. Jackson for serving on my committee and offering helpful comments.

I would like to express my appreciation to my friends for their assistance and friendship in the classroom, laboratory and tennis court. My special thanks to Jinwook Kim, it was great fun discussing colloid world and sometimes talking about life over a beer. He always gave good advice, like an older brother.

I would like to thank my mother, brother, mother and father-in-law for their encouragement and support. Finally, I wish to thank my lovely wife, Jungyun. I would like to say “I love you, Jungyun and your love makes everything worthwhile. My son Landon, I love you too.”

TABLE OF CONTENTS

LIST OF FIGURES

FIGURE Page

LIST OF TABLES

NOMENCLATURE

P = Perimeter of the projected area of an aggregate

n = Number density of the particles

G = Root-mean-square velocity gradient

E = The rate of deformation (strain-rate)

A = Projected area of an aggregate

r_i = Radius of an *i* class particle

r_j = Radius of an *j* class particle

r_k = Radius of an *k* class particle

r_m = Moving particle radius

r_s = Stationary particle radius

r_t = Total radius by adding moving particle radius and stationary particle radius

$\frac{du}{dx}$ = Local velocity gradient or strain-rate

$\overline{G}$ = Global root-mean-square velocity gradient

∇u = Velocity gradient tensor

$(\nabla u)^T$ = Transposes of velocity gradient tensor

Ω = Vorticity

d_f = Longest width of an aggregate

V_f = Floc volume

D_1 = One-dimensional fractal dimension

D_2 = Two-dimensional fractal dimension

D_{pf} = Perimeter based two-dimensional fractal dimension

D_3 = Three-dimensional fractal dimension

S_{d_f} = Exponents of the cumulative size distribution based on aggregate width

S_{V_f} = Exponents of the cumulative size distribution based on aggregate volume

u_θ = Tangential velocity

u_r = Radial velocity

ω_i = Angular velocity of the inner cylinder

ω_o = Angular velocity of the outer cylinder

R_i = Inner cylinder radius

R_o = Outer cylinder radius

$\tau_{r\theta}$ = Shear stress in cylindrical coordinates

$a_{r\theta}$ = Shear strain-rate in cylindrical coordinates

T = Torque

P_W = Mechanical power required to turn the cylinder

μ = Dynamic viscosity

T_a = Taylor number

ν = Kinematic viscosity

V_T = System volume

$\overline{\Phi}$ = Mean shear energy dissipation function

ε = Turbulent energy dissipation rate

N_p = Impeller power number

D = Impeller diameter

β = Collision frequency function

$\psi(x, y)$ = Lagrange's stream function

∇^2 = Laplace operator

$\psi^{(0)}$ = Stokes stream function neglecting the inertial forces

$\psi^{(1)}$ = Stream function with inertial effects

ξ = Radial direction in bipolar coordinates

η = Angular direction in bipolar coordinates

e = Eccentricity

$a_{\xi\xi}$ = Normal component of the strain-rate tensor in bipolar coordinates

$a_{\xi\eta}$ = Shear component of the strain-rate tensor in bipolar coordinates

$a_{\eta\xi}$ = Shear component of the strain-rate tensor in bipolar coordinates

$a_{\eta\eta}$ = Normal component of the strain-rate tensor in bipolar coordinates

$a'_{\max}$ = Local principal strain-rate

$\overline{\tau^{(0)}}$ = Average shear stress on the outer cylinder for Stokes flow

$\lambda^{(0)}$ = Dimensionless function of inner and outer cylinder radius for Stokes flow

$\lambda^{(1)}$ = Dimensionless function of inner and outer cylinder radius for inertial flow

C = Mean clearance ($C = R_o - R_i$)

CHAPTER I

INTRODUCTION

Colloidal matter, which cannot be readily removed, exists in most water resources, including groundwater. In water and wastewater treatment, particle separation is vital to meet drinking water and water effluent quality regulations. As a pretreatment followed by sand filtration, sedimentation, or recently membrane filtration, flocculation has been used to increase the size of colloid particles. Flocculation can be subdivided into three mechanisms, perikinetic, differential sedimentation, and orthokinetic. Perikinetic flocculation is induced by Brownian particle motion. The perikinetic mechanism is dominant when diameters of particles are less than 1 μm. Differential sedimentation occurs due to particles settling with different velocities, because they have different size or density. This causes particle collisions. Orthokinetic flocculation is induced by fluid motions and is the most important mechanism in the water treatment process.

Orthokinetic flocculation is the growth of floc aggregates generated by flow induced collisions of smaller particles suspended in the fluid. The most common way to initiate destabilization and aggregation of particles is to add coagulant chemicals, which reduce the electrostatic double layer repulsive forces. Particle destabilization is followed by agitation to induce particle collisions. Aggregate characteristics in flocculation are affected not only by the chemical composition of the fluid such as ionic strength and pH,

---

This thesis is follows the style and format of *Journal of Environmental Engineering*.

but also by the dynamic properties of the fluid such as local velocity gradients or strain-rates, which are characteristics of the fluid motions. In other words, exact analysis of flow dynamic conditions must be known to properly examine flocculation and develop predictive capability.

Many experimental devices have been used to study orthokinetic flocculation. Representative apparatus include rotating impellers, which generate turbulent flow and concentric rotating cylinders, which generate homogeneous laminar flow. However, rotating impeller mixers do not have a well-characterized flow. The concentric rotating cylinder apparatus generates a laminar shearing flow, which is very simplistic.

A method to create a more realistic and characterized flow is to eccentrically locate the inner cylinder in the rotating cylinder apparatus. This device has the unique feature of developing spatially varying flow while having a known analytical solution to predict the flow behavior. Use of the eccentric rotating cylinder apparatus originated from lubrication experiments in fluid dynamics for investigating journal bearing problems. The apparatus can generate pressure gradients,and eddies in the region of the largest clearance, can have shear and extensional flow coexist, and can display spatially varying dynamic conditions. Ballal and Rivlin (1976) derived exact solutions for velocities, pressures, and streamlines for the eccentric geometry with and without inertial forces. These spatially varying flow conditions are more realistic than concentric rotating cylinders and have better characterized flow than a rotating impeller mixer, i.e. a known analytical solution for the fluid motion. However, complete verification of their solutions by comparison of experiment and simulation has not been conducted. Further,

investigations of orthokinetic coagulation using the eccentric device has not been conducted. The objective of this thesis is the development and application of the eccentric rotating cylinder apparatus for the improved study of particle flocculation. To approach more realistic conditions, analytical solutions with and without inertial terms will be analyzed with changing angular velocity, inner cylinder radius, and eccentricity. These comparisons will verify the accuracy of Ballal and Rivlin's analytical solutions and provide methods to produce a more realistic model flocculator. Based on these analytical solutions, fluid velocity, strain-arte, and Camp and Stein's velocity gradients are obtained by modifying stream functions. Computed streamlines will be presented and compared to experimental data in a physical device. Finally, optimum operating conditions will be presented for future work using the eccentric rotating cylinder apparatus in flocculation.

To achieve these goals, a rigorous review of the relevant literature in the subject area will be presented. This includes problems associated with velocity gradients, particle breakup, and fractal dimension investigations using conventional apparatus, concentric cylinders and rotating impellers. The characteristics of each type of flow will be compared to approach more realistic turbulent conditions. Analytical solutions derived by Ballal and Rivlin will be modified to obtain information related to strain-rate distributions and velocity gradients. To investigate the validity of the analytical solutions of Ballal and Rivlin streamlines, generated using different eccentricity ratios, angular velocities, and inner cylinder radiuses will be compared with model results.

CHAPTER II

BACKGROUND

2.1 Introduction

Flocculation modeling was suggested by Smoluchowski (1917), who proposed two flocculation mechanisms, perikinetic and orthokinetic flocculation. Diffusive movements of colloid particles, termed Brownian motion, induce perikinetic flocculation. Orthokinetic flocculation is the growth mechanism of aggregates or floc by flow induced particle collisions. In engineering practices, orthokinetic flocculation is used to produce larger aggregates and facilitate separation from the fluid by sedimentation and/or filtration. The kinetic equation of Smoluchowski for orthokinetic flocculation is given as

$$\left(\frac{dn_k}{dt}\right) = \frac{1}{2}\sum_{i+j=k}\frac{4}{3}\frac{du}{dx}(r_i + r_j)^3 n_j n_i - \sum_{j=1}^{\max}\frac{4}{3}\frac{du}{dx}(r_j + r_k)^3 n_j n_k \qquad (1)$$

where r_i, r_j and r_k refer to the radius of i, j, and k class particles, n is number density of the particles, and du/dx is a local velocity gradient or strain-rate. The first equation on the right hand side is the rate of increase in particle size k by flocculation with particle sizes i and j. The second term on the right hand side is the rate of decrease in particle size k by flocculation with particle size j and k. Equation (1) assumes that all primary particles are perfect spheres. The aggregates formed are assumed to be spherical, no aggregates breakup, and all particle collisions lead to attachment and aggregate growth by neglecting particle interactions.

In recent years, particular progresses concerning aggregate morphology, breakup, hydrodynamic interactions, and fluid flow induced particle collisions have been made to improve Smoluchowski's assumptions. Smoluchowski assumed that when two different particles with radii of r_i and r_j, collide the resulting radius of the aggregate is $r_k = (r_i^3 + r_j^3)^{1/3}$. This is called droplet coalescence. However, in reality most aggregates formed in nature and by engineered processes have irregular geometries and porosities, which mean that the assumption of droplet coalescence underestimates real aggregate size (Gmachowski, 2000). Instead of assuming perfect spheres for the primary particles and aggregates, fractal dimensions were introduced to describe morphology and spatial structure of aggregates. Equation (1) indicates that particles collide and form aggregates without breakup. However, numerous investigations have shown that aggregates are eroded or fragmented into smaller sized particles and, that breakup plays an important role in determining particle size distribution. Thus, in order to consider aggregate breakup in coagulation modeling, breakup kinetics and a maximum aggregate size were introduced. Particle collisions and attachment with and without various interactive forces around colliding particles have been investigated with curvilinear and rectilinear models as shown in Fig. 1. Smoluchowski's assumption neglecting particle interactions is rectilinear model. The rectilinear model assumes that when a moving particle of radius, r_m, passes within the radius, $r_t = r_m + r_s$, the particle will collide with stationary particle (r_s). However, streamlines passing circular cylinder showed that hydrodynamic interactions between moving and stationary particles can affect particle collisions

(Batchelor, 1967). The curvilinear model takes account of these interactive forces in particle collisions. The curvilinear model assumes that even if the moving particle (r_m)passes within $r_t = r_m + r_s$, not all particles will collide with the stationary particle (r_s). Finally, particle collisions induced by two-dimensional laminar shearing motion were developed to consider multi-directional fluid strain-rate. Kramer and Clark (1997)

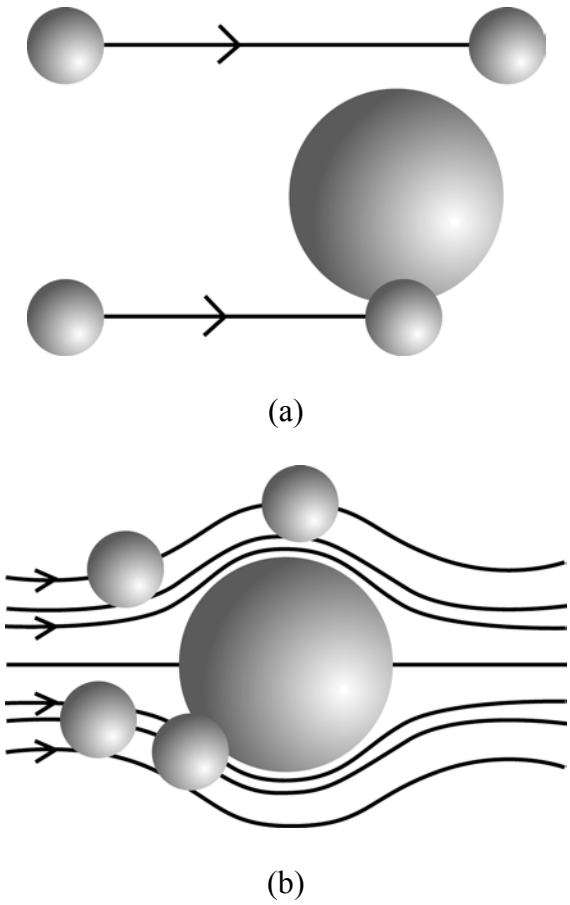

FIG. 1. Particle Collision Models with Hydrodynamic Interactions: (a) The Classical Rectilinear Model; (b) The Curvilinear Model

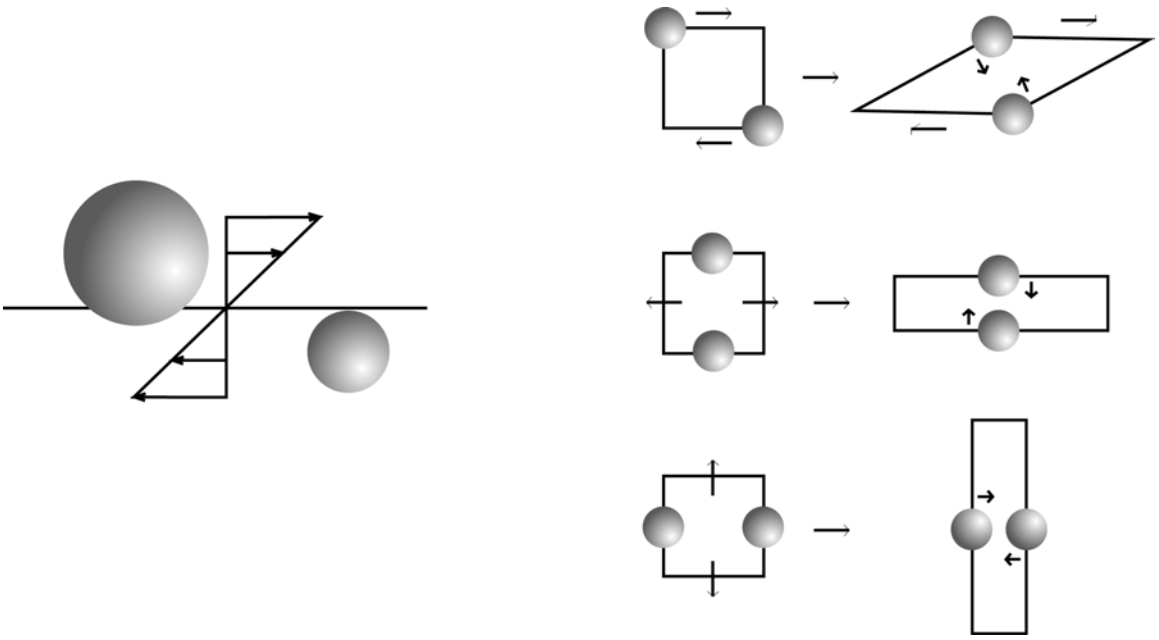

(a) (b)

FIG. 2. Flow Induced Particle Collisions: (a) Particle Collisions under Two-dimensional Laminar Shear Strain-rate; (b) Multidirectional Particle Collisions by Shear and Normal Strain-rate (Kramer and Clark, 1997)

suggested that particle collisions are induced by fluid strain-rate as presented in Fig. 2. Among the current developments, the analysis of particle collisions, aggregate breakup, and fractal dimension are known to be highly dependent on the fluid dynamics of the flocculation system. The next chapter will review the fluid dynamic effects on aggregation, aggregate breakup and morphology, and discuss the problems of conventional flocculation system for studying particle aggregation.

2.2. General Description of Orthokinetic Coagulation

2.2.1 Flow Induced Particle Agglomeration

Fluid motion associated with othokinetic flocculation can be described by the local velocity gradient or strain-rate. When one particle approaches a stationary particle, fluid shearing motions induce particle collisions. However, two-dimensional shearing motion only considers one directional particle movement and cannot explain complicated particle collisions. Camp and Stein (1943) conducted a three-dimensional analysis on velocity gradient's role in particle collisions based on shearing motions of fluid. Camp and Stein suggested that energy consumed by the fluid shearing movement is dissipated as heat. Thus, an absolute velocity gradient, G, is obtained using energy dissipation with system fluid volume for laminar flow. Camp and Stein hypothesized that a local velocity gradient (*du/dx*) was equivalent to their absolute velocity gradient, G. However, the practical flocculator contains turbulent flow, which has a more complicated and spatial varying velocity gradient distributions. To overcome complexity of fluid flow, Camp and Stein introduced defined their root-mean-square velocity gradient, $\overline{G}$.

Many studies have revealed that $\overline{G}$ does not accurately estimate velocity gradient on particle collisions in flocculators both theoretically and experimentally. Cleasby (1984) pointed out the deficiency of $\overline{G}$ for turbulent flow conditions by analysis of turbulent motions, especially studied use of absolute viscosity for $\overline{G}$. Comparisons of previous studies revealed that $\overline{G}$ is only applicable to laminar flow and limited cases of turbulent flow in which the size of the aggregate is smaller than the

Kolmogoroff microscale. Clark (1986) examined tensor approaches and found that application of an absolute velocity gradient, G, and root-mean-square velocity gradient, $\overline{G}$, into three-dimensional flow is fundamentally incorrect. Graber (1994) showed that energy dissipation is not a function of only shear stress, but functions of both normal and shear stress. Kramer and Clark (1997) examined effects of the strain-rate on particle collisions and the effects of the spatial flow variance on average velocity gradient. Kramer and Clark showed that distorted fluid elements in which particles are located make particle collisions by shear and normal strain, but rotational motion affects only the orientation of the particle. Population variance investigation on root-mean-square velocity gradient showed that the error of $\overline{G}$ is more severe as spatial flow variance increases.

Experiments have been conducted comparing experimental data at the same $\overline{G}$ value with different geometries and mixing devices. Oldhsue and Mady (1978, 1979) examined turbidity removal with different types of mixing impellers at various impeller diameters and mixing tank diameter ratios. Their results indicated that maximum turbidity removal was accomplished at different $\overline{G}$ values, even though each impeller had the same configuration. Another investigation of turbidity removal with different impellers showed that impeller type is important in determining the optimum mixing intensity (McConnachie, 1991). Spicer et al. (1996) investigated average floc size with three different types of impellers: 1) ruston for generating radial flow having longer exposure time to high velocity gradients around the impeller blade, 2) a fluid foil impeller for generating axial flow, which produces a shorter exposure time to intensive

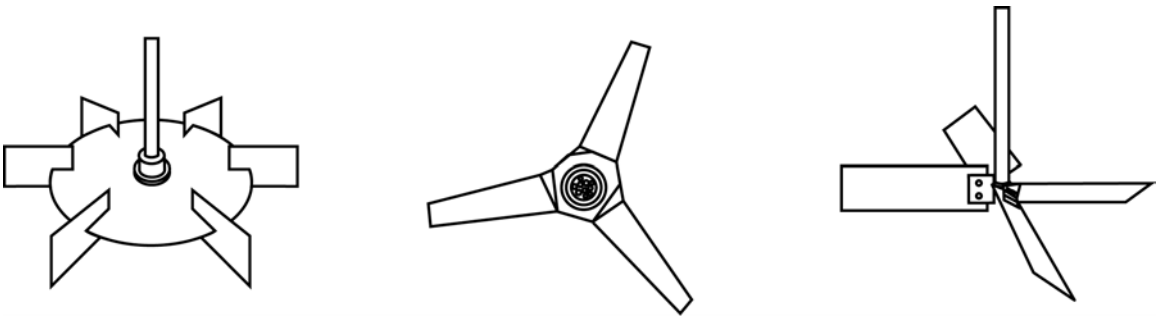

(a) (b) (c)

FIG. 3. Representative Types of Impellers for Flocculation: (a) Rushton Turbine (RT); (b) Fluid Foil Impeller (A310); (c) Pitched Blade Turbine (PBT)

velocity gradients, and 3) a four-blade impeller, which has axial and radial flow pattern as displayed in Fig. 3. They observed that aggregate size distributions were different for each impeller at constant $\overline{G}$ vaules. A310 fluid foil showed that smaller aggregates were produced with increasing flocculator volume. The ruston impeller produced smaller aggregates than the A310 fluid foil impeller (Ducoste and Clark, 1998). This result is in agreement with Spicer et al. (1996). Many investigators have recognized the problems of $\overline{G}$ in correlating mixing variables and flocculator geometries both theoretically and experimentally, however, most flocculation studies conducted have been based on root-mean-square velocity gradient. Because $\overline{G}$ provides a basis for comparison for previous studies, it continues to be applied to flocculation studies.

2.2.2 Flow Induced Aggregate Breakup

As the floc grow, they become susceptible to fluid stresses and possibly fracture into smaller aggregates. This floc breakup produces reduced sizes of aggregates which cause poor settlement in sedimentation and increased fouling in filtration processes. There are two perceived modes of particle breakup, surface erosion and fragmentation. Surface erosion of floc structure will occur when the weakest bonds are distributed on the periphery of the floc aggregate. The driving force for surface erosion is believed to be local shear stresses. Fragmentation can be caused by a distribution of the weak bonds within the body of the aggregate where the fragmenting force is due to pressure gradients or normal stresses (Thomas, 1964; Parker et al. 1972; Argaman and Kaufman, 1970; Blaser, 2000). The forces exerted on aggregates are dependent on the local fluid motions. According to Kramer and Clark (1997, 1999), the local velocity gradient induced by fluid motions affects not only particle collisions but also aggregate breakup. Thus, the analysis of the local fluid dynamic characteristics around particles is required to understand the complex aggregate breakup phenomena.

The motions of a local fluid element are described by the local velocity gradient tensor. The velocity gradient tensor (∇u) consists of the rate of deformation tensor and the rate of rotation material vector. The rate of deformation (E) called strain-rate is a symmetric tensor. The orientation of the material vector having rotational component or vorticity (Ω) has an antisymmetric form. If the Cartesian coordinates have two-dimensional components, x_l and x_m, the equations of velocity gradient (∇u), strain-rate (E), and vorticity tensor (Ω) are defined as

$$\nabla u = \frac{1}{2}\left(\frac{\partial u_l}{\partial x_m} + \frac{\partial u_m}{\partial x_l}\right) + \frac{1}{2}\left(\frac{\partial u_l}{\partial x_m} - \frac{\partial u_m}{\partial x_l}\right) \tag{2}$$

$$E = \frac{1}{2}\left(\nabla u + (\nabla u)^T\right) = \frac{1}{2}\left(\frac{\partial u_l}{\partial x_m} + \frac{\partial u_m}{\partial x_l}\right) \tag{3}$$

$$\Omega = \frac{1}{2}\left(\nabla u - (\nabla u)^T\right) = \frac{1}{2}\left(\frac{\partial u_l}{\partial x_m} - \frac{\partial u_m}{\partial x_l}\right) \tag{4}$$

where u_l and u_m represent x_l and x_m direction velocities respectively. The characteristics of the velocity gradient tensor are dependent on flow types. There are two representative flow motions; laminar flow and turbulent flow, which have been used to study aggregate breakup behavior and mechanisms. According to the ratio of strain-rate (E) and vorticity tensor (Ω), characteristics of flow are subdivided into pure shear and extensional flow. Pure shear flow can be generated using concentric rotating cylinders which consists of one stationary and one rotating cylinder either inner or outer cylinder or both cylinders rotating, or a plane Couette device in which there is fluid between two parallel plates that are moving in opposite directions. Since half of the fluid energy is consumed to the vorticity, shear flow can be called weak rotational flow and has a weak rate of deformation (Boller and Blaser, 1998). Pure extensional flow can be developed using a four-roll-mill device which was introduced by Taylor (1934). Pure extensional flow, called strong flow or irrotational flow, has no rotational component and strong deformation rate. Detailed derivations of velocity gradient, strain-rate, and vorticity tensors are presented in Appendix I.

Many studies have been reported about the behavior of aggregates in shear and extensional flow. Fig. 4 display aggregate breakup modes by shear flow conditions. The aggregate movements in shear flow show that the aggregate rotates with no deformation at a low velocity gradient, but as velocity reaches a critical point, the disintegration of the primary particle on the surface of the aggregate is observed. Surface erosion in shear flow is located at 45^{o} and 225^{o} planes on the aggregate surface. This is in an agreement with the maximum principal stress for shear flow (Kao and Mason, 1975; Powell and Mason, 1982; Boller and Blaser, 1998; Blaser, 2000). The angular velocity of aggregate rotation matched with (2) transforming half of the velocity gradient into a rotational component, or vorticity (Boller and Blaser, 1998).

The behavior of aggregates in the extensional flow shows more rapid disintegration (Kao and Mason, 1975). As shown in Fig. 5 Blaser (2000) presented the consecutive motions of breakup of aggregate in extensional flow and showed that floc does not rotate, but it is extended or compressed and fragmented into small aggregates. Fig. 6 shows consecutive motions of aggregates from Blaser (2000). Blaser explained that the first row of picture shows surface erosion but it appears to be more like aggregate fragmentation. Experimental observation (Kao and Mason, 1975) and simulation (Higashitani and Iimura, 1998) indicate that extensional flow is more disintegrate aggregates. Because extensional flow has irrotational characteristics, thus, energy from fluid motions is consumed only for material deformation.

Pure shear and extensional flow are components of instantaneous local flow, but turbulence is a macroscopic flow condition and possesses very complicated flow

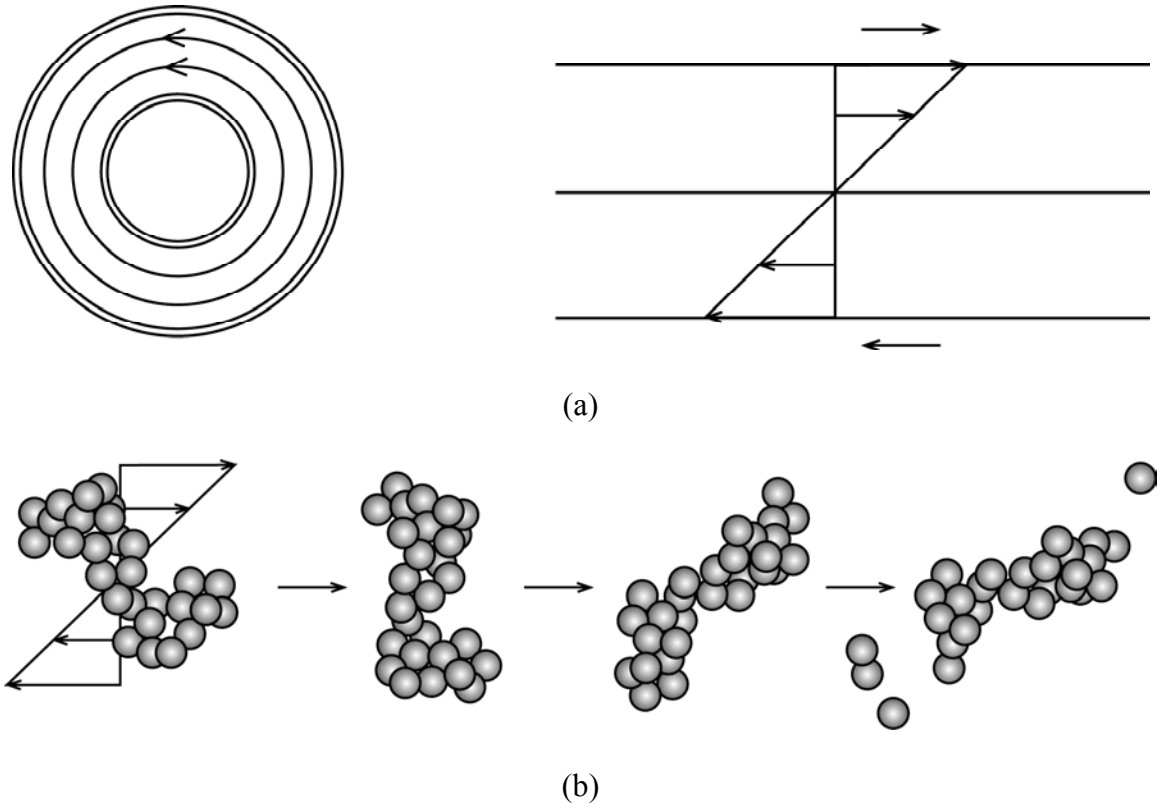

FIG. 4. Aggregate Behavior in Shear Flow: (a) Concentric Rotating Cylinder and Plane Couette Device; (b) Aggregate Movement in Shear Flow and Breakup

dynamics. Simulations of incompressible isotropic turbulent structure are presented in Fig. 7 and they showed four kinds of flow structure: rotation in eddies, convergence-divergence (extensional-compressional) zones, shear zones, and streams (Wray and Hunt, 1990). Eddies are whirl motions of flow in which fluid particles have a long retention time. Convergence-divergence zones contain compressional and extensional strain-rates without rotating fluid elements. Shear zones consist of shear strain-rates and rotational

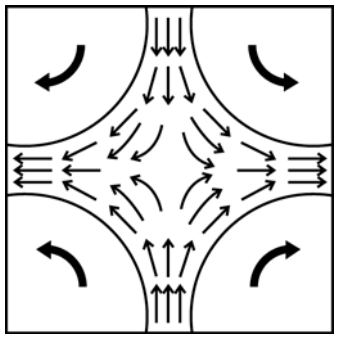

(a)

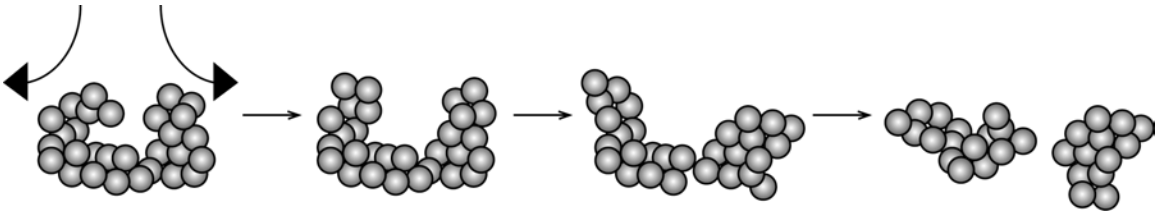

(b)

FIG. 5. Aggregate Behavior in Extensional Flow: (a) Four-Roll-Mill Device; b) Aggregate Movement in Extensional Flow and Breakup

vorticity without interchanging flow. Streams show weak strain-rates and irrotational characteristics. Dominant stresses on fluid particles for each flow showed that convergent-divergent and shear flow have normal and shear strain-rates, and rotation in eddies have vorticity. Among these stresses, only two of them, normal and shear strain-rate, work on particle collisions as the driving forces (Kramer and Clark, 1997). Particle rotation does not influence particle collisions. It only affects the orientation of

aggregates (Kramer and Clark, 1997), and has an insignificant effect on aggregate deformation and breakup (Thomas, 1964).

Many investigators have proposed different mechanisms for aggregate breakup mode in turbulent flow, which determines particle size distributions. Argaman and Kaufman (1970) suggested that the fundamental aggregate breakup mechanism in turbulent flow is the surface erosion of flocs by fluid surface shearing movements. Parker et al. (1972) reported that Argaman and Kaufman's proposal is more reasonable in the case of biological floc than aggregate fragmentation. Experiments using a flow chamber to observe aggregate breakup showed that disintegration of aggregates is distributed on the periphery of the floc, which is believed to be surface erosion (Glasgow and Liu, 1991). Thomas (1964) suggested that aggregate fragmentation in turbulent flow is caused by pressure gradients on opposite sides of the aggregate. Kramer and Clark (1999) used a system of classification of mechanical failure to describe aggregate breakup by assuming that breakup of aggregates is caused by flow induced stress. Kramer and Clark proposed that the principle mode of aggregate breakup is fragmentation by normal stress. Boller and Blaser (1998) compared behaviors and stress distribution on the surface of an aggregate in simple shear and extensional flow. Boller and Blaser suggested that the fragmentation of aggregates caused by normal stress plays a crucial role in determining particle size distribution in turbulent flow.

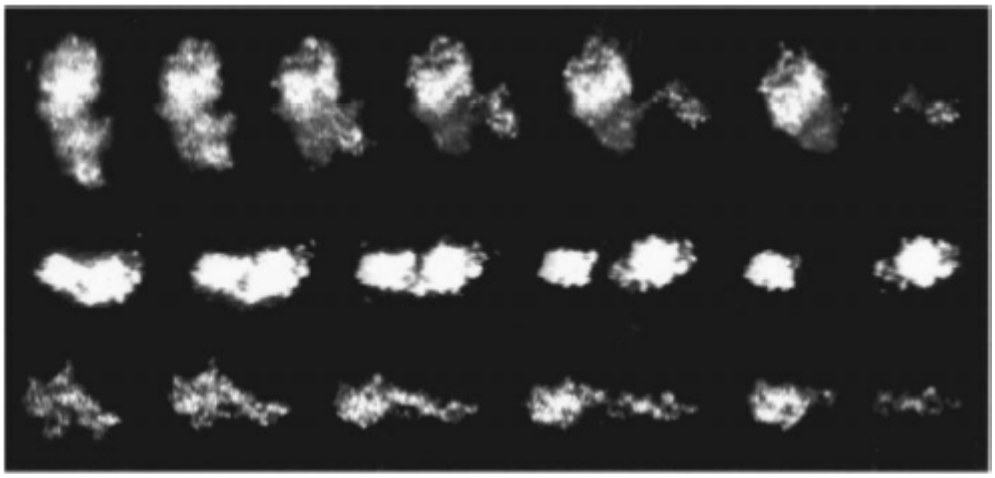

FIG. 6. Breakup of Ferric Hydroxide in a Two-dimensional Extensional Flow (Blaser, 2000)

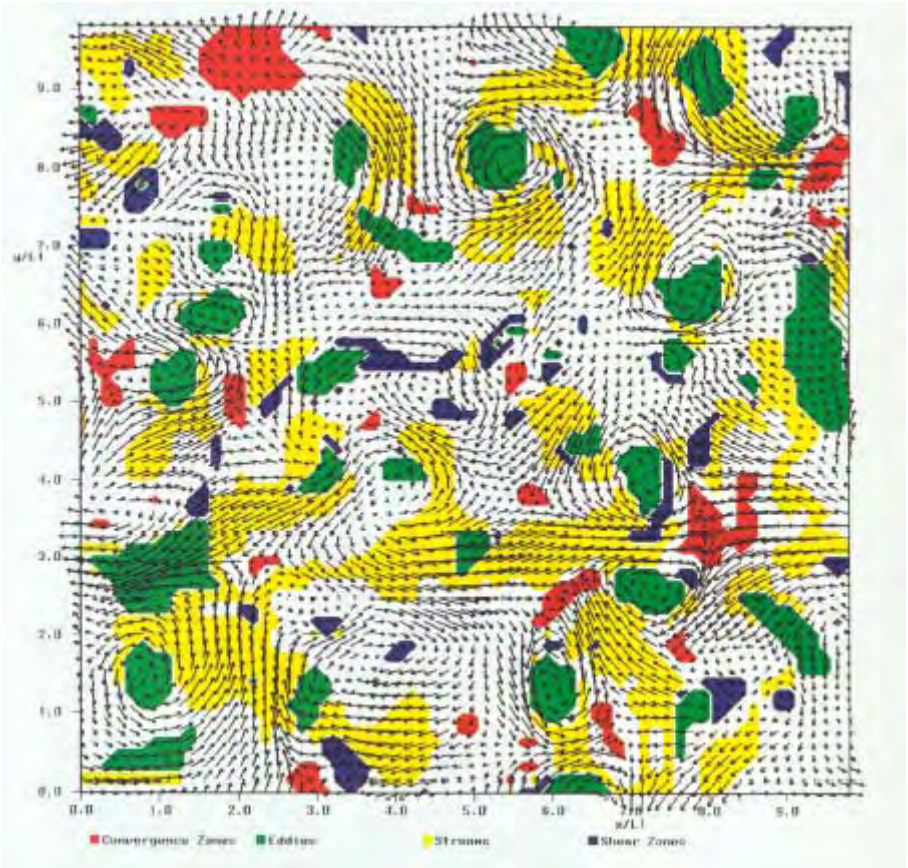

FIG. 7. Turbulent Structure Classification (Wray and Hunt, 1990)

2.2.3 Geometric Description of an Aggregate

Aggregate geometric structure has been recognized to influence the strength of floc and their potential for breakup. Therefore, characterization of floc or aggregate geometry is required to understand particle collisions and flocculation. However, it was very difficult to define the geometric characteristics of aggregates due to their highly irregular and disordered shape. Attempts to quantify the geometry of aggregates using a shape factor, porosity, or settlement velocity were not sufficient to describe the complex shapes and spatially varying structures of aggregates.

Fractal theory developed by Mandelbrot (1983) made it possible to characterize geometric irregularity and complexity. Mandelbrot introduced a non-integer dimensional value called the fractal dimension to describe mathematically complex and irregular geometric characteristics in nature such as the branches of trees, coastlines, and clouds. The geometry of aggregates also shows a highly irregular, complex, and disordered shape. Fractal dimensions of flocs have been reported to be able to characterize mass-size relationships, density, porosity, irregularity and settling velocity (Jiang and Logan, 1996; Meakin, 1998).

The measurements of fractal dimension of a system are obtained from geometric properties of aggregates. The longest width (d_f), perimeter (P), projected area (A), floc volume (V_f), and number density (N) are used to express one-dimensional (D_1), two-dimensional (D_2), two-dimensional perimeter based (D_{pf}), and three-dimensional (D_3), fractal dimensions as described in Fig. 8. The equation for determination of a one-dimensional fractal is shown as

$$P \propto d_f^{D_1} \tag{5}$$

Regular perimeters such as squares and circles, termed Euclidean objects, show D_1 is equal to one. However, floc aggregates present higher D_1 values than Euclidean objects, which means D_1 can represent irregular characteristics of the aggregate perimeter. Two-dimensional and perimeter based fractal dimensions can be expressed as

$$A \propto d_f^{D_2} \tag{6}$$

$$A \propto P^{D_{pf}} \tag{7}$$

Two-dimensional fractal dimension of Euclidean objects is equal to two. D_2 and D_{pf} can represent structures of floc aggregates such as porosity, settling velocity, and density. D_1, D_2, and D_{pf} can be measured with image analysis systems. Three-dimensional fractal dimension can be expressed as

$$V_f \propto d_f^{D_3} \text{ or } N \propto d_f^{D_3} \tag{8}$$

Meakin (1988) suggested that if the D_3 value is less than 2, then D_2 and D_3 must be the same. However, Jiang and Logan (1996) showed that this is not always the same. Jiang and Logan presented the two-slope method to more accurately quantify three-dimensional fractal dimensions. Since there is difficulty in determining steady state conditions during coagulation, the longest width and volume based cumulative size distribution is used to quantify D_3. Three-dimensional fractal dimension with the two-slope method can be shown as

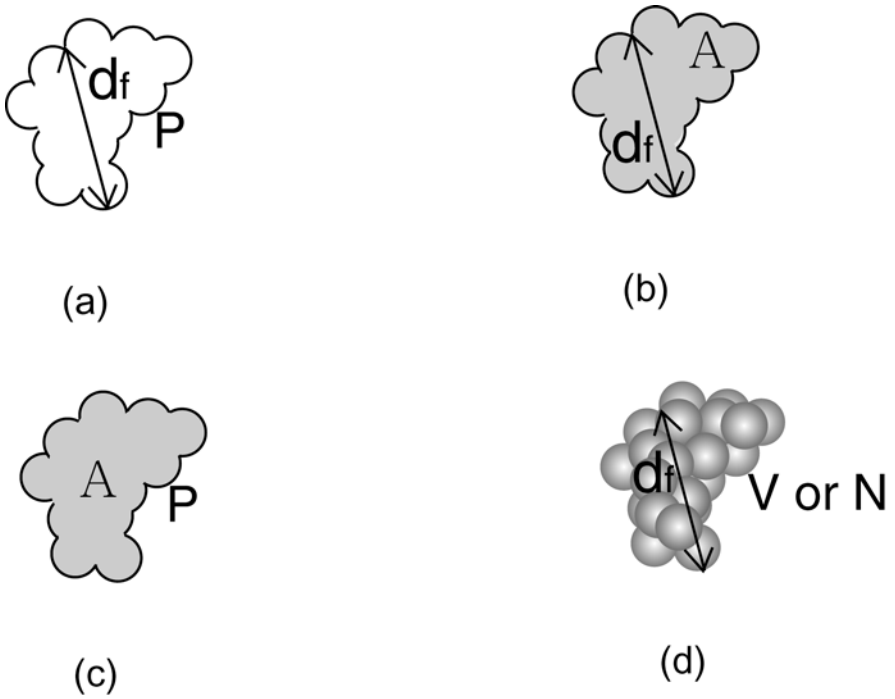

FIG. 8. Schematic Picture of Aggregate Fractal Dimensions: (a) One-Dimensional Fractal Dimension (D_1); (b) Two-Dimensional Fractal Dimension (D_2); (c) Perimeter-Based Fractal Dimension (D_{pf}); (d) Three-Dimensional Fractal Dimension (D_3)

$$D_3 = \frac{S_{d_f}}{S_{V_f}} \tag{9}$$

in which S_{d_f} and S_{V_f} represent the exponents of the cumulative size distribution based on aggregate width and volume. Detailed analysis of the two-slope method can be found in Jiang and Logan (1991, 1996)

Aggregate fractal dimensions during coagulation depend on the types of coagulant, pH, and mixing intensity. Different coagulants and pH values generate

various fractal values (D_3), in the range of 1.64 ~ 1.95 (Smoczynski and Wardzynska, 1996). It is well known that ionic strength, which is controlled by the amount of coagulant, plays a crucial role in determining fractal dimension. Diffusion-Limited-Aggregation (DLA) in which there is sufficient ionic strength to suppress repulsive forces, shows lower density structures with fractal dimensions around 1.7~1.8 (Lin et al., 1989). Reaction-Limited-Aggregation (RLA) in which there is insufficient ionic strength to suppress repulsive force, thus, strong repulsive forces exist, shows higher density and fractal dimension is around 2.0~2.1 (Meakin, 1988; Lin et al., 1989). In orthokinetic coagulation, fractal dimensions are highly dependent on the system mixing intensity, which is determined by the fluid dynamic conditions of the flocculator. Experiments using concentric rotating cylinders, which generate homogeneous laminar shear flow, showed that at shear strain-rate range of 25~50 $\sec^{-1}$ fractal dimensions do not change with increasing $\overline{G}$ (Oles, 1992; Serra and Casamitjana, 1998). However, turbulent mixing conditions (which develop intensive fluid movements around the blade) showed that fractal dimensions increased as $\overline{G}$ increased even at a low range of 15~50 $\sec^{-1}$ (Spicer et al., 1996). At higher $\overline{G}$ range over 60~150 $\sec^{-1}$, fractal dimensions slightly increased in concentric rotating cylinders (Oles, 1992), but turbulent devices showed a clearly increasing tendency of fractal dimensions (Gruy, 2001; Thill et al., 2001). Clark and Flora (1991) showed that introducing breakup process between flocculation and reflocculation can generate improved particle density structure and fractal dimension.

2.2.4 Summary

Since the introduction of Smoluchowski's coagulation equation (1), many investigations have been conducted to understand particle collision mechanisms and how they are affected by velocity gradients, aggregate breakup and fractal dimensions. The studies of velocity gradients, aggregate breakup, and fractal dimensions showed that if a flocculation system has well-defined fluid dynamics, more realistic flocculation models may be developed. For example, the study of Kramer and Clark (1997) applied the maximum strain-rate to describe fluid motions that generate particle collisions. However, the investigation of Kramer and Clark is a theoretically based hypothesis and has not yet been proven experimentally. The studies of aggregate breakup conducted with indirect methods using a flow chamber, photographic observation, and particle size distributions, have been carried out without calculating exact in-site stresses exerted on aggregates. Fractal dimension studies showed that the geometry of floc aggregates is highly dependent on mixing intensity and system fluid dynamics. However, since it is difficult to obtain a well-defined fluid dynamic conditions in a coagulation system, inappropriate estimates such as Camp and Stein's root-mean-square velocity gradient are used to represent mixing intensity and fluid dynamic conditions. Therefore, a model flocculator system that has well-defined fluid dynamics and more realistic flow conditions i.e. spatial variations, is required to achieve a better understanding of particle collisions and aggregation.

2.3 Conventional Flocculation System

2.3.1 Concentric Rotating Cylinders

Concentric rotating cylinders have been frequently used in studying mixing and flocculation in two-dimensional laminar flow. Hubley et al. (1950) used a concentric cylinder device (which has an outer cylinder rotation and stationary inner cylinder configuration) in order to generate reproducible conditions under which particles can undergo collisions. Trevelyan and Mason (1951) used a concentric cylinder device in which the outer and inner cylinders were rotated in opposite directions. This system made it possible to observe particle behavior in shear flow with a microscope as the opposite rotation of the two cylinders holds particles stationary within the field of vision of the microscope while applying shear stress on the particle surface. Swift and Friedlander (1964) applied a configuration with stationary outer cylinder and rotating inner cylinder to generate simple shear flow in order to validate Smoluchowski's equations by predicting flocculation in simple shear flow. Smith and Kitchener (1978) used a concentric rotating cylinder device for measuring the strength of floc, because the apparatus can provide predictable shear stress in laminar flow. To evaluate the efficiency of orthokinetic flocculation for fixed bed and fluidized bed flocculators, Ives and Dibouni (1979) applied the concentric cylinder device to acquire well-defined velocity gradients. Zollars and Ali (1986) applied the concentric rotating cylinder apparatus (which had rotating outer cylinder rotation and stationary inner cylinder) in order to provide sufficient shear stress and initiate flocculation in the presence of repulsive forces.

Extensive developments of the concentric rotating cylinder configurations for orthokinetic coagulation studies were conducted by van Durren (1968). The flow between two rotating cylinders (or one rotating and one stationary) is referred to as axisymmetric torsional flow. This torsional flow has a nonzero tangential velocity (u_θ) and two zero velocity components, (u_r) and (u_z). The streamlines of concentric rotating cylinder flow are circles centered at the axis of symmetry. Fig. 9 displays the geometry of the concentric rotating cylinder apparatus. From the definition of axisymmetric flow conditions ($\partial u_\theta / \partial \theta = 0$) the continuity equation for incompressible flow in cylindrical coordinates can be expressed as

$$\frac{1}{r}\frac{\partial}{\partial r}(ru_r)+\frac{1}{r}\frac{\partial u_\theta}{\partial \theta}+\frac{\partial u_z}{\partial z}=0 \tag{10}$$

The momentum equations for the tangential component can be simplified as

$$\frac{d}{dr}\left(\frac{1}{r}\frac{d}{dr}(ru_\theta)\right)=0 \tag{11}$$

The boundary conditions are given as

$$u_\theta = \omega_i R_i \text{ at } r = R_i,$$

$$u_\theta = \omega_o R_o \text{ at } r = R_o$$

By solving the simplified Navier-Stokes equations (momentum equations) with boundary conditions, general solutions for the flow can be obtained. These solutions for the configuration with rotating outer cylinder rotation and stationary inner cylinder configuration are given as

$$u_\theta = \frac{R_o^2 \omega_o}{R_o^2 - R_i^2}\left(r - \frac{R_i^2}{r}\right) \tag{12}$$

$$\tau_{r\theta} = 2\mu \frac{R_i^2 R_o^2}{R_o^2 - R_i^2}\omega_o \frac{1}{r^2} \tag{13}$$

$$\overline{G} = \frac{1}{R_o - R_i}\int_{R_i}^{R_o}\left(\frac{du_\theta}{dr} - \frac{u_\theta}{r}\right)dr = \frac{2\omega_o R_i R_o}{R_o^2 - R_i^2} \tag{14}$$

In equations (12) and (14), R_i is the inner cylinder radius, R_o outer cylinder radius, ω_o is angular velocity of outer cylinder, μ is viscosity, and r is radial distance. Due to axisymmetric flow conditions, normal stress ($\tau_{\theta\theta}$ and τ_{rr}) and radial direction velocity (u_r) are negligible.

Instead of using the difference between the rate of change in velocity and the relative particle velocity to calculate root-mean-square velocity gradient Kramer and Clark (1997) obtained root-mean-square velocity gradients with power input using local flow strain-rate. The shear strain-rate, $a_{r\theta}$, stress, $\tau_{r\theta}$, and torque, T, on the outer cylinder are given as

$$a_{r\theta} = \frac{2\omega_o R_o^2 R_i^2}{R_o^2 (R_o^2 - R_i^2)^2}\ln\left(\frac{R_o}{R_i}\right) \tag{15}$$

$$\tau_{r\theta} = 2\mu a_{r\theta} \tag{16}$$

$$T = \tau_{r\theta}(2\pi R_o L)R_o = 4\pi\mu L \frac{\omega_o R_o^2 R_i^2}{(R_o^2 - R_i^2)} \tag{17}$$

The mechanical power required to turn the cylinder is expressed as

$$P_W = T\omega_o \tag{18}$$

According to Camp and Stein, the root-mean-square velocity gradient, $\overline{G}$, can be measured as

$$\overline{G} = \sqrt{\frac{P}{\mu V_T}} = \frac{2\omega_o R_o R_i}{\left(R_o^2 - R_i^2\right)} \tag{19}$$

The root-mean-square velocity gradient of the concentric rotating cylinder device using total power input to the system is good agreement with Durren's study (1968).

However, concentric rotating cylinder flow is not always laminar (Taylor, 1923). If the fluid velocity between two cylinders exceeds a critical limit, the homogeneous motions of the fluid streamline may become unstable and generate eddies, which destabilize fluid conditions. Taylor performed stability studies using concentric cylinder apparatus. He found the torque on the outer cylinder increased linearly with the angular speed of inner cylinder until flow destabilized at which point there was an abrupt increase in torque. Eddies generated at these unstable conditions are termed Taylor vortices. A criterion for torque at which eddies begin to be formed was defined as

$$T_a = \frac{2\omega_i^2 R_i^2 (R_o - R_i)^3}{\nu^2 (R_i + R_o)} \tag{20}$$

Taylor suggested that a system with a rotating outer cylinder rotation and a stationary inner cylinder is more stable than one in which the inner cylinder rotates. Serra et al. (1997) used the development of Taylor vortices in a concentric rotating cylinder device to simulate isotropic turbulence in order to observe particle aggregation and breakup. Selomulya et al. (2002) a applied concentric rotating cylinder to produce shear particle

collisions between two parallel plates and produce a more isotropic turbulent flow than other mixing apparatus.

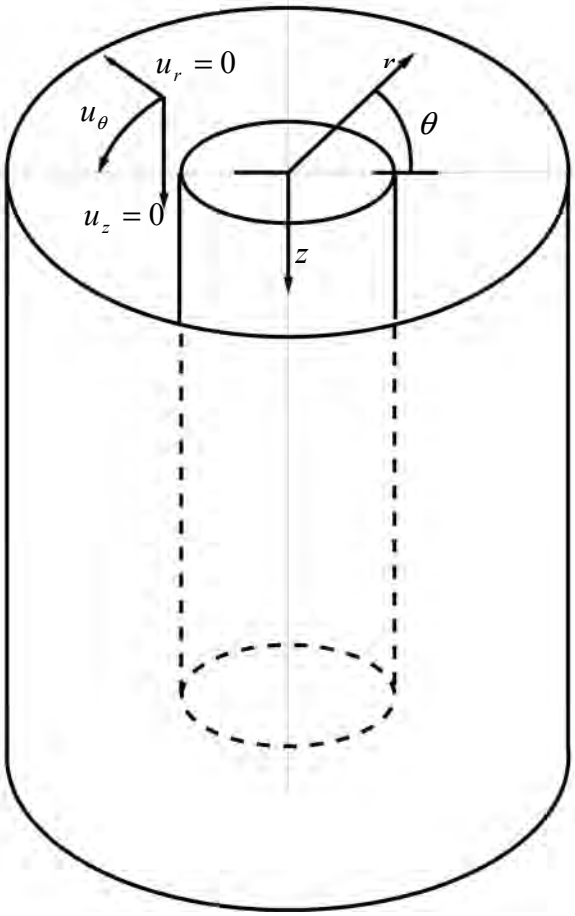

FIG. 9. Geometry of the Concentric Rotating Cylinder Apparatus Using on Cylindrical Coordinates

2.3.2 Turbulent Mixing Devices

Most flow mixing environments for particle aggregation are turbulent. Turbulent flow has spatial variations of fluid properties such as velocity, pressure and temperature, which are fluctuating in three dimensions. Turbulent flow has unstable and irregular movements, which produce complex fluid structures such as rotational eddies, shear strains, normal strains and stream flow (Wray and Hunt, 1990). One of the important characteristics of turbulent flow is eddy motion. Turbulent flow can sustain itself by generating new eddies, which mix and fill the shear layer. Turbulent eddy motion improves diffusion of mass, momentum and energy by three-dimensional movements and velocity gradients. Characterization of turbulent flow is defined by an energy flux from turbulent energy dissipation by eddy motions (Levich 1962). Kinetic energy of large scale eddies is converted into thermal energy by smaller sized eddies. The smallest eddies are those with the size of the Kolmogorov micro length scale, which is defined as a

$$\eta = \left(\frac{v^3}{\varepsilon} \right)^{1/4} \tag{21}$$

where η is Kolmogorov micro length scale, ε is the turbulent energy dissipation rate and v is the kinematic viscosity. The turbulent energy dissipation rate for a flocculator is estimated as a function of impeller geometry, velocity, and flocculator volume (Spicer et al. 1996).

$$\varepsilon = \left(\frac{N_P \omega^3 D^5}{V} \right) \tag{22}$$

where N_p is the impeller power number, ω is the impeller speed, V is the stirred tank volume, and D the impeller diameter.

Camp and Stein (1943) suggested a collision frequency function (β) for orthokinetic collisions between particles in the turbulent flow. The collision frequency function was expressed with mean energy dissipation function ($\overline{\Phi}$). This represents the average work of shear stress per unit of volume per unit of time at given system. The collision frequency function are suggested as

$$\beta = \frac{4}{3}\left(r_i + r_j\right)^3 \sqrt{\frac{\overline{\Phi}}{\mu}} \tag{23}$$

Saffman and Turner (1956) defined two particle flocculation mechanisms in turbulent flow in terms of the spatially varying velocities and the difference of inertia between the particles and bulk fluid. Saffman and Turner suggested that the inertial forces on particles play a less important role in neutrally buoyant conditions, i.e between equal size particles, and the small relative inertia between particles and the bulk fluid. Collision frequency functions can be expressed as a function of the turbulent energy dissipation (ε), which is assumed normally distributed, is given as

$$\beta = \sqrt{\frac{8\pi}{15}}\left(r_i + r_j\right)^3 \sqrt{\frac{\varepsilon}{\nu}} \tag{24}$$

Levich (1962) presented that particle collision mechanisms are caused by density gradients between the particles and fluid in terms of a turbulent energy dispersion. However, density gradients between the liquid bulk and particles are small, thus, the main mechanism of particle collisions in turbulent flow is generated by turbulent eddy

dispersion. Levich assumed that particles contact and flocculation occur only when particle size is smaller than the Kolmogorov microscale, and that flow characteristics are homogeneous isotropic turbulence. Particle collision frequency is suggested by Levich as

$$\beta = 12\pi\left(r_i + r_j\right)^3\sqrt{\frac{\varepsilon}{v}} \tag{25}$$

Experiment and model comparisons by Higashitani et al. (1983) revealed that Saffman and Turner's study overestimates particle collision in turbulent flow and suggested mean strain-rate as a

$$\overline{\frac{du}{dx}} = \sqrt{\frac{4\varepsilon}{15\pi v}} \tag{26}$$

Many studies have suggested different particle collision frequency functions for the turbulent particle aggregation. However, turbulent energy dissipation rate (ε) is recognized in all studies as being an important parameter in determining coagulation frequency. Therefore, it is important to consider the exact fluid dynamic characteristics of a flocculator in order to investigate particle collision frequency.

Fluid dynamics in a turbulent flocculator are governed by the types of mixing impeller. There are two general types of fluid flow that can be developed by mixing impellers; radial and axial flow. Rushton turbines, bar turbines, and anchor impellers develop radial flow, in which flow is discharged along the impeller radius and in a horizontal direction towards the flocculator wall. The characteristics of discharge flow in the radial impeller region are achieved by evaluation of the radial and tangential components of flow velocity (Ducoste, 1996). Radial fluid velocity is equal to 0.6~0.8

times impeller tip velocity and the maximum tangential velocity behind rotating impeller is equal to 1.2 times impeller tip speed. Foil impellers, marine propellers, pitched-blade turbines, and double spiral impellers are all axial flow impellers and are designed on the basis of screw theory. They all generate parallel flow to the impeller shaft, along the impeller axis. Argaman and Kaufman (1970) conducted turbulent flocculation experiments with two different types of mixing devices, a turbine (radial flow) impeller and a stake and stator (axial flow) impeller. Turbulent characteristics of the two impellers, measured with a hot-wire anemometer probe, indicated that the volume weighted mean-square-velocity fluctuation for stake and stator impellers was higher than for the turbine impeller. Root-mean-square velocity gradient comparisons between axial flow with a foil impeller and radial flow with a Rushton turbine, revealed that the foil impeller had lower values of $\overline{G}$ than the Rushton turbine at the same impeller speed (Weetman and Oldsue, 1988). To achieve the same $\overline{G}$, higher impeller speed is required for an axial flow impeller, which means that floc aggregates are exposed to more severe flow conditions. Spicer et al. (1996) showed that when a steady-state condition is reached, the radial flow impeller generates larger sizes of aggregates than the axial flow impeller at the same $\overline{G}$ value and that the axial flow impeller produces larger aggregate at the same impeller speed. Spicer et al. suggested that these results are caused by the exposure frequency of the aggregates to the impeller discharge region. Axial flow impellers discharge fluid flow in the axial direction, resulting in faster recirculation and often subjecting the floc aggregates to higher flow velocity than the radial flow impellers. Fig. 10 displays the flow pattern of each type of impeller. The investigation of fluid

dynamics in a flocculator tank to examine the influence of geometric variations on particle aggregation revealed that applied $\overline{G}$ could not explain geometric variations in flocculators, especially tank size and impeller designs (Ducoste and Clark, 1998). Ducoste and Clark suggested that different geometric parameters such as impeller tip speed and dimensionless impeller power number would be better parameters than $\overline{G}$ in coagulation modeling. McConnachie (1991) investigated the turbulence effects produced by three different impellers; a picket gate, two blade paddle, and a branched paddle, on turbidity removal. Turbulent characterization was achieved with LDV (Laser Doppler Velocimetery). McConnachie showed that the $\overline{G}$ value needed to achieve the maximum turbidity removal varied based on impeller type. Bouyer et al. (2001) used PIV (Particle Image Velocimetry) to analyze hydrodynamic environments and particle trajectories. Bouyer et al. showed that floc characteristics are dependent on an instantaneous velocity field after passage of the impeller blade by studying floc size and steady-state particle size Therefore, knowledge about the behavior of the flocculator impellers of different geometry geometries is required to achieve a better understanding of particle collisions and flocculation in turbulent fluid flow.

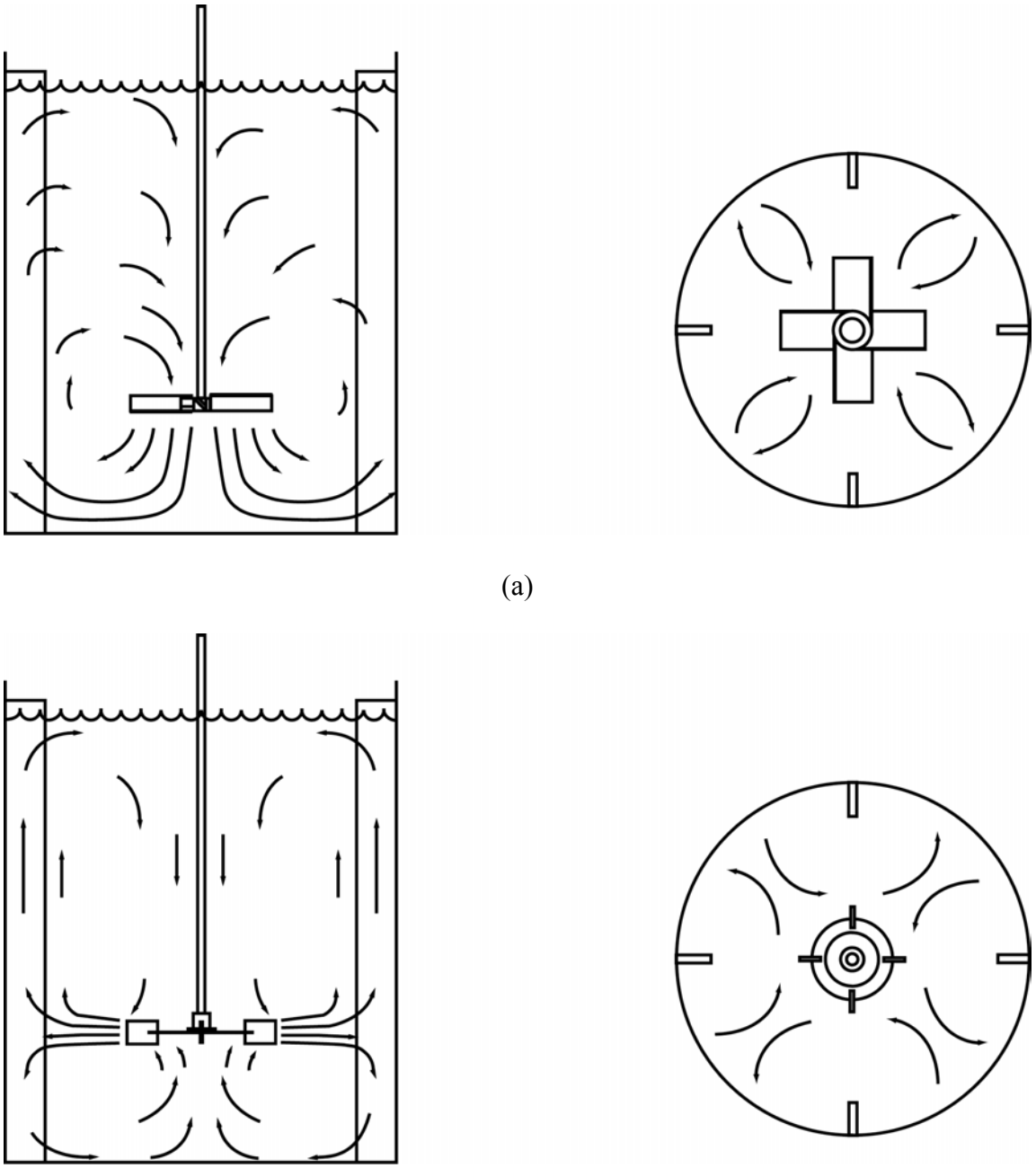

(a)

(b)

FIG. 10. Turbulent Impeller Flow Patterns: (a) Axial Flow and the Bottom View; (b) Radial Flow and the Bottom View

2.3.3 Summary

Many experimental devices have been applied to the study of orthokinetic flocculation. Representative apparatus reviewed include a rotating impeller, which generates turbulent flow, and concentric rotating cylinders, which develop uniform laminar flow. However, rotating impeller mixers do not have a well-characterized flow and it is difficult to characterize fluid dynamics in them. In contrast, the concentric rotating cylinder apparatus generates a well-defined flow, but it is simple laminar shearing flow, which is not found water treatment. Therefore, both well-established fluid dynamic characteristics and more realistic flow conditions such as spatial variations are required to understand particle aggregation and aggregate breakup mechanisms.

A method to create a more realistic and well-characterized flow is achieved by eccentrically locating the inner cylinder in the rotating cylinder apparatus. The eccentric rotating cylinder device has the unique features of developing spatially varying flow while having a known analytical solution to predict the flow behavior. The eccentric rotating cylinder apparatus originated from lubrication experiments in fluid dynamics for investigating journal bearing problems. This apparatus can generate pressure gradients, eddies in the region of the largest clearance, shear and extensional flow simultaneously, and spatially varying dynamic conditions. Ballal and Rivlin (1976) derived exact solutions for velocities, pressures, and streamlines with and without inertial forces. The eccentric rotating cylinder device developing spatially varying flow is more realistic than the concentric rotating cylinders generating simple shear flow. It also has a better characterized flow than a rotating impeller mixer.

CHAPTER III

THE ECCENTRIC ROTATING CYLINDER SYSTEM

3.1 Background

The concentric rotating cylinder apparatus generates uniform state of shearing flow. However, this uniform flow is different than typical mixing flow, which has spatial variation. One way to generate spatially varying flow is to eccentrically locate one cylinder between two parallel cylinder devices. Streamlines of concentric and eccentric rotating cylinders are displayed on Fig 11. Streamlines for concentric rotating cylinders are developed by (12) and for eccentric rotating cylinders are based on Ballal and Rivlin (1976)'s analytical solutions. These figures show that concentric rotating cylinders generate simple streamlines, but eccentric rotating apparatus develop complex laminar flow. Even though eccentric rotating cylinders generate spatially varying flow this spatially varying flow has known analytical solutions for the flow velocities, strain-rates, pressures and streamlines.

By simply displacing one of the cylinders to an eccentric location, the eccentric rotating apparatus develops pressure gradients, Taylor vortices, and eddies (Kamal, 1966). These fluid dynamic properties and motions provide valuable data for particle coagulation and breakup studies. Pressure gradients generated by the tendency to restore concentricity are important in the study of aggregate breakup mechanisms as floc rupture is caused by pressure differences around the aggregates (Thomas, 1964). It has been known that concentric rotating cylinder apparatus does not develop spatial varying fluid flow. The

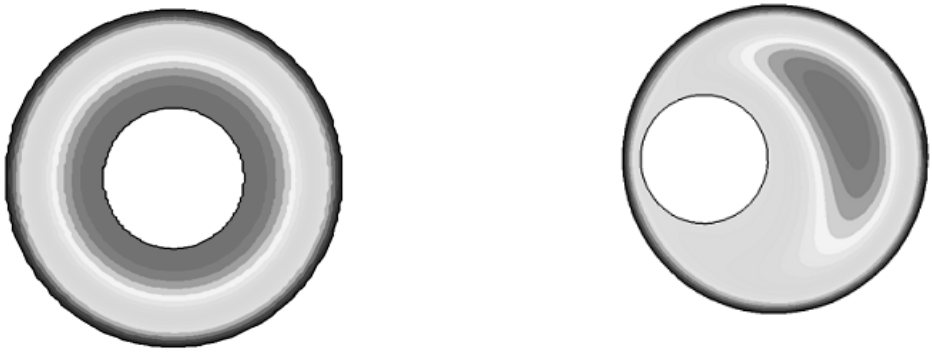

(a) (b)

FIG. 11. Streamline Developments (r_o = 7.62 *cm*, r_i = 3.175 *cm,* ω = 60 RPM): (a) Concentric Rotating Cylinders; (b) Eccentric Rotating Cylinders ($v = 1\,cm^2/\sec$, $\varepsilon = 0.8$)

normal components of strain-rate in concentric cylinders are neglected, because only the angular direction velocity (u_θ) is non-zero. Thus, concentric rotating apparatus is often used to develop pure shear strain-rate flow. However, eddy development in the eccentric rotating cylinder can provide not only spatial variation of fluid dynamics but also normal stain-rate. Therefore, applications of eccentric rotating apparatus will achieve more realistic mixing conditions with known analytical solutions and will be very beneficial for studying particle coagulation and aggregate breakup.

In an early study on eccentric rotating cylinder apparatus, Wannier (1950) examined the relationship between conventional lubrication theories of the Stokes and Reynolds approximation, and presented solutions of eccentric cylinder flow without restricting the geometry. Wood (1957) used modified bipolar coordinates to reduce the

geometry to polar coordinates where the eccentricity is equated to zero. Linearization of the Navier-Stokes equations for small displacements of the inner cylinder was conducted with perturbation analysis incorporating Bessel functions of the first order and higher order corrections. Kamal (1966) compared three approximate solutions of the Navier-Stokes equations; Reynolds, Stokes, and an inertial approximation. The Reynolds approximation is limited application to the case of small clearances in which the curvature effects on the streamlines are negligible. Stokes approximation is only applicable when the Reynolds number is small, usually below one. Kamal employed a bipolar coordinate system to simplify the boundary conditions. The inertial approximation conducted by Kamal was a first attempt that considered inertial forces on the streamline curvature, and separation and reattachment points in the eccentric rotating cylinder flow. Ashino and Yoshida (1975) obtained solutions for the slow viscous flow between eccentric rotating cylinders with stream functions using bipolar coordinates. Ashino and Yoshida suggested that the Stokes approximation is only applicable when Reynolds number is less than 7. When the Reynolds number is greater than 7, the Stokes approximation cannot clearly describe fluid dynamics in eccentric cylinders, as inertial forces are larger than viscous forces. Thus, inertial approximations are required to understand high Reynolds number flow in eccentric rotating cylinder apparatus.

Studies have been reported for eccentric rotating cylinder apparatus operating conditions. They have increasingly higher rotating speed and Reynolds number for the eccentric devices covered both laminar and the turbulent flow regions. Flow stability studies showed that critical Taylor number for system with rotating outer cylinder, which

indicates transition laminar into turbulent flow, is much higher than for ones with stationary outer cylinder rotation for both eccentric (Yamada and Nakabayshi, 1968) and concentric cylinder devices (van Durren, 1968). However, few studies have been conducted for the a system with rotating outer cylinder rotation and stationary inner cylinder so data for a wide range of cylinder angular velocities and Reynolds numbers are not available. Yamada and Nakabayashi (1968) examined a system with rotating outer cylinder rotation and stationary inner cylinder using plain slider bearing analysis. The effects of eccentricity and clearance ratio on inertial forces showed that as clearance ratio increased and eccentricity decreased the inertial effects were increased. By taking inertial forces into consideration, pressure distributions changed from symmetric to asymmetric. Diprima and Stuart (1972) obtained solutions for the first-order linearized inertial correction at small clearance and modified the Reynolds number using a modified bipolar coordinate system. Unlike previous investigations that focused on the limited eccentricity and single stationary cylinder cases, Diprima and Stuart considered either the outer cylinder, inner cylinder, or both cylinders rotating, and there was no limit on eccentricity. Ballal and Rivlin (1976) derived two exact solutions for eccentric rotating cylinder geometries. Ballal and Rivlin analyzed two cases for arbitrary geometries in which both or only one of the cylinders are rotating. They obtained resultant forces acting on the inner and outer cylinders, normal and tangential force distributions, and streamline patterns. The solution of Ballal and Rivlin is based on bipolar coordinates, which converts the eccentric geometry in Euclidean space into a concentric one in complex space. San Andres and Szeri (1984) compared Ballal and

Rivlin's analytical solutions to their numerical approaches using Galerkin's method with *B*-spline test functions. At increasing eccentricity an eddy is developed in the large gap between the two cylinders in both cases. Along with eddy formation, separation and reattachment of flow is generated. San Andres and Szeri showed that the separation point when only one of cylinders is rotating, moves in the direction of cylinder rotation. However, Ballal and Rivlin's results showed that the separation point moves in the opposite direction of cylinder rotation when the inner cylinder is rotating and the outer cylinder is stationary. In the case of outer cylinder rotation and inner cylinder stationary, the separation point is dependent on eccentricity. When the eccentricity is between 0.27 and 0.57, the separation point moves opposite to rotation direction. However, the separation point moves in the same direction as the eccentricity is between 0.57and 1.0. San Andres and Szeri did not provide any experimental verification for their results. The Stokes approximation analysis of Ballal and Rivlin was verified by comparing computational data and experimental measurements (Thomas, 1999). The measurement of Thomas indicated that measurement of the accuracy of the Stokes approximation by the Ballal and Rivlin solution is highly dependent on fluid viscosity and cylinder angular velocity. For a low viscosity fluid such as pure water, the development of small eddies break streamline creation. When the fluid viscosity reached 1.86 cm^2/sec, theoretical computation and experimental measurement were identical at small eccentricities. Photographic observations indicated that inertial forces acting on the streamlines are quite appreciable. However, more computational work on the linearized inertial correction analysis of Ballal and Rivlin were not conducted.

3.2 Governing Equations and Analytical Solutions

The flow between two cylinders is studied where the outer cylinder is rotating, and inner cylinder is stationary. Their axes are parallel but one of cylinders is offset. In general, flow development between two parallel cylinders will be three-dimensional. However, the flow movements in the *z* direction caused by end effects can be neglected by assuming that the length of cylinder is infinitely long. Thus, fluid motions between the annuls will be true two-dimensional flow, whose equations of motion can be described by the continuity equation and the two components of the Navier-Stokes equations. In the Cartesian coordinates the continuity equation and Navier-Stokes equations in *x* and *y* components are expressed as

$$\frac{\partial u_x}{\partial x} + \frac{\partial u_y}{\partial y} = 0 \tag{27}$$

$$u_x \frac{\partial u_x}{\partial x} + u_y \frac{\partial u_x}{\partial y} = -\frac{1}{\rho}\frac{\partial p}{\partial x} + \nu\left(\frac{\partial^2 u_x}{\partial x^2} + \frac{\partial^2 u_x}{\partial y^2}\right) \tag{28}$$

$$u_x \frac{\partial u_y}{\partial x} + u_y \frac{\partial u_y}{\partial y} = -\frac{1}{\rho}\frac{\partial p}{\partial y} + \nu\left(\frac{\partial^2 u_y}{\partial x^2} + \frac{\partial^2 u_y}{\partial y^2}\right) \tag{29}$$

(27) is satisfied by introducing Lagrange's stream function, $\psi(x, y)$, which is useful to describe streamlines in bi-directional flow. Velocities of *x* and *y* directions are presented with stream function as

$$u_x = \frac{dx}{dt} = -\frac{\partial \psi}{\partial y} \qquad u_y = \frac{dy}{dt} = \frac{\partial \psi}{\partial x} \tag{30}$$

By differentiating (28) and (29) with respect to *y* and *x*, and by subtracting one equation from the other, the equation can be rewritten as a forth-order partial differential equation.

$$\nabla^4\psi = \frac{1}{\nu}\left(\frac{\partial\psi}{\partial y}\frac{\partial}{\partial x}\left(\nabla^2\psi\right) - \frac{\partial\psi}{\partial x}\frac{\partial}{\partial y}\left(\nabla^2\psi\right)\right) \tag{31}$$

where the Laplace operator (∇^2) in Cartesian coordinates is defined as

$$\nabla^2 \equiv \frac{\partial^2}{\partial x^2} + \frac{\partial^2}{\partial y^2} \tag{32}$$

When the Reynolds number is within the Stokes regime, the viscous effects are larger than the inertial forces. Then inertial effects can be neglected and the equation reduces to the biharmonic or Stokes equation,

$$\nabla^4\psi^{(0)} \equiv 0 \tag{33}$$

where $\psi^{(0)}$ is the Stokes stream function neglecting the inertial forces. The no-slip boundary conditions for (33), with the inner cylinder stationary and outer cylinder rotating, is

$$\begin{aligned} u_x &= \frac{\partial\psi^{(0)}}{\partial y} = \omega_o y \\ u_y &= \frac{\partial\psi^{(0)}}{\partial x} = -\omega_o(x-l) \end{aligned} \qquad \text{on the outer cylinder} \tag{34}$$

$$\begin{aligned} u_x &= \frac{\partial\psi^{(0)}}{\partial y} = 0 \\ u_y &= \frac{\partial\psi^{(0)}}{\partial x} = 0 \end{aligned} \qquad \text{on the inner cylinder} \tag{35}$$

where l is distance from O to C, and x and y are generic points of outer cylinder in Fig. 12. If the Reynolds number is large, inertial forces cannot be neglected. Then, by

introducing $\psi^{(1)}$, which is the inertial stream function, the equation defining two-dimensional flow with inertial forces can be obtained as

$$\nabla^4\psi^{(1)} = \frac{\partial\psi^{(0)}}{\partial y}\frac{\partial}{\partial x}(\nabla^2\psi^{(0)}) - \frac{\partial\psi^{(0)}}{\partial x}\frac{\partial}{\partial y}(\nabla^2\psi^{(0)}) \tag{36}$$

with boundary conditions

$$u_x = \frac{\partial\psi^{(1)}}{\partial y} = 0$$

$$\text{on both cylinders} \tag{37}$$

$$u_y = \frac{\partial\psi^{(1)}}{\partial x} = 0$$

Thus, the stream function with viscous and inertial effects is defined as summation of both Stokes and inertial stream functions

$$\psi = \psi^{(0)} + \frac{1}{v}\psi^{(1)} \tag{38}$$

However, the eccentric rotating cylinder apparatus that offsets one of the cylinders has nonparallel boundaries, which means that the Navier-Stokes equations cannot be linearized, and exact solutions are very difficult in the Cartesian coordinates. Thus, Ballal and Rivlin introduced a bipolar coordinates, which is an exact match with the geometry of the eccentric rotating cylinder apparatus. The eccentric rotating cylinder geometry based on bipolar coordinates is presented in Fig. 12. The transformation of from Cartesian coordinates to complex bipolar coordinates can be expressed as

$$x = -b\frac{\sinh(\xi)}{\cosh(\xi) - \cos(\eta)} \tag{39}$$

$$y = b\frac{\sin(\eta)}{\cosh(\xi) - \cos(\eta)} \tag{40}$$

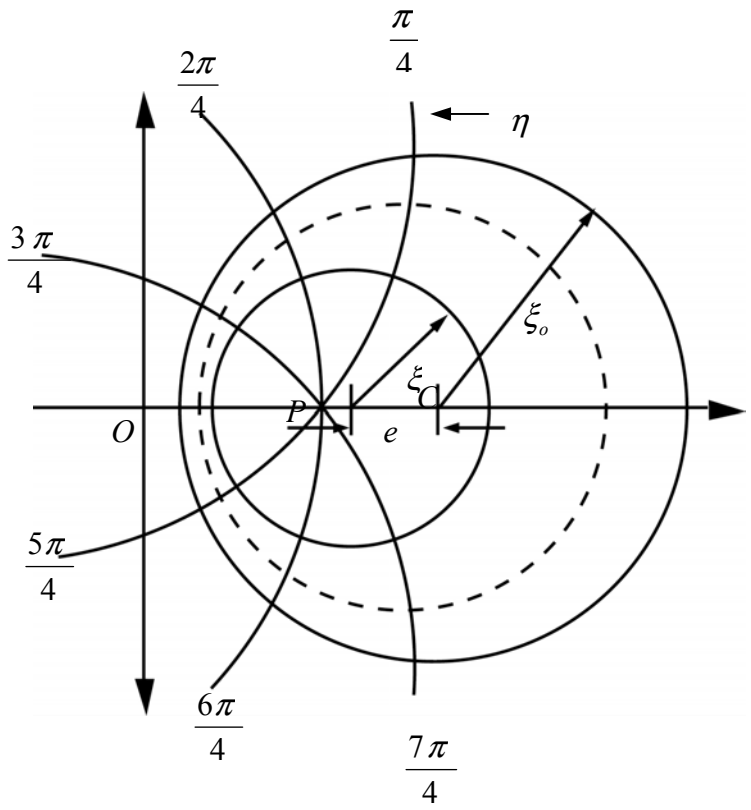

FIG. 12. Geometry of Eccentric Rotating Cylinders and Bipolar Coordinates (ξ, η)

With boundary conditions $\xi_o \le \xi \le \xi_i$ and $0 \le \eta \le 2\pi$. where b is the distance between O and P given by

$$b = \frac{1}{2e}\sqrt{\left(R_o^2 + R_i^2 - e^2\right) - 4R_o^2 R_i^2} \tag{41}$$

Boundary conditions are $\xi = \xi_o$ on the outer cylinder and $\xi = \xi_i$ on the inner cylinder where ξ_i and ξ_o are negatively valued constants. Other relationships for this system are

$$R_o = \frac{-b}{\sinh(\xi_o)} \tag{42}$$

$$R_i = \frac{-b}{\sinh(\xi_i)} \tag{43}$$

$$c = -b\coth(\xi_o) \tag{44}$$

$$\varepsilon = -b\left(\coth\xi_o - \coth\xi_i\right) \tag{45}$$

To solve the biharmonic equation for the noninertial stream function with complex coordinates, the Laplace operator must be defined in bipolar coordinates as

$$\nabla^2 = \frac{1}{h^2}\left(\frac{\partial^2}{\partial\xi^2} + \frac{\partial^2}{\partial\eta^2}\right) \tag{46}$$

where scale factors for bipolar coordinates are defined as

$$h_\eta = h_\xi = h = \frac{b}{\cosh(\xi) - \cos(\eta)} \tag{47}$$

Then, biharmonic equation is rewritten as

$$\nabla^2\left(\nabla^2\psi^{(0)}\right) = \frac{1}{h^2}\left(\frac{\partial^2}{\partial\xi^2} + \frac{\partial^2}{\partial\eta^2}\right)\left(\frac{1}{h^2}\left(\frac{\partial^2\psi^{(0)}}{\partial\xi^2} + \frac{\partial^2\psi^{(0)}}{\partial\eta^2}\right)\right) = 0 \tag{48}$$

For the case where the inner cylinder is stationary and the outer cylinder is rotating, the boundary conditions become

$$\psi^{(0)} = 0 \text{ and } \frac{\partial\psi^{(0)}}{\partial\xi_i} = 0 \text{ on the inner cylinder} \tag{49}$$

$$\psi^{(0)} = \overline{\psi} \text{ and } \frac{\partial\psi^{(0)}}{\partial\xi_o} = -R_o\omega_o h \text{ on the outer cylinder} \tag{50}$$

where $\overline{\psi}$ is a function of the radius of the inner cylinder, radius of the outer cylinder and angular velocity. The solution of the Stokes stream functions neglecting the inertial forces can be expressed as

$$\psi^{(0)} = h\phi^{(0)} \tag{51}$$

where $\phi^{(0)}$ is a function dependent on the eccentricity ratio (e/c), radius ratio, R_i/R_o, and outer cylinder angular velocity, ω_o. For the case of the governing inertial forces, (36) must be rewritten in bipolar coordinates. Transformation of (36) and t(37) with (46) and (48) are

$$\nabla^4\psi^{(1)} = \frac{1}{h^4}\left(\psi_\eta^{(0)}\frac{\partial}{\partial\xi} - \psi_\xi^{(0)}\frac{\partial}{\partial\eta}\right)\left(\frac{\partial^2\psi^{(0)}}{\partial\xi} + \frac{\partial^2\psi^{(0)}}{\partial\eta}\right) \tag{52}$$

Thus, the stream function with consideration of inertial forces can be expressed as

$$\psi^{(1)} = h\phi^{(1)} \tag{53}$$

where $\phi^{(1)}$ is also function that depends on the eccentricity ratio (e/c), radius ratio, R_i/R_o, and outer cylinder angular velocity, ω_o. Detailed analytical solutions are displayed in Appendix III.

Since the investigation of Ballal and Rivlin (1976) only focused on streamline computations in eccentric rotating cylinder apparatus, it is inappropriate to directly apply Ballal and Rivlin's analytical solutions for the study of the coagulation. In this thesis, I will modify Ballal and Rivlin's analytical solutions for the application of eccentric rotating cylinder apparatus for the coagulation study. Modifications will be conducted based on relationships between stream function and velocity vector, and generalized two-dimensional strain-rate system. Using the modified analytical solutions, fluid velocities, strain-rates, mean principal strain-rates and root-mean-velocity gradients can be obtained for the various geometries and rotation speeds of a system.

3.3 Fluid Dynamics of Eccentric Rotating Cylinder Apparatus

A streamline is a line in a flow field that is everywhere tangent to the velocity vector at each point along the streamline for any instant of time. Thus, the component of the velocity normal to a streamline is always equal to zero so that there is no mass flux across a streamline. Fluid velocities of eccentric rotating cylinder apparatus are obtained based on two stream functions (51) and (53). Fluid velocities for the radial, ξ, and angular, η, directions in viscous and inertial flow are calculated with (30) and expressed as.

$$u_{\xi} = \frac{d\xi}{dt} = \frac{1}{h}\frac{\partial \psi}{\partial \eta} = \frac{1}{h}\left\{ h\frac{\partial \psi}{\partial \eta} + \psi\frac{\partial h}{\partial \eta} \right\} \tag{54}$$

$$u_{\eta} = \frac{d\eta}{dt} = -\frac{1}{h}\frac{\partial \psi}{d\xi} = -\frac{1}{h}\left\{ h\frac{\partial \psi}{\partial \xi} + \psi\frac{\partial h}{\partial \xi} \right\} \tag{55}$$

Strain-rate is used to define the intensity and direction of the deformation at a given point with respect to a specified plane within a fluid element. The strain-rate in Cartesian coordinates is derived in Appendix I. However, Ballal and Rivlin's stream functions are based on complex bipolar coordinates. In order to derive strain-rate based on bipolar coordinates it may be useful to develop generalized two-dimensional system. It is known that tensor equations are valid in any generalized coordinate system. However, in order to express physical phenomena, which are invariant and independent of the coordinate system, tensor equations must be expanded with proper physical components. Detailed analysis of generalized two-dimensional strain-rate is presented in

Appendix II. By assuming an orthogonal coordinate system the normal component ($a_{\xi\xi}$ and $a_{\eta\eta}$) and shear component ($a_{\xi\eta}$ and $a_{\eta\xi}$) strain-rate tensor is expressed as

$$a_{\xi\xi} = \frac{\partial}{\partial\xi}\left(\frac{u_\xi}{h_\xi}\right) + \frac{1}{2h_\xi^2}\sum_{m=\xi,\eta}\frac{u_m}{h_m}\frac{\partial}{\partial m}(h_\xi^2) \tag{56}$$

$$a_{\eta\eta} = \frac{\partial}{\partial\eta}\left(\frac{u_\eta}{h_\eta}\right) + \frac{1}{2h_\eta^2}\sum_{m=\xi,\eta}\frac{u_m}{h_m}\frac{\partial}{\partial m}(h_\eta^2) \tag{57}$$

$$2a_{\xi\eta} = 2a_{\eta\xi} = \frac{h_\xi}{h_\eta}\frac{\partial}{\partial\eta}\left(\frac{u_\xi}{h_\xi}\right) + \frac{h_\eta}{h_\xi}\frac{\partial}{\partial\xi}\left(\frac{u_\eta}{h_\eta}\right) \tag{58}$$

Representative characteristics of fluid dynamics such as streamline, velocity, strain-rate were analyzed, however, the main focus of this study is in applications of the eccentric rotating cylinder apparatus for the investigation of particle coagulation and flocculation. To contribute to the study of coagulation, mean principal strain-rate and Camp and Stein's velocity gradient are also derived. According to Kramer and Clark (1997, 2000), a local principal strain-rate is obtained from the diagonalization of the strain-rate tensor without a loss of information. The 2×2 strain-rate (E) is a symmetric matrix, therefore there exists an orthogonal matrix P such that

$$E = \begin{bmatrix} a_{\xi\xi} & a_{\xi\eta} \\ a_{\xi\eta} & a_{\eta\eta} \end{bmatrix} \tag{59}$$

$$P = \begin{bmatrix} -\frac{1}{2}\left\{\left(a_{\xi\xi}+a_{\eta\eta}\right)+\sqrt{\left(\left(a_{\xi\xi}-a_{\eta\eta}\right)^2+4a_{\xi\eta}\right)}\right\} & -\frac{1}{2}\left\{\left(a_{\xi\xi}+a_{\eta\eta}\right)-\sqrt{\left(\left(a_{\xi\xi}-a_{\eta\eta}\right)^2+4a_{\xi\eta}\right)}\right\} \\ 1 & 1 \end{bmatrix} \tag{60}$$

where $\mathrm{col}_1(P)$ and $\mathrm{col}_2(P)$ are linearly independent eigenvectors of E. Since E is symmetric matrix, P^T is equal to P^{-1}. The diagonal elements of E_{max} are expressed with the eigenvalues of E associated with eigenvectors as a

$$E_{\max} = P^{-1}EP = P^T EP \tag{61}$$

where P^{-1} is the inverse matrix of P and P^T is the transpose of matrix P. Then, the diagonalized matrix ($E_{\max}$) is

$$E_{\max} = \begin{bmatrix} \frac{1}{2}\left\{\left(a_{\xi\xi} + a_{\eta\eta}\right) + \sqrt{\left(\left(a_{\xi\xi} - a_{\eta\eta}\right)^2 + 4a_{\xi\eta}\right)}\right\} & 0 \\ 0 & \frac{1}{2}\left\{\left(a_{\xi\xi} + a_{\eta\eta}\right) - \sqrt{\left(\left(a_{\xi\xi} - a_{\eta\eta}\right)^2 + 4a_{\xi\eta}\right)}\right\} \end{bmatrix} \tag{62}$$

A local principal strain-rate is equivalent to the absolute maximum principal strain-rate (Kramer and Clark, 1997). Thus, a local principal strain-rate for the eccentric rotating apparatus is given as

$$\left|a'_{\max}\right| = \frac{1}{2}\left[\left(a_{\xi\xi} + a_{\eta\eta}\right) \pm \sqrt{\left(\left(a_{\xi\xi} - a_{\eta\eta}\right)^2 + 4a_{\xi\eta}\right)}\right] \tag{63}$$

Root-mean-square velocity gradient can be derived from the required mechanical power input to turn the outer cylinder with (18) and the volume of the fluid system. To estimate theoretical torque, total shear stress force exerted on the cylinder surface is required. For Stokes flow, average shear stress over $0 \le \eta \le 2\pi$ on the outer cylinder ($\overline{\tau^{(0)}}$) is suggested as

$$\overline{\tau^{(0)}} = 2\mu\lambda^{(0)}\varpi_o \tag{64}$$

where $\lambda^{(0)}$ is the dimensionless function of inner and outer cylinder radius. For inertial flow, average shear stress, $\overline{\tau^{(1)}}$, is given by

$$\overline{\tau^{(1)}} = \lambda^{(1)} R_o^2 \varpi_o^2 \tag{65}$$

where $\lambda^{(1)}$ is a dimensionless functions of η, which depend on the geometry of the system. Root-mean-square velocity gradient is derived from (19) with (64) and (65)

$$\overline{G} = \sqrt{\frac{2R_o^2 \varpi_o \overline{\tau^{(0),(1)}}}{\mu(R_o^2 - R_i^2)}} \tag{66}$$

In this work, Matlab (Mathworks, Inc) was used to perform the calculations due to the complexity of the analytical solution. The streamlines, velocities, strain-rates and root-mean-square velocity gradients from the analytical solutions were directly coded into the Matlab source code. In order to produce contour plots for the streamlines, an array of specified ξ and η coordinates are required. Thus, 200 × 200 grids are set up by ξ and η values. The ξ values ranging from ξ_1 to ξ_2 and the η values ranging from $-\pi$ to $+\pi$ each incremented into 200 steps. The calculated data was saved to a file and transferred to another software package to create streamlines. The data was transferred from the data file into Techplot 9.0 (Amtech Engineering, Inc) and plotted streamlines. The mean principal strain-rate is obtained from the total sum of local principal strain-rate divided by the number of data. However, as shown in Fig. 13 a), data distribution displays that the narrow gap region is denser than large gap location due to bipolar coordinates. Thus, the total sum of local principal strain-rate divided by the number of data may overestimate the mean principal strain-rate because narrow gap has faster fluid velocity than wide gap. In order to compensate unbalanced data distributions, computational grid are generated and presented in Fig. 13. However, computational meshes are also shows that smaller in elements exist in the narrow gap region, while

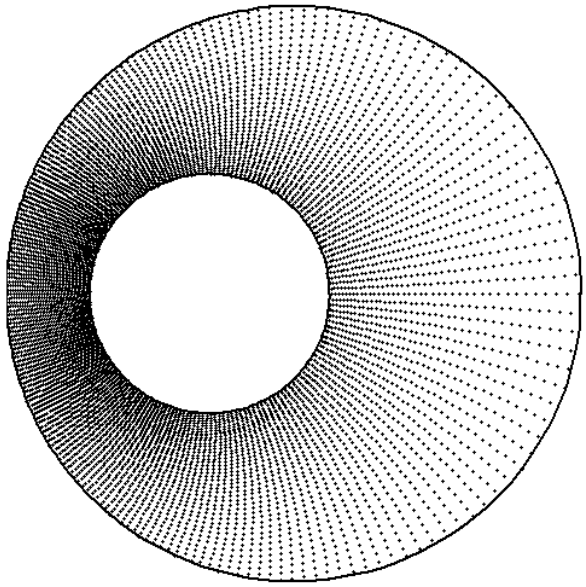

(a)

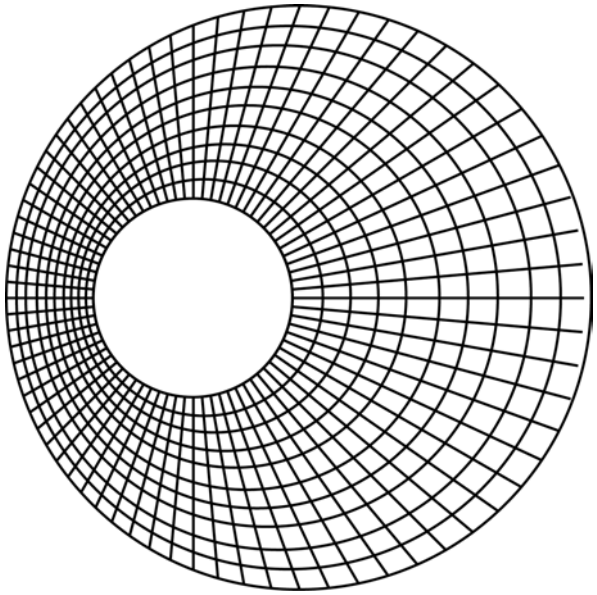

(b)

FIG. 13. a) Data Distribution and b) Computational Grids for Eccentric Rotating Cylinders

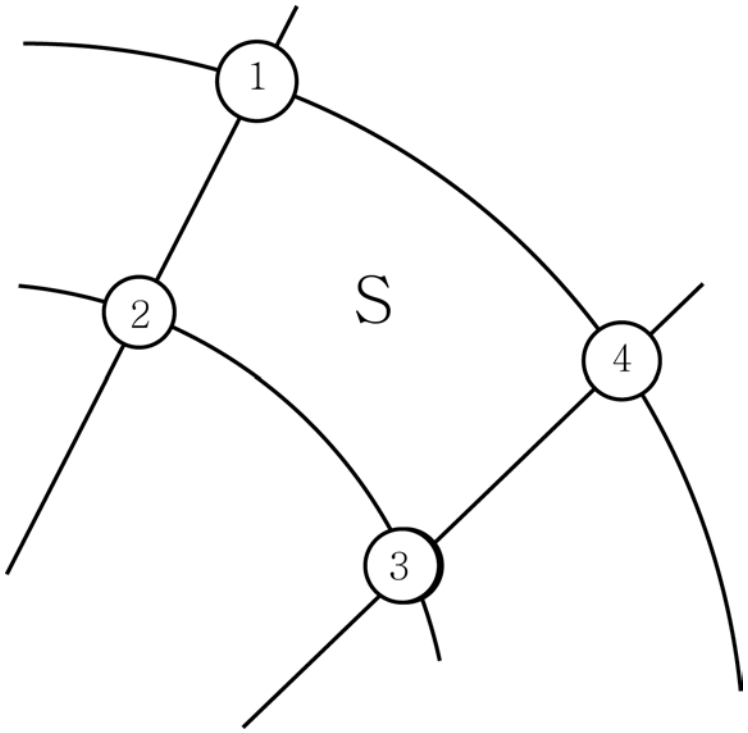

FIG. 14. Specific Fluid Element Coordinates

larger size elements are found in wide gap area. To avoid overestimation of the mean principal strain-rate, area weight methods are applied. The total principal strain-rate on a specific fluid element is divided by the area of each fluid element. The computation of the mean principal strain-rate of a mesh using weighted method is presented in Fig 14. The mean principal strain-rate is defined as

$$\overline{|a_{\max}|} = \frac{1}{\sum_{S}(Area)_S}\left[\sum_{S}\frac{1}{4}(Area)_S\left(a'_{\max 1}+a'_{\max 2}+a'_{\max 3}+a'_{\max 4}\right)_S\right] \tag{67}$$

where S indicate one specific element and the subscript number is the fluid element coordinate.

CHAPTER IV

RESULTS AND DISCUSSION

4.1 Introduction

The objective of this investigation was to evaluate the eccentric rotating cylinder apparatus for the improved study of particle coagulation. Conventional apparatuses have limitations. The concentric rotating cylinders are developing uniform laminar flow and turbulent mixing device do not have well-defined fluid dynamics. Many types of coagulation studies would be improved if an apparatus with well-defined fluid dynamics and spatially varying flow were developed. For this reason, this investigation presents computed streamlines, velocities and strain-rates to show well-defined fluid dynamics for the eccentric rotating cylinder apparatus. The spatial variations of the eccentric rotating apparatus are obtained by presenting streamlines and velocity variations as eccentricity ratio changes. The root-mean-square velocity gradient and mean principal strain-rate are obtained for its application to coagulation. These computed data, which are based on Ballal and Rivlin's solution, are compared to previous experimental data (Thomas, 1999) to insure the validity and accuracy of the computational work of this investigation. All of computational works performed with MATLAB (Mathworks, Inc) and streamlines were plotted with Techplot 9.0 (Amtech Engineering, Inc).

4.2 Determination of Analytical Solution

Since Ballal and Rivlin (1976) suggested two analytical solutions, Stokes and inertial method, it is required to determine a preferable solution for the study of the coagulation. The difference between Stokes and inertial method is governing forces. When Reynolds number is close to zero, viscous forces overwhelm inertial forces. Thus, Stokes method is used to consider viscose forces on fluid dynamics. Fig. 15 shows comparison of streamlines developed by the Stokes and inertial method. Both methods are simulated under the same conditions but the inertial method is included kinematic viscosity for inertial forces. For Stokes flow the eddy position does not skew to the direction of rotation with eccentricity (see Fig. 15(a)). The eddy development is symmetric at all values of Reynolds number. However, as the fluid viscosity is decreased and mixing intensity is increased (Reynolds number is increased over one) inertial forces cannot be neglected. The effects of inertial force on streamline developments are presented in Fig. 15(b). The eccentric rotating cylinder device is assumed to contain a fluid with kinematic viscosity 1 $cm^2/\sec$ and to rotate its outer cylinder at 30 RPM. Both Stokes and inertial methods develop an eddy in the wide clearance. Stokes flow shows that a developed eddy is symmetric. However, for inertial flow the eddy is skewed in the rotating direction by inertial forces. More detailed analysis of inertial force effects on fluid dynamics are presented in Fig. 16 and 17. Contour plots in Fig. 16 show inertial effects on angular (η) and radial (ξ) velocity distributions. Angular and radial velocity distributions are symmetric for the Stokes flow. However, inertial forces break down the symmetric balance for inertial flow. Normal and shear strain-rate

distributions are also shifted in the rotating directions by inertial forces in Fig. 17. Generally, coagulation studies require various rotating speeds and kinematic viscosities. Inertial effects cannot be neglected, even at low angular velocity. Therefore, the following results are computed considering inertial forces.

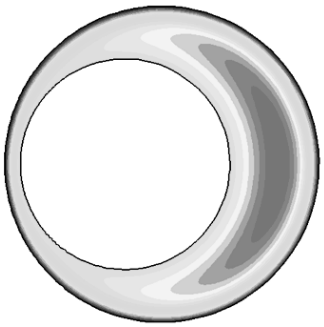

(a)

(b)

FIG. 15. Streamline developments with (a) Stokes; (b) inertial ($\nu = 1\ cm^2/\sec$, R_o = 7.62 cm, $R_i = 5.08\ cm$, $\omega = 30$ RPM, $\varepsilon = 0.7$)

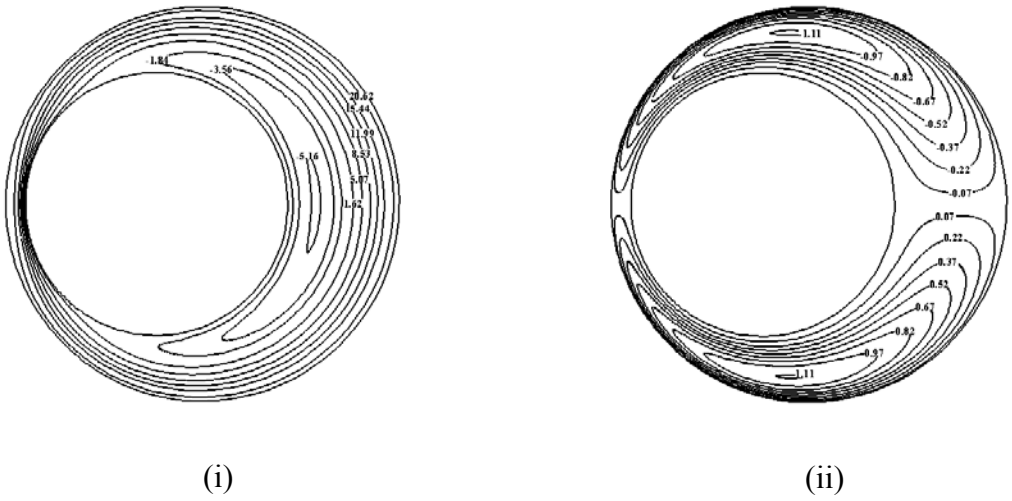

(i) (ii)

(a)

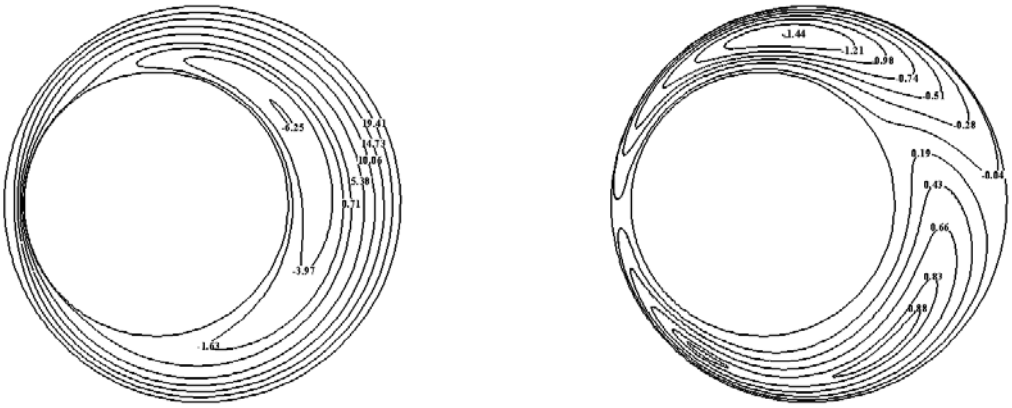

(i) (ii)

(b)

FIG. 16. (i) Angular velocity and (ii) radial velocity distributions in (a) Stokes; (b) inertial ($\nu = 1\ cm^2/\sec,\ \omega = 30$ RPM, $\varepsilon = 0.7$)

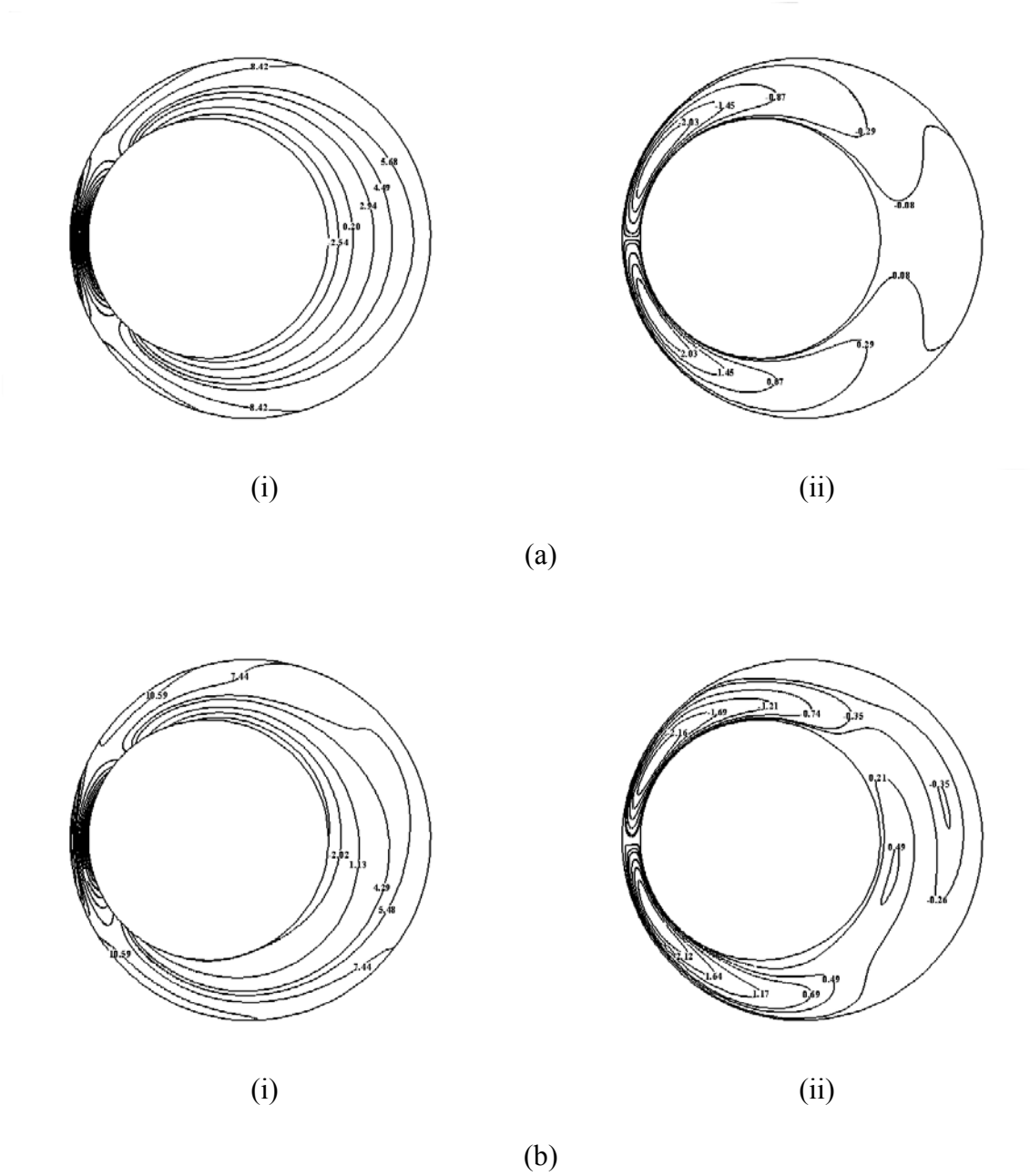

FIG. 17. (i) Shear strain and (ii) normal strain-rate distributions in (a) Stokes; (b) inertial ($\nu = 1\ cm^2/\sec$, $\omega = 30$ RPM, $\varepsilon = 0.7$)

4.3 Fluid Dynamics

One of the advantages of using the eccentric rotating cylinder apparatus that it has well-defined fluid dynamics. The stability of the fluid flow for the eccentric rotating cylinder apparatus is governed by eddy development in the wide clearance area. The eddy development is related to the geometry of the inner cylinder. The geometry of the inner cylinder is determined by the eccentricity (e) or eccentricity ratio (e/c). The inertial forces exerted on the fluid are estimated from the Reynolds number. Various equations to determine the Reynolds number for the eccentric rotating cylinder apparatus have been suggested in the literature. Table. 1 shows the various equations for Reynolds number for the eccentric rotating cylinder apparatus. In this research, Reynolds number is defined by the equation of Vohr (1968) and Pereira et al., (2001) as

$$\mathrm{Re} = \frac{\rho \omega_o R_o (R_o - R_i)}{\mu} \tag{68}$$

Values of the Reynolds numbers used in this investigation are presented in Table. 2.

Fig. 18 shoes that how the development of eddies changes when the position of the inner cylinder changes. It shows that an eddy develops at a constant Reynolds number as the eccentricity ratio increases. At low eccentricity ratio, streamline developments are almost symmetric. However, as eccentricity ratio is increased the eddy develops in the largest clearance area and the position of the eddy shifts in the direction of rotation. This clearly indicates that inertial forces are increased as eccentricity ratio increases. Fig. 19 shows the movement of eddy separation and reattachment points, as eccentricity ratio increases, with two different rotation speeds. At lower rotation speed

TABLE 1. Definitions of Reynolds number for Eccentric Rotating Cylinder Apparatus in Literatures

Reference	Equation
Ballal and Rivlin (1976) and Kumar and Homsy (1996)	$\mathrm{Re} = \frac{\rho \omega_o R_o^2}{\mu}$
Diprima and Stuart (1972)	$\mathrm{Re} = \frac{\rho \omega_o R_o^2 \alpha^2}{\mu}$
Vohr (1968) and Pereira et al., (2001)	$\mathrm{Re} = \frac{\rho \omega_o R_o (R_o - R_i)}{\mu}$
Escudier et al., (2000)	$\mathrm{Re} = \frac{2\rho \omega_o R_o (R_o - R_i)}{\mu}$ (Bulk axial Reynolds number)
	$\mathrm{Re} = \frac{\rho \omega_o R_o (R_o - R_i)}{\mu}$ (Rotational Reynolds number)

α is the measure of clearance ratio which is dimensionless parameter.

TABLE. 2 Reynolds Number Used in the Simulation

$R_o\,(cm)$	$R_i\,(cm)$	ω (RPM)	Re
7.62	5.08	10	20
		20	40
		30	60
		50	100
		100	200
	3.175	10	35
		20	70
		30	106
		50	177
		100	355
$\nu = 1\ cm^2/\sec$			

(Fig. 19(a)) the reattachment point moves in the opposite of the direction of rotation and the separation point shifts in the direction of the rotation. However, the reattachment point moves in the direction of the rotation at higher rotation speed (Fig. 19(b)). The separation point also shifts in the direction of rotation at higher rotation speed. San Andres and Szeri (1984) reported that the movements of the separation and reattachment points are governed by the eccentricity ratio. Between eccentricity ratios of 0.3 and 0.53, the separation point moves in the direction of rotation and the reattachment point moves in the opposite direction of rotation, which is similar to a low rotation speed case (Fig. 19(a)). At eccentricity ratios over 0.53, both separation and reattachment point shift in the direction of rotation, which is found in the simulation data at a high rotation speed (Fig. 19(b)). However, Fig. 19 clearly indicates that the consideration of both Reynolds number and eccentricity ratio are required to predict the position of the separation and reattachment points.

The eddy developments are also dependent on the radius ratio (R_i / R_o) or mean clearance ($c = R_o - R_i$). Fig. 20 shows that application of larger mean clearance results in the earlier development of the eddy than smaller clearance. This earlier development of the eddy is explained in section 4.4. The center of the eddy is more skewed to the direction of rotation in Fig. 20(d) than in Fig. 18(d). These two figures are computed under the same conditions except at different inner cylinder radii. The difference of the position of the eddy center in Fig. 18(d) and 19(d) is explained by the different amount of inertial force exerted on the fluid flow. Applying a smaller inner cylinder radius (R_i = 3.175 *cm*) increase the clearance and Reynolds number indicates greater importance of

inertial forces. The eddy development and inertial force effects on fluid flow as rotation speed increases are shown in Fig. 21. This figure shows that the eddy grows and is shifted in the direction of rotation as the Reynolds number is increased with rotation speed. At lower rotation speed the position of eddy is almost symmetric, even at large eccentricity ratios. This means that the effect of fluid inertia is negligible. As the speed of the outer cylinder is increased, the fluid inertial force plays an important role in determining the position of the eddy.

The influence of varying average velocity as eccentricity ratio increases is shown in Figs. 22 and 23. Fig. 22 simulates average angular velocity (u_η) change as eccentricity ratio increases with three different rotation speeds for two different inner cylinder radii. For small mean clearance (R_i = 5.08 *cm*), average angular velocity is lowered as eccentricity ratio is increased. However, when the eccentricity ratio is over 0.7 the average angular velocity does not change even when increasing eccentricity to 0.9. The reason for the stable angular velocity at high eccentricity ratio is that fluid is trapped in the eddy area. When the eccentricity ratio is increased, the clearance between inner cylinder and outer cylinder tends to zero. Thus, almost all the fluid is contained in the eddy at the largest clearance. A similar tendency is observed when a small inner cylinder (R_i = 3.175 *cm*) is applied. However, at high rotation speed (see Fig. 22(c)), average angular velocity is not decreased or stable, but increased. Radial direction velocity (u_ξ) in the eccentric rotation cylinder apparatus is small when compared to angular direction velocity (u_η). However, this velocity increases in keeping with

eccentricity ratio. Fig. 23 shows how the average radial direction velocity changes as eccentricity ratio changes. The average radial direction velocity is increased as eccentricity ratio is increased.

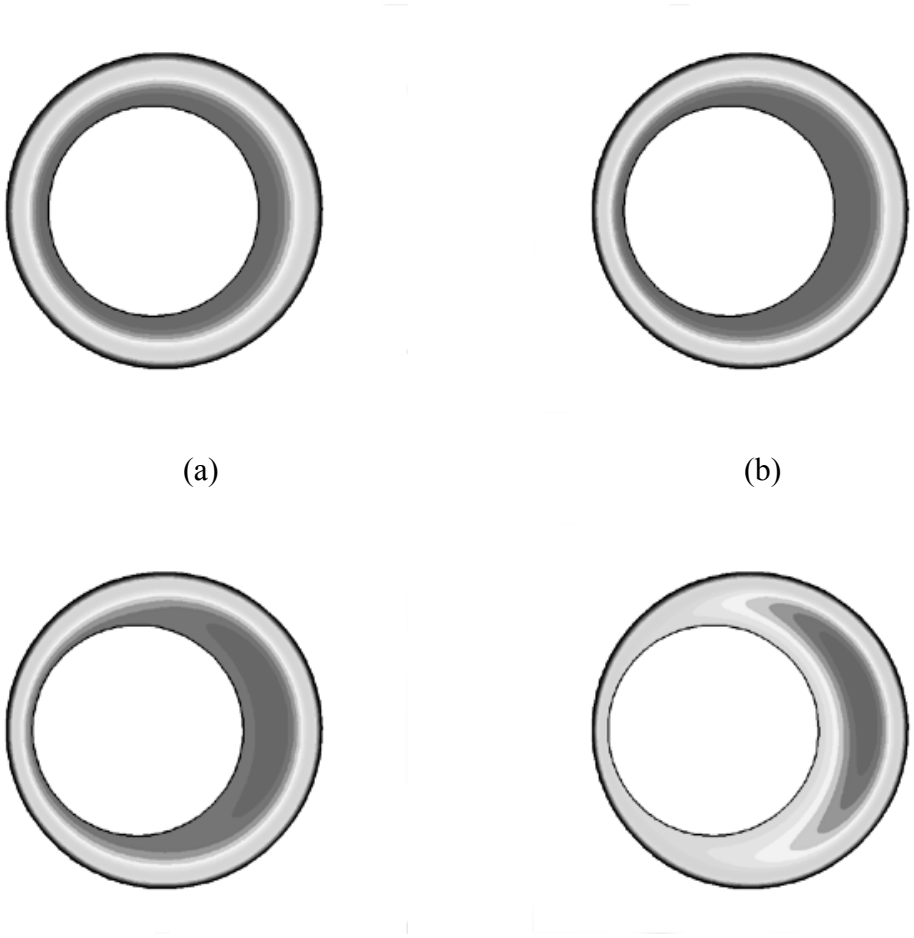

(a) (b)

(c) (d)

FIG. 18. Effects on streamlines of eccentricity ratio at fixed rotation speed ($\nu = 1\ cm^2/\sec$, $R_o = 7.62\ cm$, $R_i = 5.08\ cm$, $\omega = 20$ RPM); (a) $\varepsilon = 0.2$; (b) $\varepsilon = 0.4$; (c) $\varepsilon = 0.5$; (d) $\varepsilon = 0.7$

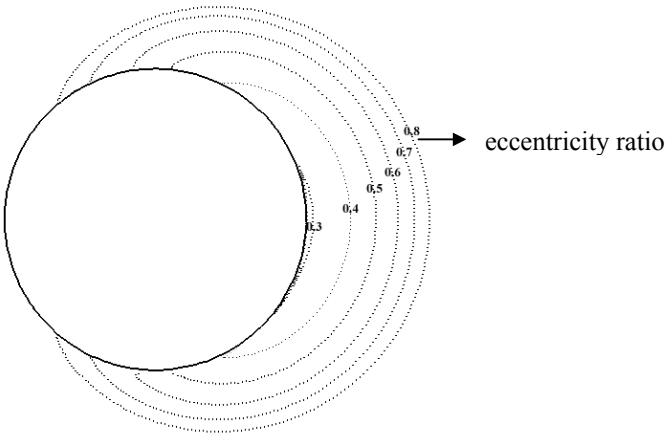

(a)

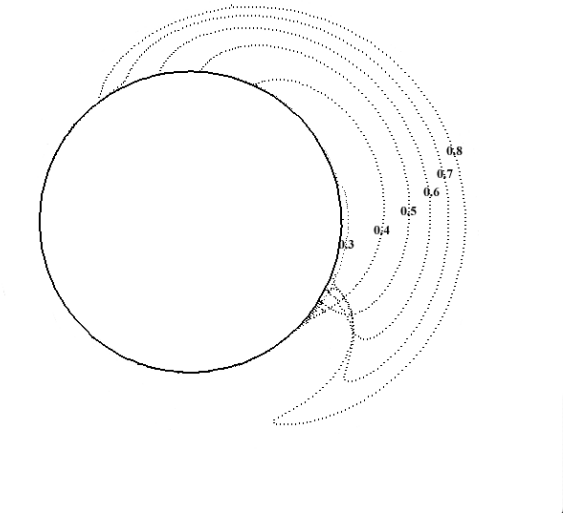

(b)

FIG. 19. Movements of the separation and reattachment points as eccentricity ratio increases ($\nu = 1\ cm^2/\sec$, R_o = 7.62 *cm*, R_i = 3.175 *cm*); (a) ω = 10 RPM; (b) ω = 50 RPM

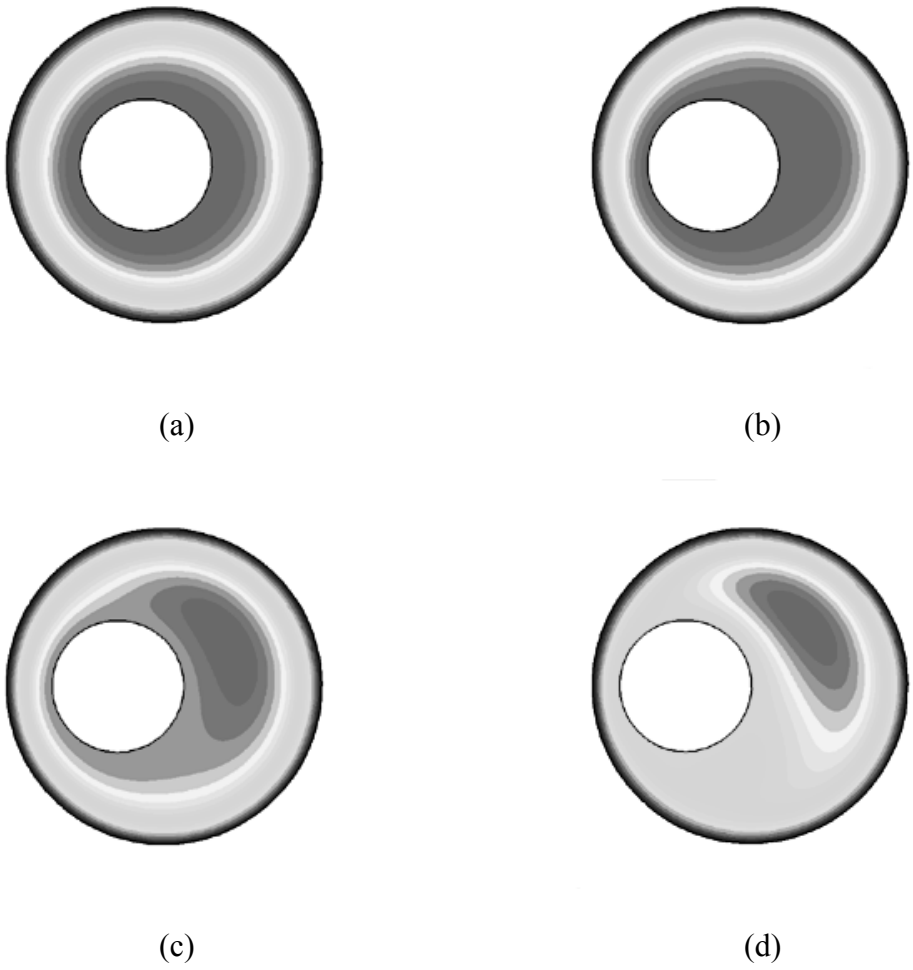

(a) (b)

(c) (d)

FIG. 20. Effects on streamline of increasing eccentricity ratio at fixed rotation speed ($\nu = 1\,cm^2/\sec$, $R_o = 7.62\ cm$, $R_i = 3.175\ cm$, $\omega = 20$ RPM); (a) $\varepsilon = 0.2$; (b) $\varepsilon = 0.4$; (c) $\varepsilon = 0.5$; (d) $\varepsilon = 0.7$

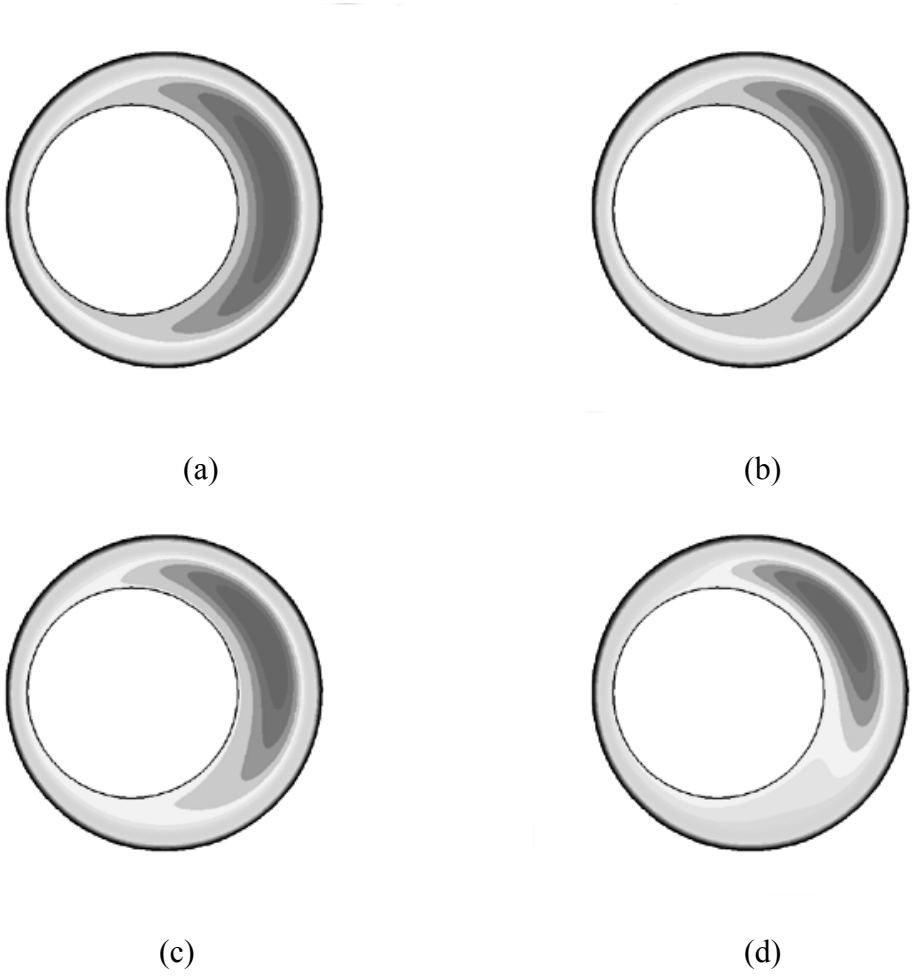

FIG. 21. Effects on streamlines of increasing rotation speed at fixed eccentricity (ν = $1\,cm^2/\sec$, R_o = 7.62 *cm*, R_i = 5.08 *cm*, ε = 0.6); (a) ω = 10 RPM; (b) ω = 30 RPM; (c) ω = 50 RPM; (d) ω = 100 RPM

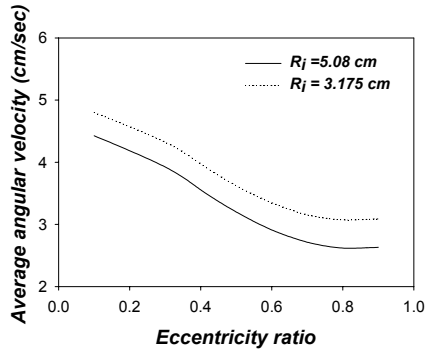

(a)

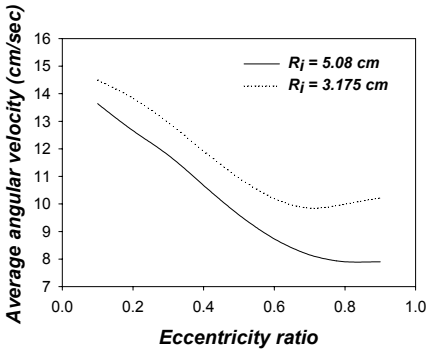

(b)

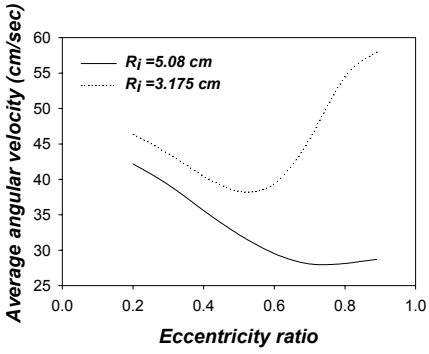

(c)

FIG. 22. Average angular direction velocity (u_η) changes with increasing eccentricity ratio ($\nu = 1.0$ cm^2/sec, $R_o = 7.62$ *cm*); (a) 10 RPM; (b) 30 RPM; (c) 100 RPM

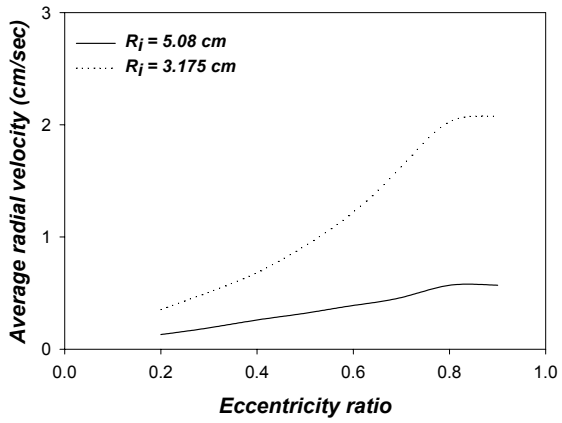

(a)

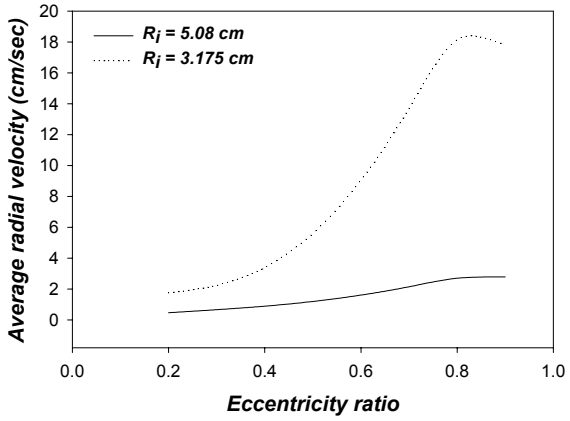

(b)

FIG. 23. Average radial direction velocity (u_ξ) as eccentricity ratio increases (ν = 1.0 cm^2/sec, R_o = 7.62 *cm*); (a) 30 RPM; (b) 100 RPM

4.4 Spatial Variance and Non-Uniform Velocity Distribution

The spatial variance and non-uniform velocity distribution of the eccentric rotating cylinder apparatus are generated by the development of the eddy in the wide clearance. Szeri and Al-Sharif (1995) showed that the pressure gradients cause eddy development near the stationary inner cylinder as the eccentricity ratio or rotation speed increases, The size of the eddy is increased with eccentricity ratio at fixed rotation speed (see Fig. 18 and 20). It is expected that the growth of the eddy size increase non-uniform velocity distributions.

Variance of angular velocity (u_η) as eccentricity ratio increases with two inner cylinder radiuses is shown in Fig. 24. Large inner cylinder radius (R_i= 5.08 *cm*) shows that the variance of angular velocity changes as eccentricity ratio increases by 0.5. Beyond an eccentricity ratio of 0.5, the variance of angular velocity is decreased. This is similar to the growth of the eddy size by shifting the inner cylinder from the center of outer cylinder. With increasing eccentricity ratio, the eddy appears near the stationary inner cylinder and grows in size. As the eddy expands, fluid flow near the stationary inner cylinder is in the opposite direction of the outer cylinder rotation, which causes the variance of angular velocity to increase until eccentricity ratio is equal to 0.5. Decease of the variance of angular velocity at high eccentricity ratio (beyond 0.5) is caused by trapping fluid in the eddy. By increasing eccentricity ratio, the clearance between the outer cylinder and inner cylinder is decreased. The eddy recirculating fluid in the wide clearance does not go through the narrow clearance zone. Therefore, almost all the fluid is contained in the eddy. However, when a smaller inner cylinder radius (R_o= 3.175 *cm*)

is applied, the variance of angular velocity shows a different tendency. Rotation speed is increased at high eccentricity ratio between 0.5 and 0.9. As eccentricity ratio increases from 0.5 to 0.9, the variance of angular velocity is less.

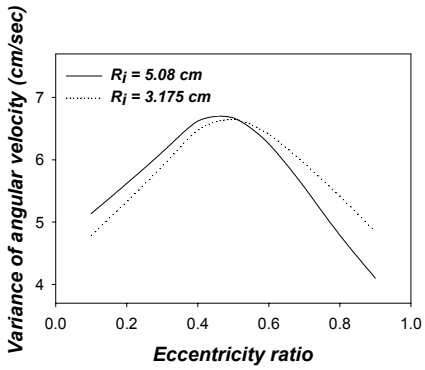

(a)

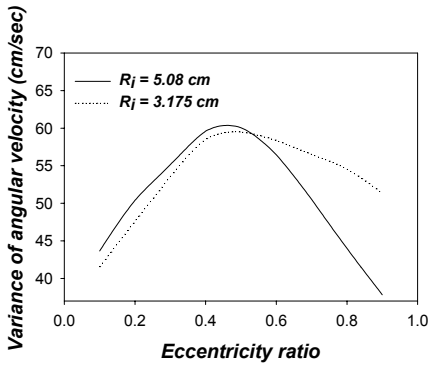

(b)

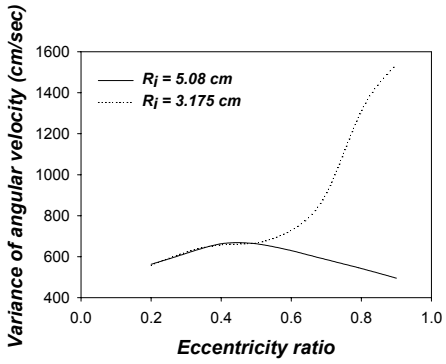

(c)

FIG. 24. Variance of angular velocity as eccentricity ratio increases ($\nu = 1.0$ cm^2/sec, $R_o = 7.62\ cm$); (a) 10 RPM; (b) 30 RPM; (c) 100 RPM

4.5 RMS Velocity Gradient and Mean Principal Strain-rate.

The root-mean-square velocity gradient and average principal strain-rate were obtained in order to apply the eccentric rotating cylinder apparatus to coagulation studies. The root-mean-square velocity gradient is calculated from the mechanical power consumption that is needed to rotate the outer cylinder and the volume of fluid in eccentric rotating cylinder apparatus (see (67)). Fig. 25 shows that $\overline{G}$ changes as eccentricity ratio and rotation speed increase. At low rotation speed (10 RPM), $\overline{G}$ is not affected by the location of inner cylinder, even when eccentricity ratio is greater than 0.5 for both R_i = 3.175 *cm* and R_i = 5.08 *cm*. However, rotation speed increases $\overline{G}$ changes with eccentricity ratio. With R_i = 5.08 *cm*, $\overline{G}$ increases in keeping with eccentricity ratio. When eccentricity ratio reaches 0.8, $\overline{G}$ shows a sudden increase. With R_i = 3.175 *cm*, $\overline{G}$ shows similar behavior with eccentricity ratio. However, at 100 RPM, $\overline{G}$ shows a rapid increase when eccentricity ratio is over 0.6. This is similar to the result of the variations of angular velocity with increasing eccentricity ratio in Fig. 24. Average principal strain-rate values are obtained in both Stokes and inertial flow with (64). Fig. 26 shows that $\overline{|a_{\max}|}$ increases consistently with eccentricity ratio in Stokes flow. For inertial flow, $\overline{|a_{\max}|}$ slightly increase at low rotation speed 10 to 50 RPM. As rotation speed increases over 50 RPM, the increase of $\overline{|a_{\max}|}$ is divided in two regions. When eccentricity ratio is under 0.6, the increase of $\overline{|a_{\max}|}$ corresponds to low rotation speed

cases between 10 to 50 RPM. However, as eccentricity ratio is above 0.7, $\overline{|a_{\max}|}$ shows a sudden rise at 100 RPM. Fig. 27 shows that $\overline{|a_{\max}|}$ increases in keeping with rotation speed.

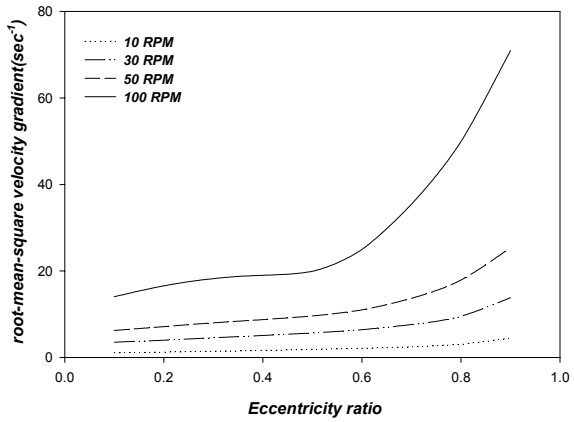

(a)

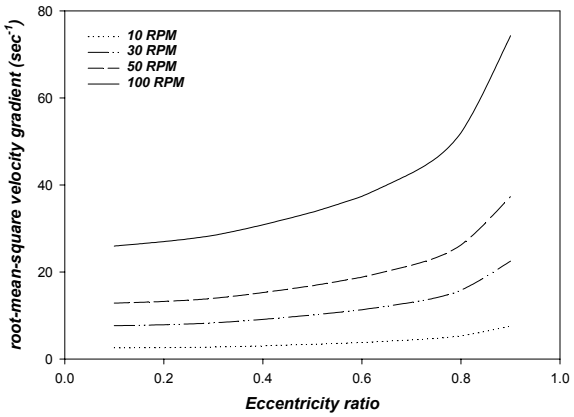

(b)

FIG. 25. Root-mean-square velocity gradient ($\overline{G}$) as a function of rotation speed and eccentricity ratio ($v = 1\ cm^2$/sec, $R_o = 7.62\ cm$); (a) $R_i = 3.175\ cm$; (b) $R_i = 5.08\ cm$

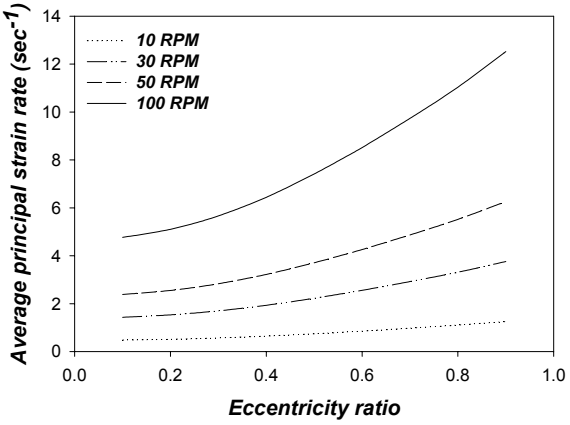

(a)

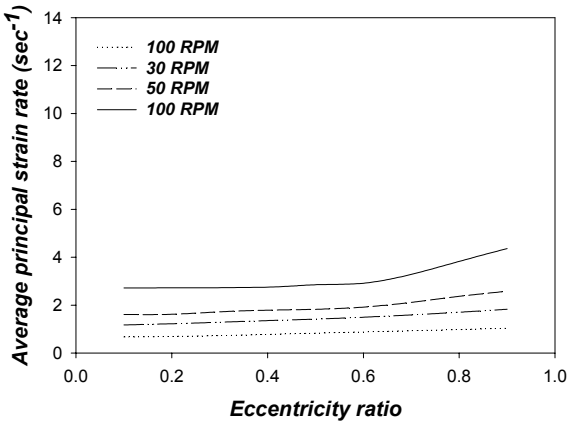

(b)

FIG. 26. Average principal strain-rate ($\overline{|a_{\max}|}$) as a function of rotation speed and eccentricity ratio ($R_o = 7.62\ cm,\ R_i = 3.175\ cm$); (a) Stokes flow; (b) Inertial flow ($\nu = 1\ cm^2/\sec$)

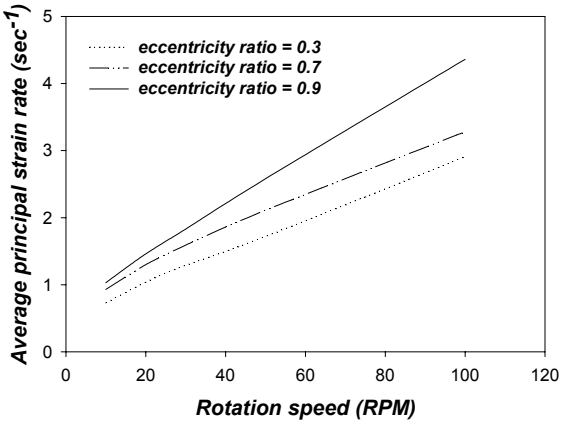

(a)

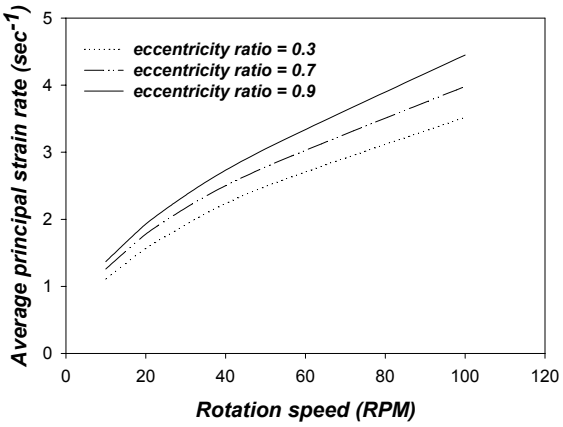

(b)

FIG. 27. Average principal strain-rate ($\overline{|a_{\max}|}$) with rotation speed; ($\nu = 1\ cm^2$ /sec, $R_o =$ 7.62 *cm*); (a) $R_i = 3.175\ cm$; (b) $R_i = 5.08\ cm$

4.6 Comparison with Thomas (1999)

Thomas (1999) conducted experiments to verify the Stokes method for the eccentric rotating cylinder apparatus. Flow visualization was achieved through use of a green dye and aluminum powder. The kinematic viscosity of the fluid was carefully controlled using a glycerin and water mixture. The dimensions of the apparatus used in Thomas (1999) are that an outer cylinder radius was 7.62 cm, and two inner cylinder radii were 3.175 cm and 5.08 cm. The depth of the cylinder was 20.32 cm and the ratio of length per outer cylinder diameter was 1.33 cm. Fig. 28(i) shows streamline development with $\nu = 0.6689$ cm^2/sec. Fig. 28(a) shows that when outer cylinder rotates 30 RPM in the counterclockwise direction, the eddy formed is slightly skewed in the rotating direction by the inertial forces. Fig. 28(b) shows that the separation point shifts further to the rotation direction with increasing rotation speed. This is consistent with simulated streamlines in Fig. 21. The reattachment point moves in the direction opposite of the rotation in comparisons with Fig. 28 (a) and (b). This corresponds to Fig. 19 (a) for low rotation speed (10 RPM). Comparisons Fig. 28 (a) and (b) with Fig. 28(b) and (c) show that the size of eddy grows and more inertial forces work on fluid flow with eccentricity ratio. However, by applying small inner cylinder ($R_i = 3.175\ cm$), the model fails to predict the streamlines accurately with increasing the mean clearance. Fig. 29 shows that increasing the mean clearance causes the failure of the model prediction even at a small eccentricity ratio. The increase of the mean clearance ratio increases Reynolds number. As Reynolds number increases over 300, model cannot accurately predict the flow streamlines. The eccentricity ratio of Fig. 29(a) is 0.3 and (b) is 0.67. Both cases

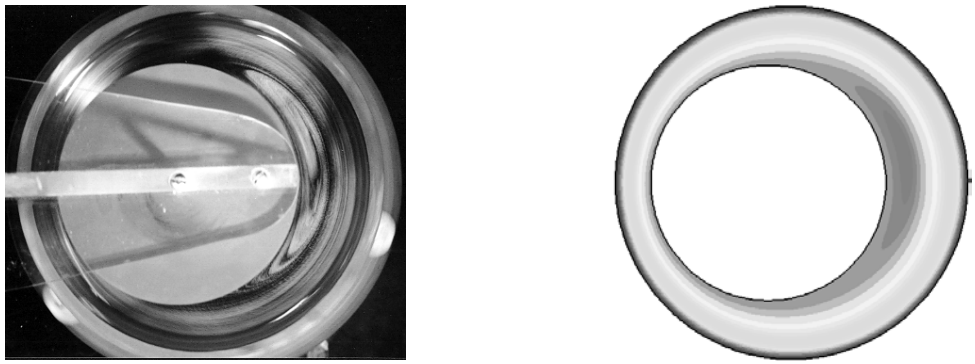

(i) (ii)

(a)

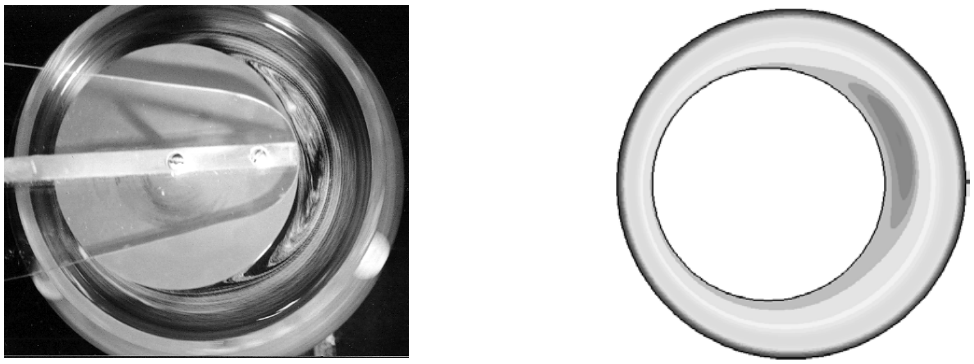

(i) (ii)

(b)

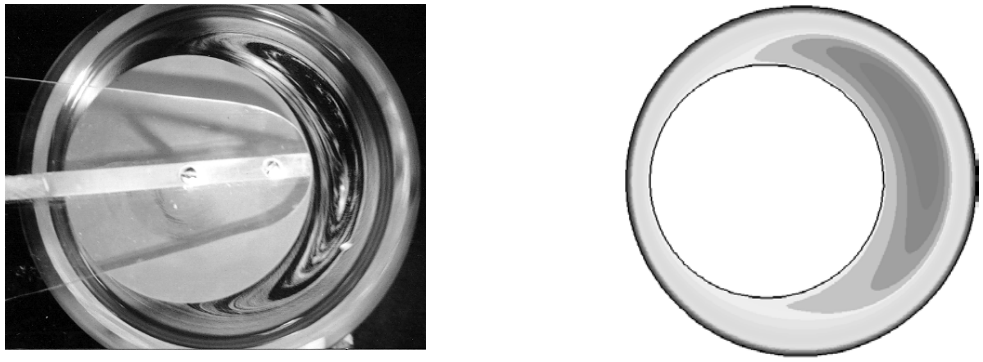

(i) (ii)

(c)

FIG. 28. Streamline Developments Comparisons of (i) Thomas (1999) and (ii) Simulation (ν = 0.6689 cm^2/sec, R_o = 7.62 cm, R_i = 5.08 cm); (a) ε =0.39, ω = 30RPM, Re = 90; (b) ε = 0.39, ω = 60 RPM, Re = 182; (c) ε = 0.59, ω = 60 RPM, Re = 182

fail to predict streamlines. The failure of simulation results at high values of the Reynolds number is caused by the subsequent terms of the perturbation series and the series diverges in inertial analytical solution. As series are diverged, the error of the perturbation is increased. Comparison of computational simulation based on the modified solutions of Ballal and Rivlin (1976) with experimental results for fluid motions in an eccentric rotating cylinder apparatus shows good agreement for Reynolds number smaller than 200.

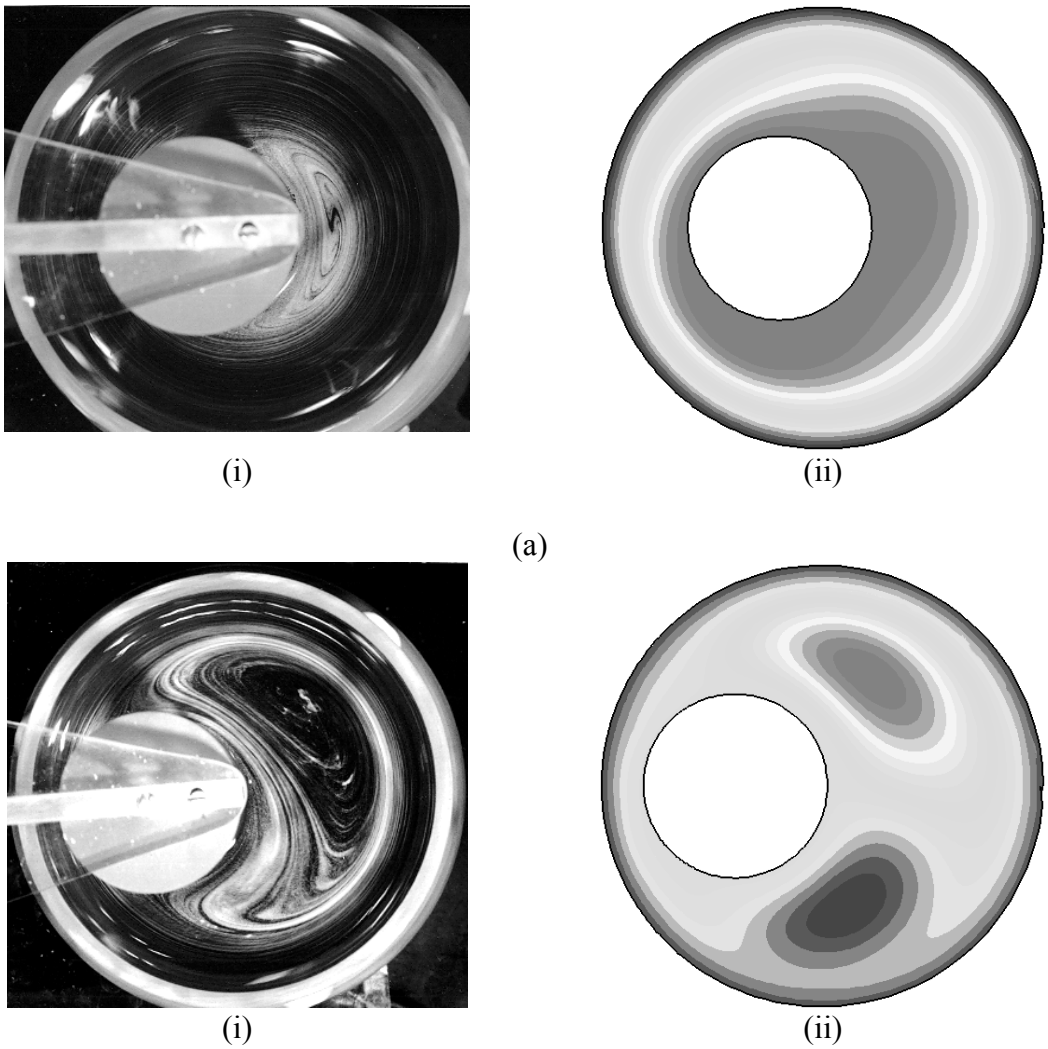

FIG. 29. Streamline Developments Comparisons of (i) Thomas (1999) and (ii) Simulation (ν = 0.6689 cm^2/sec, R_o = 7.62 *cm*, R_i = 3.175 *cm*, Re = 318); (a) ε =0.34, ω = 60RPM; (b) ε = 0.67, ω = 60 RPM

CHAPTER IV

SUMMARY AND CONCLUSIONS

van Duuren (1968) investigated concentric rotating cylinders as a model flocculator and suggested that a model flocculator must be easy to handle, generate two-dimensional laminar flow, and develop shear velocity gradients. Finally, fluid dynamics in the flow must be well-defined. The eccentric rotating cylinders apparatus has two parallel cylinders like the concentric rotating cylinder device and is based on a journal bearing system (Swanson and Ottino, 1990). However, the only difference is that the inner cylinder is located eccentrically. Therefore, requisites for a model flocculator (easy to handle, two-dimensional laminar flow, and shear velocity gradients) are satisfied. In this study, fluid dynamics for the eccentric rotating cylinder apparatus were examined using the modified analytical solution of Ballal and Rivlin (1976) of various eccentricity ratios and rotation speeds.

The Stokes method was identified as not being an appropriate method for the study of coagulation, because general coagulation studies require various mixing intensities and fluid viscosities. As mixing intensity increases, inertial effects working on the fluid increase. Thus, the inclusion of the inertial approximation was determined as a proper method to investigate the fluid dynamics of the eccentric rotating cylinder.

As eccentricity ratio increased at a fixed rotation speed, inertial forces working on the fluid caused the shifting of the position of the eddy in the direction of rotation. At low eccentricity ratio, the eddy was symmetric, however, as eccentricity increases the

position of the eddy was skewed to the direction of rotation. Inertial forces were increased by applying a smaller inner cylinder or increasing rotation speed. The simulation with a small inner cylinder radius (R_i = 3.175 *cm* showed that the eddy appeared earlier even at smaller eccentricity ratio and that the center of the eddy was more skewed in the direction of rotation than for the larger inner cylinder radius (R_o = 5.08 *cm*). When the rotation speed was increased at a fixed eccentricity ratio, the position of the eddy was almost symmetric, even at a large eccentricity ratio. As the rotation speed reaches 100 RPM, the eddy moves in the direction of rotation and the separation point shifts to the narrow gap. These results clearly indicated that inertial forces working on the fluid could be estimated from Reynolds number, because the Reynolds number increases with rotation speed.

The investigation of eddy separation and reattachment points with two different rotation speeds showed that at a low rotation speed (10 RPM) the separation point shifts in the direction of rotation. However, the reattachment point moved opposite the direction of rotation. At a high rotation speed (100 RPM), both the separation and reattachment point moved in the direction of rotation. Therefore, consideration of both eccentricity ratio and Reynolds number is required to predict the position of the separation and reattachment points.

The average angular velocity showed that when the rotation speed was below 30 RPM the average angular velocity decrease with increasing eccentricity ratio and reached a steady state. Average angular velocity (u_η) was lowered as eccentricity ratio increases. However, when the eccentricity ratio was over 0.7 the average angular

velocity reached steady state even when eccentricity ratio was increased to 0.9. Variance of angular velocity also showed a certain pattern when the rotation speed is kept under 30 RPM. The variance of angular velocity showed that variance increased as eccentricity ratio increased to 0.5. However, after 0.5, the variance of angular velocity declined. Both the steady state conditions of average angular velocity and the decreasing in the variance of angular velocity were caused by fluid entrapment inside of the eddy, when eccentricity ratio is beyond 0.7 and 0.5.

The root-mean-square velocity gradient and average principal strain-rate increased in keeping with eccentricity ratio. This clearly indicated that increasing spatial variations of fluid dynamics increased both $\overline{G}$ and $\overline{|a_{\max}|}$. $\overline{|a_{\max}|}$ increased linearly with rotation speed, which suggested that $\overline{|a_{\max}|}$ can properly represent mixing intensity.

Finally, comparison of model streamlines and experimentally developed streamlines in Thomas (1999) showed that when larger inner cylinder radius (R_i = 5.08 *cm*) was applied, the model generated streamlines were in good agreement with streamlines in Thomas (1999). However, when the smaller inner cylinder (R_i = 3.175 *cm*) was simulated, the model failed to predict the proper development of the streamlines. This failure is caused by inaccuracies of perturbation series divergence in the inertial analytical solution of Ballal and Rivlin (1976) with increasing Reynolds number.

In conclusion, the eccentric rotating cylinder apparatus was found to be applicable for the study of particle coagulation as a model flocculator. However, some operating limitations are required.

1. Fluid Reynolds number must keep below 200 in order to obtain reliable model simulation.
2. It is recommended that small mean clearance ($R_o - R_i$) should be applied in order to maintain low Reynolds number at various mixing intensities.
3. Using a large mean clearance requires the use of a high viscosity fluid to maintain low Reynolds number.

REFERENCES

Argaman, Y., and Kaufman, W. J. (1970). "Turbulence and flocculation." *J. Sanit. Eng. Div., ASCE*. 96(SA2), 223-241.

Ashino, I., and Yoshida, K. (1975). "Slow motion between eccentric rotating cylinders." *Belletin, Japan Soc. Mech Eng*., 18, 280-285

Ballal, B.Y., and Rivlin, R.S. (1976). "Flow of a Newtonian fluid between eccentric rotating cylinders." *Arch. Rational Mech. Anal.,* 62, 237-294.

Batchelor, G. K. (1992). *An introduction to fluid dynamics.* Cambridge University Press, Cambridge, U.K.

Blaser, S. (2000). "Floc in shear and strain flows." *J. Colloid and Interface Sci.,* 225, 273-284.

Boller, M., and Blaser, S. (1998). "Particle under stress." *Water Sci. Technol.,* 37(10), 9-29.

Bouyer, D., Line, A., Cockx, A., and Do-Quang, Z. (2001). "Experimental Analysis of Floc Size Distribution and Hydrodynamics in a Jar-Test." *Trans. IChemE*., 79(A), 1017-1024.

Camp, T. R., and Stein, P. C. (1943). "Velocity-gradients and internal work in fluid motion." *J. Boston. Soc. of Civ. Engrs.*, 30(4), 219-237.

Clark, M. M. (1986). "Critique of Camp and Stein's RMS velocity gradient." *J. Envir.-Engrg. Div.,*ASCE, 111(3), 741-754.

Clark, M. M. (1996). *Transport modeling for Environmental Engineers and Scientists*. Wiley Interscience, New York, N.Y.

Clark, M. M., and Flora, R. V. (1991). "Floc restructuring in varied turbulent mixing." *J. Colloid and Interface. Sci*., 147(2), 407-421.

Cleasby, J. L. (1984). "Is velocity gradient a valid turbulent flocculation parameter?." *J. Envir. Engrg. Div.,ASCE*, 110(5), 875-897.

Diprima, R. C., and Stuart, J. T. (1972). "Flow between eccentric rotating cylinders." *J. Lubric. Tech. – T. ASME*., F94, 266-274.

Ducoste, J. J. (1996). *The effects of tank size and impeller type on turbulent flocculation*. Ph. D. Thesis, University of Illinois, Urbana, IL.

Ducoste, J. J., and Clark, M. M. (1998). "The Influence of tank size and impeller geometry on turbulent flocculation : I. Experimental." *Environ. Eng. Sci.,* 15(3), 225-235.

Escudier, M.P., Gouldson, I.W., Oliveira, P.J., and Pinho, F.T. (2000). "Effects of inner cylinder rotation on laminar flow of a Newtonian fluid through an eccentric annulus." *Int. J. Heat and Fluid Flow*., 21, 92-103.

Glasgow, L. A., and Liu, X. (1991). "Response of aggregate structures to hydrodynamic stress." *AIChE J*., 37(9), 1411-1414.

Gmachowski, L. (2000). "Estimation of the dynamic size of fractal aggregates*." Colloid Surface A.,* 170, 209-216.

Graber, S.D. (1994). "A critical review of the use of G-value (RMS velocity gradient) in environmental engineering." *Proc.,17th South Eastern Conf. On Theoretical and Appl. Mech., Developments in Theoretical and Appl. Mech.,* Vol. 16. University of Arkansas, Fayetteville, AR, 553-556.

Gruy, F. (2001). "Formation of small silica aggregates by turbulent aggregation," *J.Colloid and Interface. Sci.,* 237, 28-39.

Higashitani, K., and Iimura, K. (1998). "Two-dimensional simulation of the breakup process of aggregates in shear and elongational flows." *J. Colloid and Interface. Sci*., 204, 320-327.

Higashitani, K., Yamauchi, K., Matsuno, Y., and Hosokawa, G. (1983). "Turbulent coagulation of particles dispersed in a viscous fluid." *J. Chem. Eng. Jpn.,* 16(4), 299-304

Hubley, C. E., Robertson, A. A., and Mason, S. G. (1950). "Flocculation in suspensions of large particles*." Can. J. Res*. 28(B), 770-787.

Ives, K. J., and Dibouni, M. AL. (1979). "Orthokinetic flocculation of latex microspher-es." *Chem. Eng. Sci*., 34, 989-991.

Jiang, Q., and Logan, B. E. (1991). "Fractal dimension of aggregates determined from steady-state size distributions." *Envir. Sci. Technol*., 25, 2031-2038.

Jiang, Q., and Logan, B. E. (1996). "Fractal dimensions of aggregates from shear device." *J. AWWA*., 88, 100-113.

Kamal, M. M. (1966). "Separation in the flow between eccentric rotating cylinders." *J. Basic Eng.-T. ASME*., 88, 717-724.

Kao, S.V., and Mason, S.G. (1975). "Dispersion of particles by shear." *Nature.*, 253, 619-621.

Kramer, T. A., and Clark, M. M. (1997). "Influence of strain-rate on coagulation kinetics." *J. Envir. Engrg. Div., ASCE,* 123(5), 444-452.

Kramer, T.A., and Clark, M. M. (1999). "Incorporation of aggregate breakup in the simulation of orthokinetic coagulation." *J. Colloid and Interface. Sci*., 216, 116-126.

Kramer, T. A., and Clark, M. M. (2000). "Modeling orthokinetic coagulation in spatially varying laminar flow." *J. Colloid and Interface. Sci.,* 227, 251-261.

Kumar, S., and Homsy, G. M. (1996). "Chaotic advection in creeping flow of viscoelastic fluids between slowly modulated eccentric cylinders." *Phys. Fluids*., 8(7), 1774-1787.

Levich, V. G. (1962). "*Physicochemical hydrodynamics*. Prentice-Halls, Inc., Englewood Cliffs, N.J.

Lin, M. Y., Lindsay, H. M., Weitz, D. A., Ball, R. C., Klein, R., and Meakin, P. (1989). "Universality in colloid aggregation." *Nature.*, 339, 360-362.

Mandekbrot, B. B. (1983). *The fractal geometry of nature*. W. H. Freeman, New York, N.Y.

McConnachie, G. L. (1991). "Turbulence intensity of mixing in relation to flocculation." *J. Envir. Engrg. Div.,*ASCE, 117(6), 731-750.

Meakin, P. (1988). "Fractal aggregates." *Adv. Colloid. Interfac*., 28, 249-331.

Meakin, P. (1998) *Fractal scaling and growth far from equilibrium*. Cambridge University Press, Cambridge, U.K.

Oldshue, J. Y., and Mady, O. B. (1978). "Flocculation performance of mixing Impellers." *Chem. Eng. Prog.,* 74(8), 103-108.

Oldshue, J. Y., and Mady, O. B. (1979). "Flocculator impellers: A comparison." *Chem. Eng. Prog.,* 75(5), 72-75.

Oles, V. (1992). “Shear-induced aggregation and breakup of polystyrene latex particles.” *J. Colloid and Interface. Sci.,* 154(2), 351-358.

Parker, D. S., Kaufman, W. J. and Jenkins, D. (1972). “Floc breakup in turbulent flocculation processes.” *J. Sanit. Eng. Div., ASCE*, 98(SA1), 79-99.

Pereira, A., McGrath, G., and Joseph, D. D. (2001). “Flow and stress induced cavitation in a journal bearing with axial throughput.” *J. Tribol - T. ASME*., 123(4), 742-754.

Powell, R.L., and Mason, S.G. (1982). “Dispersion by laminar flow.” *AIChE J.*, 28(2), 286-293.

Saffman, P. G., and Turner, J. S. (1956). “On the collision of drops in turbulent clouds.” *J. Fluid Mech*., 1(16)

San Andres, A., and Szeri, A. Z. (1984). “Flow between eccentric rotating cylinders.” *J. Appl. Mech*., 51(12), 869-878.

Selomulya, C., Bushell, G., Amal, R., and Waite, T. D. (2002). “Aggregation mechanisms of latex of different particle sizes in a controlled shear environment.” *Langmuir*., 18, 1974-1984.

Serra, T., and Casamitjana, X. (1998). “Structure of the aggregates during the process of aggregation and breakup under a shear flow.” *J. Colloid and Interface*. *Sci*., 206, 505-511.

Serra, T., Colomer, J. and Casamitjana, X. (1997). “Aggregation and Breakup of Particles in a Shear Flow.” *J. Colloid and Interface. Sci.* 187, 466-473.

Smith, D. K. W., and Kitchener, J. A. (1978). “The strength of aggregates formed in flocculation.” *Chem. Eng. Sci*., 33,1631-1636.

Smoczynski, L., and Wardzynska, R. (1996). “Study on macroscopic aggregation of silica suspensions and sewage.” *J. Colloid and Interface. Sci*., 183, 309-314.

Smoluchowski, M.V. (1917). “Versuch einer mathematishcen theorie der koagulationsknetik kolloider losungen.” *Zeitschrift fur Physikalische Chemie*, 92, 129-168.

Spicer, P. T., Keller, W., and Pratsinis, S. E. (1996). “The effect of impeller type on floc size and structure during shear-induced flocculation.” *J. Colloid and Interface. Sci.,* 184(1), 112-122.

Swanso, P. D. and Ottino, J. M. (1990). "A comparative computational and experimental study of chaotic mixing of viscous fluids." *J. Fluid Mech*., 213, 227-249.

Swift, D. L., and Friedlander, S. K. (1964). "The coagulation of hydrosols by Brownian motion and laminar shear flow." *J. Coll. Sci.,* 19, 621-647

Szeri, A.Z., and Al-Sharif, A. (1995). "Flow between finite, steadily rotating eccentric cylinders." *Theoret. Comput. Fluid Dynamics*., 7, 1-28.

Taylor, G.I. (1923). "Stability of a viscous liquid contained between two rotating cylinders." *Philos. T. Roy. Soc. A.,* 223,289-346.

Taylor, G.I. (1934). "The formation of emulsions in definable fields of flow." *Proc. Royal. Soc.,*146A, 501-523.

Thill, A., Moustier, S., Aziz, J., Wiesner, M. R., and Bottero, J. Y. (2001). "Floc restructuring during aggregation: experimental evidence and numerical simulation." *J. Colloid and Interface. Sci*., 243, 171-182.

Thomas, C. J. (1999). *Design and analysis of an improved apparatus for the study of mixing and coagulation*. M.S. Thesis, Aurburn University, Auburn, AL.

Thomas, D. G. (1964). "Turbulent of flocs in small particle size suspensions." *AIChE. J*., 10(4), 517-523.

Trevelyan, B. J., and Mason, S. C. (1951). "Particle motions in shared suspensions: I. Rotations." *J. Coll. Sci*., 6, 354-367

van Duuren, F. A. (1968). "Defined velocity gradient model flocculator." *J. Sanit. Eng. Div., ASCE,* 94, 671-682.

Vohr, J. H. (1968). "An experimental study of Taylor vortices and turbulence in flow between eccentric rotating cylinders." *J. Lubri. Tech. – T. ASME*., 67, 285-296.

Wannier, G. H. (1950). "A contribution to the hydrodynamics of lubrication." *Q. Appl. Maths*., 8, 1-32.

Weetman, R.J., and Oldshue, J.Y., and Colye, C. (1988). "Comparison of mass transfer characteristics of radial and axial impellers." *6th European Conference on Mixing*., Pavia, Italy, 345-350.

White, F. M. 1991. *Viscous fluid flow*. McGraw-Hill Book Co., Inc., New York, N.Y.

Wood, W. W. (1957). "The asymptotic expansions at large Reynolds number for steady

motion between non-coaxial rotating cylinders." *J. Fluid Mech*., 3, 159-175.

Wray, A. A., and Hunt, J. C. R. (1990). "Algorithms for classification turbulent structures." In: Moffatt, H. K., and Tsinober, A. (eds.) *Topological fluid mechanics, Proc. IUTAM Symp,* Cambridge, Cambridge Univ. Press, 95-104.

Yamada, Y., and Nakabayashi, Koichi. (1968). "On the flow between eccentric rotating cylinders when the outer cylinder rotates." *Belletin, Japan Soc. Mech Eng*., 11(45), 455-462.

Zollars, R. L., and Ali, S. I. (1986) "Shear coagulation in presence of repulsive interparticle forces." *J. Colloid and Interface. Sci.,* 114, 149-166

APPENDIX I

Derivation of Velocity Gradient, Strain-Rate, Vorticity Tensor

In order to derive the velocity gradient, strain-rate and vorticity tensors, consider the displacement and distortion of a fluid element due to fluid motion. When force is exerted on a fluid element, four different types of motion or deformation develop: translation, extensional or dilation, shear, and rotation. The distortions of a fluid element such as extensional, dilation and shear strain are called the strain-rate tensor, which is the rate of deformation by external fluid forces. The orientation of a material vector of a fluid element is named the vorticity tensor. Displacement and deformation of a fluid element by external fluid force is shown in Fig. I-1, which clearly displays the four motions (translation movement of reference corner A to E), dilation (EFGH looks a little bigger), shear strain (the lozenged shape of EFGH), and rotation (the change of angle BAC and BAG)). The displacement of ABCD into EFGH can be defined in matrix form.

$$\begin{pmatrix} x' \\ y' \end{pmatrix} = \begin{bmatrix} O_{11} & O_{12} \\ O_{21} & O_{22} \end{bmatrix} \begin{pmatrix} x \\ y \end{pmatrix} \tag{I.1}$$

To solve this matrix, the displacement of each of the points, A, B, C, and D in terms of a displacement field $u = u(x, y)$ and $v = v(x, y)$ is required. The first consideration is displacement of A to E. By assuming that A has coordinate (x, y), then the E is defined $(x + u, y + v)$. Then transformation of A to E is defined as

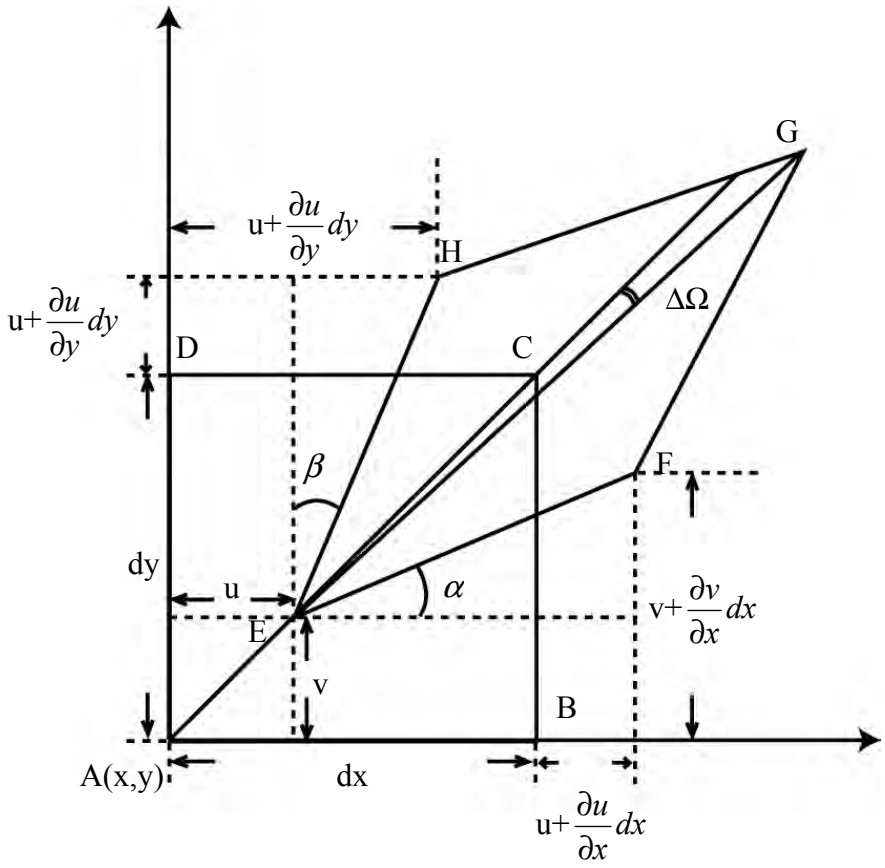

FIG. I-1. Orientation and Distortion of a Fluid Element ABCD to EFGH

$$\begin{pmatrix} x+u \\ y+v \end{pmatrix} = \begin{bmatrix} O_{11} & O_{12} \\ O_{21} & O_{22} \end{bmatrix} \begin{pmatrix} x \\ y \end{pmatrix} \tag{I.2}$$

The transformation of B to E is expressed as a

$$x' = x + dx + u(x + dx, y),\ y' = y + v(x + dx, y)$$

By expanding u and v in a Taylor series approximation, transformed point F can be defined as a

$$x' = x + dx + u + \frac{\partial u}{\partial x}dx + \frac{1}{2!}\frac{\partial^2 u}{\partial x^2}(dx)^2 + \cdots$$

$$y' = y + v + \frac{\partial v}{\partial x}dx + \frac{1}{2!}\frac{\partial^2 v}{\partial x^2}(dx)^2 + \cdots$$

By assuming that *dx* is sufficiently small (close to zero), the terms of higher order can be neglected. So transformation of B to F in matrix form is

$$\begin{pmatrix} x + u + dx + \frac{\partial u}{\partial x}dx \\ y + v + \frac{\partial v}{\partial x}dx \end{pmatrix} = \begin{bmatrix} O_{11} & O_{12} \\ O_{21} & O_{22} \end{bmatrix} \begin{pmatrix} x + dx \\ y \end{pmatrix} \tag{I.3}$$

With the same approach, transformation of C and D into G and H are

$$\begin{pmatrix} x + u + \frac{\partial u}{\partial y}dy \\ y + v + dy + \frac{\partial v}{\partial y}dy \end{pmatrix} = \begin{bmatrix} O_{11} & O_{12} \\ O_{21} & O_{22} \end{bmatrix} \begin{pmatrix} x \\ y + dy \end{pmatrix} \tag{I.4}$$

and

$$\begin{pmatrix} x + dx + u + \frac{\partial u}{\partial x}dx + \frac{\partial u}{\partial y}dy \\ y + dy + v + \frac{\partial v}{\partial x}dx + \frac{\partial v}{\partial y}dy \end{pmatrix} = \begin{bmatrix} O_{11} & O_{12} \\ O_{21} & O_{22} \end{bmatrix} \begin{pmatrix} x + dx \\ y + dy \end{pmatrix} \tag{I.5}$$

respectively. The matrix (I.2), (I.3), (I.4), and (I.5) give rise to simultaneous equations and the solution is

$$\begin{pmatrix} x' \\ y' \end{pmatrix} = \begin{bmatrix} O_{11} & O_{12} \\ O_{21} & O_{22} \end{bmatrix} \begin{pmatrix} x \\ y \end{pmatrix} + \begin{bmatrix} \frac{\partial u}{\partial x} & \frac{\partial u}{\partial y} \\ \frac{\partial v}{\partial x} & \frac{\partial v}{\partial y} \end{bmatrix} \begin{pmatrix} x \\ y \end{pmatrix} \tag{I.6}$$

where the first equation of right hand side represents identity matrix and the second matrix represents velocity gradient. A physical interpretation of velocity gradient (relative motion of a fluid element) is consisted of strain arte and vorticity and defined as a

$$\begin{bmatrix} \frac{\partial u}{\partial x} & \frac{\partial u}{\partial y} \\ \frac{\partial v}{\partial x} & \frac{\partial v}{\partial y} \end{bmatrix} = \begin{bmatrix} a_{11} & a_{22} \\ a_{21} & a_{22} \end{bmatrix} + \begin{bmatrix} \omega_{11} & \omega_{12} \\ \omega_{21} & \omega_{22} \end{bmatrix}$$

where the first matrix on the right hand side is a symmetric matrix called strain-rate and the second is an antisymmetric matrix called vorticity. Strain-rate is divided into normal strain-rate and shear strain-rate. Normal strain-rate is defined as the rate of change of length per unit of original length. By assuming that the angle of α and β are small, so normal strain-rate for a fluid element in Fig. I. 1 is expressed as

$$a_{11} = \frac{dx + \frac{\partial u}{\partial x} dx - dx}{dx} = \frac{\partial u}{\partial x} \qquad a_{22} = \frac{dy + \frac{\partial v}{\partial y} dy - dy}{dy} = \frac{\partial v}{\partial y} \tag{I.7}$$

where a_{11} represents x direction and a_{22} for y direction. By considering deformation of a fluid element without extensional strain-rate and rotation, pure shear strain-rate will be obtained. Fig. I-2 shows a fluid element motions by pure strain-rate. The matrix equations for the deformed square a) and b) are given as

$$\begin{pmatrix} x' \\ y' \end{pmatrix} = \begin{bmatrix} 1 & 0 \\ \alpha & 1 \end{bmatrix} \begin{pmatrix} x \\ y \end{pmatrix} \text{ and } \begin{pmatrix} x' \\ y' \end{pmatrix} = \begin{bmatrix} 1 & \beta \\ 0 & 1 \end{bmatrix} \begin{pmatrix} x \\ y \end{pmatrix}$$

respectively. The multiplication of matrix for a) and b) produces matrix for c) in Fig. I.2 and expressed as

$$\begin{pmatrix} x' \\ y' \end{pmatrix} = \begin{bmatrix} 1 & \beta \\ \alpha & 1 \end{bmatrix} \begin{pmatrix} x \\ y \end{pmatrix} \tag{I.8}$$

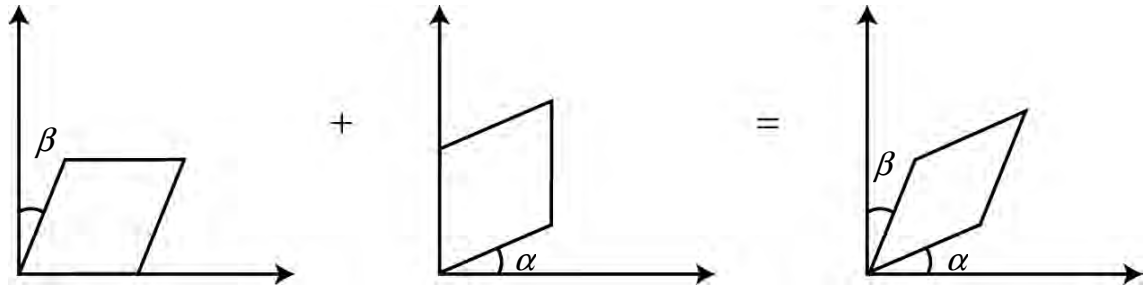

(a) (b) (c)

FIG. I-2. Distortion of a Fluid Element By Pure Shear Strain-rate

The reason neglecting $\alpha\beta$ is that α and β are small, so $\alpha\beta$ approaches zero. Thus the shear strain-rate is equal to

$$2a_{12} = 2a_{21} = \alpha + \beta \tag{I.9}$$

From Fig.I.1, α and β are defined as

$$\alpha \approx \tan(\alpha) = \frac{\frac{\partial v}{\partial x} dx}{dx + \frac{\partial u}{\partial x} dx} \approx \frac{\partial v}{\partial x} \tag{I.10}$$

$$\beta \approx \tan(\beta) = \frac{\frac{\partial u}{\partial y} dy}{dy + \frac{\partial v}{\partial y} dy} \approx \frac{\partial u}{\partial y} \tag{I.11}$$

By substituting (I.10) and (I.11) into (I.9), shear strain-rate is defined as a

$$a_{12} = a_{21} = \frac{1}{2}\left(\frac{\partial v}{\partial x} + \frac{\partial u}{\partial y}\right) \tag{I.12}$$

The derivation of antisymetric vorticity is achieved by considering the pure rotation of a fluid element presented Fig. I.3. This shows a fluid element change its orientation without any normal and shear strain-rate. Transformations of a) and b) in Fig. I.3 are achieved by

$$\begin{pmatrix} x' \\ y' \end{pmatrix} = \begin{bmatrix} 1 & \alpha \\ 0 & 1 \end{bmatrix} \begin{pmatrix} x \\ y \end{pmatrix} \text{ and } \begin{pmatrix} x' \\ y' \end{pmatrix} = \begin{bmatrix} 1 & 0 \\ -\alpha & 1 \end{bmatrix} \begin{pmatrix} x \\ y \end{pmatrix} \tag{I.13}$$

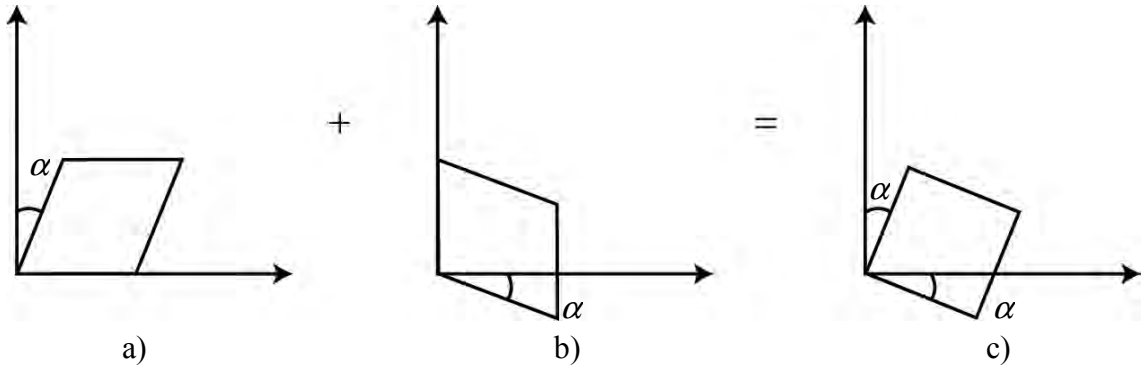

FIG. I-3. Fluid Element Orientation by Pure Rotation Strain-rate

The multiplication (I.13) defines c) in Fig. I-3, and expressed as a

$$\begin{pmatrix} x' \\ y' \end{pmatrix} = \begin{bmatrix} 1 & \alpha \\ -\alpha & 1 \end{bmatrix} \begin{pmatrix} x \\ y \end{pmatrix} \tag{I.14}$$

By (I.10) and (I.11) antisymmetric vorticity for Fig. I-1 is expressed as a

$$\omega_{12} = -\omega_{21} = \frac{1}{2}\left(\frac{\partial u}{\partial y} - \frac{\partial v}{\partial x}\right) \tag{I.15}$$

By substituting (I.7), (I.12) and (I.15) into (I.6) velocity gradient matrix which describe relative motion or distortion of a fluid element is obtained as a

$$\begin{bmatrix} \frac{\partial u}{\partial x} & \frac{\partial u}{\partial y} \\ \frac{\partial v}{\partial x} & \frac{\partial v}{\partial y} \end{bmatrix} = \begin{bmatrix} \frac{\partial u}{\partial x} & \frac{1}{2}\left(\frac{\partial v}{\partial x}+\frac{\partial u}{\partial y}\right) \\ \frac{1}{2}\left(\frac{\partial v}{\partial x}+\frac{\partial u}{\partial y}\right) & \frac{\partial v}{\partial y} \end{bmatrix} + \begin{bmatrix} 0 & \frac{1}{2}\left(\frac{\partial u}{\partial y}-\frac{\partial v}{\partial x}\right) \\ \frac{1}{2}\left(\frac{\partial v}{\partial x}-\frac{\partial u}{\partial y}\right) & 0 \end{bmatrix} \tag{I.16}$$

By introducing index notation, (I.16) can be expressed into

$$u_{i,j} = \frac{1}{2}\left(u_{i,j} + u_{j,i}\right) + \frac{1}{2}\left(u_{i,j} - u_{j,i}\right) \tag{I.17}$$

where *i* and *j* indicate coordinate direction indicies, the left hand side equation represents the velocity gradient tensor, the first right hand side equation is termed symmetric strain-rate tensor and the second equation of right hand side is the vorticity tensor.

APPENDIX II

Strain-Rate Derivation

It is known that tensor equations are valid in any generalized coordinate system. However, in order to express physical phenomena, which are invariant and independent of the coordinate system, tensor equations must be expanded with proper physical components. From Appendix I, strain-rate tensor is defined as a

$$a_{ij} = \frac{1}{2}(u_{i,j} + u_{j,i}) \tag{II.1}$$

With the covariant components to velocity vector strain-rate tensor, (II.1), is expresses as a

$$a_{ij} = \frac{1}{2}(g_{it}u^t_{,j} + g_j u^t_{,i}) \tag{II.2}$$

By assuming an orthogonal coordinate system, a metric tensor that indicates the distance between any two points in a certain space is defined as a

$$g_{ij} = g_{ii}\delta_{ij} = h_i^2\delta_{ij} \tag{II.3}$$

where h_i is scale factor and δ_{ij} is the Kroneck delta. Before using any expanded tensor equations all the tensor components must be replaced by their corresponding physical components in order to make the homogeneous dimension. The physical components, $T(ij)$, associated with the second order tensor, T_{ij}, can be represented

$$T(ij) = \frac{T_{ij}}{h_i h_j} \tag{II.4}$$

and the physical components of velocity is expressed as a

$$u(i) = h_i u^i \qquad \textit{no summation on } i \tag{II.5}$$

Then, normal strain-rate, a_{ii}, and shear strain-rate tensor, a_{ij}, are defined

$$a_{ii} = g_{it}\left[\frac{\partial u^t}{\partial x^i} + \begin{Bmatrix} t \\ mi \end{Bmatrix} u^m\right] \quad \textit{no summation on } i \tag{II.6}$$

$$2a_{ij} = g_{it}\frac{\partial u^t}{\partial x^j} + g_{jt}\frac{\partial u^t}{\partial x^i} \qquad i \neq j \tag{II.7}$$

By substituting physical components, (II.4) and (II.5) into (II.6) and (II.7), the expanded strain-rate tensor equations which are valid in any generalized two-dimensional coordinate system are defined as

$$2a_{ij} = \frac{h_i}{h_j}\frac{\partial}{\partial j}\left(\frac{u_i}{h_i}\right) + \frac{h_j}{h_i}\frac{\partial}{\partial i}\left(\frac{u_j}{h_j}\right) \quad \textit{no summation on } i \textit{ or }, j \;\; i \neq j \tag{II.8}$$

$$a_{ii} = \frac{\partial}{\partial x_i}\left(\frac{u_i}{h_i}\right) + \frac{1}{2h_i^2}\sum_{m=i,j}\frac{u_m}{h_m}\frac{\partial}{\partial m}(h_i^2) \; \textit{no summation on } i \tag{II.9}$$

For Example, with equations, (II-8) and (II-9), strain-rate tensors on Cartesian, polar and bipolar coordinates can be defined.

1. Catesian coordinates (x, y)

The scale factors for the Cartesian coordinates, when, $i = x$ and $j = y$, are given as

$$h_x = h_y = 1 \tag{II.10}$$

By substituting (II.10) into (II.8) and (II.9), shear (a_{xy}) and normal (a_{xx} and a_{yy}) strain-rate are defined as

$$a_{xx} = \frac{\partial}{\partial x}\left(\frac{u_x}{h_x}\right) + \frac{1}{2h_x^2}\sum_{m=x,y}\frac{u_m}{h_m}\frac{\partial}{\partial m}(h_x)^2 = \frac{\partial}{\partial x}\left(\frac{u_x}{1}\right) + \frac{1}{2}\sum_{m=x,y}\frac{u_m}{h_m}\frac{\partial}{\partial m}(1)^2 = \frac{\partial u_x}{\partial x} \quad \text{(II.11)}$$

$$a_{yy} = \frac{\partial}{\partial y}\left(\frac{u_y}{h_y}\right) + \frac{1}{2h_y^2}\sum_{m=x,y}\frac{u_m}{h_m}\frac{\partial}{\partial m}(h_y)^2 = \frac{\partial}{\partial y}\left(\frac{u_y}{1}\right) + \frac{1}{2}\sum_{m=x,y}\frac{u_m}{h_m}\frac{\partial}{\partial m}(1)^2 = \frac{\partial u_y}{\partial y} \quad \text{(II.12)}$$

$$2a_{xy} = \frac{h_x}{h_y}\frac{\partial}{\partial y}\left(\frac{u_x}{h_x}\right) + \frac{h_y}{h_x}\frac{\partial}{\partial x}\left(\frac{u_y}{h_y}\right) = \frac{1}{1}\frac{\partial}{\partial y}\left(\frac{u_x}{1}\right) + \frac{1}{1}\frac{\partial}{\partial x}\left(\frac{u_y}{1}\right) = \frac{\partial u_x}{\partial y} + \frac{\partial u_y}{\partial x} \quad \text{(II.13)}$$

The matrix form of strain-rate is expressed as a

$$E = \begin{bmatrix} \dfrac{\partial u_x}{\partial x} & \dfrac{1}{2}\left(\dfrac{\partial u_y}{\partial x} + \dfrac{\partial u_x}{\partial y}\right) \\ \dfrac{1}{2}\left(\dfrac{\partial u_y}{\partial x} + \dfrac{\partial u_x}{\partial y}\right) & \dfrac{\partial u_y}{\partial y} \end{bmatrix} \quad \text{(II.14)}$$

(II. 14) is corresponding to strain-rate tensor, equation (3). Therefore, the expanded strain-rate tensor equations generalized for any two-dimensional coordinate system are valid.

2. Polar coordinates (r , θ)

The scale factors for the polar coordinates, when, $i = r$ and $j = \theta$, are given

$$h_r = 1,\ h_\theta = r \quad \text{(II.15)}$$

By substituting (II.15) into (II.8) and (II.9), shear ($a_{r\theta}$) and normal (a_{rr} and $a_{\theta\theta}$) strain-rate are defined as

$$a_{rr} = \frac{\partial}{\partial r}\left(\frac{u_r}{h_r}\right) + \frac{1}{2h_r^2}\sum_{m=r,\theta}^{3}\frac{u_m}{h_m}\frac{\partial}{\partial m}(h_r^2) = \frac{\partial}{\partial r}\left(\frac{u_r}{1}\right) + \frac{1}{2}\sum_{m=r,\theta}\frac{u_m}{h_m}\frac{\partial}{\partial m}(1)^2 = \frac{\partial u_r}{\partial r} \qquad \text{(II.16)}$$

$$a_{\theta\theta} = \frac{\partial}{\partial \theta}\left(\frac{u_\theta}{h_\theta}\right) + \frac{1}{2h_\theta^2}\sum_{m=r,\theta}\frac{u_\theta}{h_m}\frac{\partial}{\partial m}(h_\theta^2) = \frac{\partial}{\partial \theta}\left(\frac{u_\theta}{r}\right) + \frac{1}{2r^2}\sum_{m=r,\theta}\frac{u_m}{h_m}\frac{\partial}{\partial m}(r)^2 = \frac{1}{r}\frac{\partial u_\theta}{\partial \theta} + \frac{u_r}{r}$$

(II.17)

$$2a_{r\theta} = \frac{h_{r1}}{h_\theta}\frac{\partial}{\partial \theta}\left(\frac{u_r}{h_r}\right) + \frac{h_\theta}{h_r}\frac{\partial}{\partial r}\left(\frac{u_\theta}{h_\theta}\right) = \frac{1}{r}\frac{\partial u_r}{\partial \theta} + \frac{r}{1}\frac{\partial}{\partial r}\left(\frac{u_\theta}{r}\right) = \frac{1}{r}\frac{\partial u_r}{\partial \theta} + r\left(\frac{1}{r}\frac{\partial u_\theta}{\partial r} - \frac{u_\theta}{r^2}\right)$$

(II.18)

$$E = \begin{bmatrix} \dfrac{\partial u_r}{\partial r} & \dfrac{1}{2}\left(\dfrac{1}{r}\dfrac{\partial u_r}{\partial r} + r\left(\dfrac{1}{r}\dfrac{\partial u_\theta}{\partial r} - \dfrac{u_\theta}{r^2}\right)\right) \\ \dfrac{1}{2}\left(\dfrac{1}{r}\dfrac{\partial u_r}{\partial r} + r\left(\dfrac{1}{r}\dfrac{\partial u_\theta}{\partial r} - \dfrac{u_\theta}{r^2}\right)\right) & \dfrac{1}{r}\dfrac{\partial u_\theta}{\partial \theta} + \dfrac{u_r}{r} \end{bmatrix} \qquad \text{(II.19)}$$

3. Bipolar coordinates (ξ, η)

The scale factors for the bipolar coordinates, when, $i = \xi$ and $j = \eta$, are given

$$h_\xi = h_\eta = \frac{b^2}{(\cosh(\xi) - \cos(\eta))^2} \qquad \text{(II.20)}$$

By substituting (II-19) into (II-8) and (II-9), shear ($a_{\xi\eta}$) and normal ($a_{\eta\eta}$ and $a_{\xi\xi}$) strain-rate are defined as

$$a_{\xi\xi} = \frac{\partial}{\partial \xi}\left(\frac{u_\xi}{h_\xi}\right) + \frac{1}{2h_\xi^2}\sum_{m=\xi,\eta}\frac{u_m}{h_m}\frac{\partial}{\partial m}(h_\xi^2) = \frac{\partial}{\partial \xi}\left(\frac{u_\xi}{h_\xi}\right) + \frac{1}{2h_\xi{}^2}\left(\frac{u_\xi}{h_\xi}\frac{\partial}{\partial \xi}(h_\xi^2) + \frac{u_\eta}{h_\eta}\frac{\partial}{\partial \eta}(h_\xi^2)\right)$$

(II.21)

$$a_{\eta\eta} = \frac{\partial}{\partial \eta}\left(\frac{u_\eta}{h_\eta}\right) + \frac{1}{2h_\eta^2}\sum_{m=\xi,\eta}\frac{u_m}{h_m}\frac{\partial}{\partial m}(h_\eta^2) = \frac{\partial}{\partial \eta}\left(\frac{u_\eta}{h_\eta}\right) + \frac{1}{2h_\eta^2}\left(\frac{u_\xi}{h_\xi}\frac{\partial}{\partial \xi}(h_\eta^2) + \frac{u_\eta}{h_\eta}\frac{\partial}{\partial \eta}(h_\eta^2)\right)$$

(II.22)

$$2a_{\xi\eta} = \frac{h_\xi}{h_\eta}\frac{\partial}{\partial \eta}\left(\frac{u_\xi}{h_\xi}\right) + \frac{h_\eta}{h_\xi}\frac{\partial}{\partial \xi}\left(\frac{u_\eta}{h_\eta}\right) = \frac{\partial}{\partial \eta}\left(\frac{u_\xi}{h_\xi}\right) + \frac{\partial}{\partial \xi}\left(\frac{u_\eta}{h_\eta}\right) \qquad \text{(II.23)}$$

$$E = \begin{bmatrix} \frac{\partial}{\partial \xi}\left(\frac{u_\xi}{h_\xi}\right) + \frac{1}{2h_\xi^2}\left(\frac{u_\xi}{h_\xi}\frac{\partial}{\partial \xi}\left(h_\xi^2\right) + \frac{u_\eta}{h_\eta}\frac{\partial}{\partial \eta}\left(h_\xi^2\right)\right) & \frac{1}{2}\left(\frac{\partial}{\partial \eta}\left(\frac{u_\xi}{h_\xi}\right) + \frac{\partial}{\partial \xi}\left(\frac{u_\eta}{h_\eta}\right)\right) \\ \frac{1}{2}\left(\frac{\partial}{\partial \eta}\left(\frac{u_\xi}{h_\xi}\right) + \frac{\partial}{\partial \xi}\left(\frac{u_\eta}{h_\eta}\right)\right) & \frac{\partial}{\partial \eta}\left(\frac{u_\eta}{h_\eta}\right) + \frac{1}{2h_\eta^2}\left(\frac{u_\xi}{h_\xi}\frac{\partial}{\partial \xi}\left(h_\eta^2\right) + \frac{u_\eta}{h_\eta}\frac{\partial}{\partial \eta}\left(h_\eta^2\right)\right) \end{bmatrix}$$

(II.24)

APPENDIX III

Analytical Solutions for The Eccentric Rotating Cylinder Apparatus

Since two-dimensional momentum equations (28) and (29) cannot be linearized in Cartesian coordinates, Ballal and Rivlin (1976) adopted the bipolar coordinates. Transformation of the Cartesian coordinates (*x, y*) into the bipolar coordinates (ξ, η) can be expressed as

$$x = -b\frac{\sinh\xi}{\cosh\xi - \cos\eta}, \qquad y = b\frac{\sin\eta}{\cosh\xi - \cos\eta} \tag{III-1}$$

The geometry transformation is shown in Fig. III-1. The Euclidean cylindrical coordinates R and θ were transformed into an equivalent complex coordinate system. Boundary conditions are $\xi = \xi_o$ on the outer cylinder, and $\xi = \xi_i$ on the inner cylinder, where ξ_i and ξ_o are negatively valued constants the geometric characteristics of eccentric rotating cylinder such as outer cylinder radius, R_o, inner cylinder radius, R_i, eccentricity, e, and clearance, c, are defined

$$R_o = \frac{-b}{\sinh(\xi_o)} \tag{III-2}$$

$$R_i = \frac{-b}{\sinh(\xi_i)} \tag{III-3}$$

$$c = -b\coth(\xi_o) \tag{III-4}$$

$$e = -b\left(\coth\xi_o - \coth\xi_i\right) \tag{III-5}$$

where b is the distance between O and P in Fig. 12 and given by

$$b = \frac{1}{2e}\sqrt{\left(R_o^2 + R_i^2 - e^2\right) - 4R_o^2 R_i^2} \tag{III-6}$$

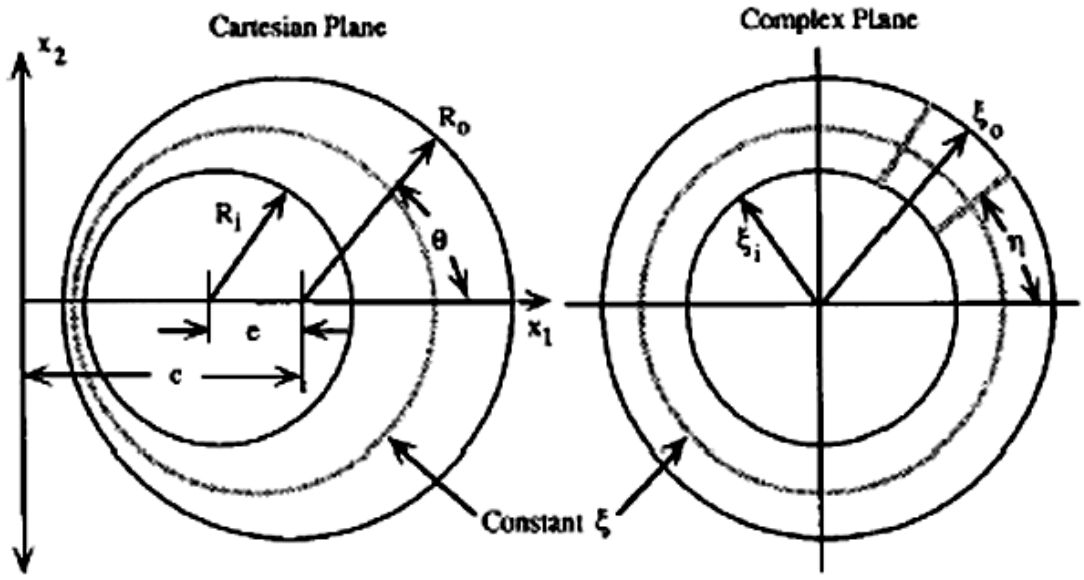

FIG. III-1. Eccentric device in Euclidean (cylindrical) and complex coordinates (Kramer and Clark, 1997)

To solve biharmonic equation for Stokes stream function with complex coordinates, Laplace operator must be defined in bipolar coordinates.

$$\nabla^2 = \frac{1}{h^2}\left(\frac{\partial^2}{\partial \xi^2} + \frac{\partial^2}{\partial \eta^2}\right) \tag{III-7}$$

where *h* is defined as

$$h_\eta = h_\xi = h = \frac{b}{\cosh(\xi) - \cos(\eta)} \tag{III-8}$$

Then, biharmonic equation, (33), is rewritten as a

$$\nabla^2\left(\nabla^2\psi^{(0)}\right)=\frac{1}{h^2}\left(\frac{\partial^2}{\partial\xi^2}+\frac{\partial^2}{\partial\eta^2}\right)\left(\frac{1}{h^2}\left(\frac{\partial^2\psi^{(0)}}{\partial\xi^2}+\frac{\partial^2\psi^{(0)}}{\partial\eta^2}\right)\right)=0 \qquad \text{(III-9)}$$

For the case inner cylinder stationary and out cylinder rotating, the boundary conditions are

$$\psi^{(0)}=0 \text{ and } \frac{\partial\psi^{(0)}}{\partial\xi_i}=0 \text{ on inner cylinder} \qquad \text{(III-10)}$$

$$\psi^{(0)}=\overline{\psi} \text{ and } \frac{\partial\psi^{(0)}}{\partial\xi_o}=-R_o\omega_o h \text{ on outer cylinder} \qquad \text{(III-11)}$$

where $\overline{\psi}$ is a function of the radius of the inner cylinder, radius of the outer cylinder and angular velocity.

$$\overline{\psi}=\frac{b\overline{\delta}}{\overline{\overline{\delta}}}\left(h_1\omega_o R_o\right) \qquad \text{(III-12)}$$

where $\overline{\delta}$ and $\overline{\overline{\delta}}$ are defined in (III-19).

The solution of the Stokes stream functions neglecting the inertial forces can be expressed as

$$\psi^{(0)}=h\phi^{(0)} \qquad \text{(III-13)}$$

where $\phi^{(0)}$ is function which depend on the eccentricity, e, radius ratio, R_i/R_o, and outer cylinder angular velocity, ω_o and given as a

$$\phi^{(0)}=F_0(\xi)+F_1(\xi)\cos(\eta) \qquad \text{(III-14)}$$

where

$$F_0(\xi)=(A_0+C_0\xi)\cosh(\xi)+(B_0+D_0\xi)\sinh(\xi)$$

$$F_1(\xi)=A_1\cosh(2\xi)+B_1\sinh(2\xi)+C_1\xi+D_1$$

$$(A_0, B_0, C_0, D_0) = (f_1, f_3, f_5, f_7)\omega_o R_o$$

$$(A_1, B_1, C_1, D_1) = (f_9, f_{11} - f_5, f_{13})\omega_o R_o$$

with

$$f_1 = \frac{1}{\delta}\left(\frac{\bar{\delta}}{\bar{\bar{\delta}}} h_1 h_7 + h_3\right)$$

$$f_3 = \frac{1}{\delta}\left(\frac{\bar{\delta}}{\bar{\bar{\delta}}} h_1 h_8 + h_5\right)$$

$$f_5 = \frac{h_1}{\bar{\bar{\delta}}}\cosh(\xi_1 - \xi_2)$$

$$f_7 = -\frac{\sinh A_2}{\bar{\bar{\delta}}} \times \sinh^2(\xi_1 - \xi_2)$$

$$f_9 = -\frac{h_1}{2\bar{\bar{\delta}}}\sinh(\xi_1 + \xi_2)$$

$$f_{11} = \frac{h_1}{2\bar{\bar{\delta}}}\cosh(\xi_1 + \xi_2)$$

$$f_{13} = \frac{h_1}{2\bar{\bar{\delta}}}\left(\sinh(\xi_1 - \xi_2) + 2\xi_2 \cosh(\xi_1 + \xi_2)\right) \qquad \text{(III-15)}$$

and

$$\delta = (\xi_1 - \xi_2)^2 - \sinh^2(\xi_1 - \xi_2) < 0$$

$$\bar{\delta} = (\xi_1 - \xi_2)\cosh(\xi_1 - \xi_2) - \sinh(\xi_1 - \xi_2) > 0$$

$$\bar{\bar{\delta}} = \sinh(\xi_1 - \xi_2)\left(2\sinh\xi_1 \sinh\xi_2 \sinh(\xi_1 - \xi_2) - (\xi_1 - \xi_2)(\sinh^2\xi_1 + \sinh^2\xi_2)\right) < 0$$

$$h_1 = (\xi_1 - \xi_2)\sinh(\xi_1) - \sinh(\xi_2)\sinh(\xi_1 - \xi_2) > 0$$

$$h_3 = \xi_1 \sinh(\xi_2)\sinh(\xi_1 - \xi_2) - \xi_2(\xi_1 - \xi_2)\sinh(\xi_1) > 0$$

$$h_5 = -\xi_1 \cosh(\xi_2)\sinh(\xi_1-\xi_2) + \xi_2(\xi_1-\xi_2)\cosh(\xi_1)$$

$$h_7 = \sinh(\xi_2)\cosh(\xi_1)\sinh(\xi_1-\xi_2) + \frac{1}{2}\xi_1 \sinh(2\xi_2) - \frac{1}{2}\xi_2 \sinh(2\xi_1) - \xi_2(\xi_1-\xi_2) > 0$$

$$h_8 = -\cosh(\xi_1)\cosh(\xi_2)\sinh(\xi_1-\xi_2) + \xi_2 \cosh^2(\xi_1) - \xi_1 \cosh^2(\xi_2) \qquad \text{(III-16)}$$

For the case of governing inertial forces, (36) must be rewritten in bipolar coordinates. Transformation of (36) and its boundary conditions (37) with (46) and (48) in bipolar coordinates, are defined as

$$\nabla^4 \psi^{(1)} = \frac{1}{h^4}\left(\psi_\eta^{(0)}\frac{\partial}{\partial\xi} - \psi_\xi^{(0)}\frac{\partial}{\partial\eta}\right)\left(\frac{\partial^2\psi^{(0)}}{\partial\xi} + \frac{\partial^2\psi^{(0)}}{\partial\eta}\right) \qquad \text{(III-17)}$$

Then, inertial stream function is defined as

$$\psi^{(1)} = h\phi^{(1)} \qquad \text{(III-18)}$$

where $\phi^{(1)}$ is also function which depend on the rate of eccentricity, *e*, radius ratio, R_i/R_o, and outer cylinder angular velocity, ω_o and defined as a

$$\phi^{(1)}(\xi,\eta) = 2b\sum_{n=1}^{\infty} G_n(\xi)\sin(n\eta) \qquad \text{(III-19)}$$

with

$$G_1(\xi) = -\frac{1}{4}\int_{\xi_o}^{\xi}\int_{\xi_o}^{\xi}\overline{g}_1(\xi)d\xi d\xi + \frac{1}{8}\sinh(2\xi)\int_{\xi_o}^{\xi}\overline{g}_1(\xi)\cosh(2\xi)d\xi - \frac{1}{8}\cosh(2\xi)\int_{\xi_o}^{\xi}\overline{g}_1(\xi)\sinh(2\xi)d\xi$$
$$+\frac{1}{2}\sinh^2(\xi-\xi_i)G_1''(\xi_i) - \frac{1}{8}\left(2(\xi-\xi_i) - \sinh 2(\xi-\xi_i)\right)G_1'''(\xi_i)$$
$$G_n(\xi) = \frac{1}{4n}\sum_{v=\pm1}\frac{-v}{n-v}\{\sinh((n-v)\xi)\int_{\xi_i}^{\xi}\overline{g}_n(\xi)\cosh(n-v)\xi d\xi$$

$$(n-v)\cosh((n-v)(\xi-\xi_i))G_n''(\xi_2) + \sinh((n-v)(\xi-\xi_2))G_n'''(\xi_i)\} \qquad \text{(III-20)}$$

where $g_n(\xi)$ (n = 1,2,3,4) are given by

$$g_1(\xi) = P_1'(F_0\sinh(\xi) - F_0'\cosh(\xi) + \frac{1}{4}F_1') - P_2(F_0 + F_1\cosh(\xi)) + \frac{1}{2}P_2'(F_0' + F_1\sinh(\xi) - F_1'\cosh(\xi))$$

$$g_2(\xi) = \frac{1}{2}P_1(F_0 + F_1\cosh(\xi)) + \frac{1}{2}P_1'(F_0' + F_1\sinh(\xi) - F_1'\cosh(\xi)) + P_2'(\frac{1}{2}F_1' + F_0\sinh(\xi) F_0'\cosh(\xi))$$

$$g_3(\xi) = \frac{1}{4}P_1'F_1' + P_2(F_0 + F_1\cosh(\xi)) + \frac{1}{2}P_2'(F_0' + F_1\sinh(\xi) - F_1'\cosh(\xi))$$

$$g_4(\xi) = \frac{1}{4}P_2'F_1'$$

$$G_1''(\xi_2) = \frac{1}{2\bar{\delta}}\left\{\frac{1}{2}\left[\frac{(\xi_1-\xi_2)\sinh(2\xi_1)}{\sinh(\xi_1-\xi_2)} - \sinh(\xi_1+\xi_2)\right]\int_{\xi_2}^{\xi_1}\tilde{g}_1(\xi)\sinh(2\xi)d\xi - \frac{1}{2}\left[\frac{(\xi_1-\xi_2)\cosh(2\xi_1)}{\sinh(\xi_1-\xi_2)} - \cosh(\xi_1+\xi_2)\right]\int_{\xi_2}^{\xi_1}\tilde{g}_1(\xi)\cosh(2\xi)d\xi - \sinh(\xi_1-\xi_2)\int_{\xi_2}^{\xi_1}\xi\tilde{g}_1(\xi)d\xi\right\}$$

$$G_1'''(\xi_2) = \frac{1}{2\bar{\delta}}\left\{\sinh(\xi_1+\xi_2)\int_{\xi_2}^{\xi_1}\tilde{g}_1(\xi)\cosh(2\xi)d\xi - \cosh(\xi_1+\xi_2)\int_{\xi_2}^{\xi_1}\tilde{g}_1(\xi)\sinh(2\xi)d\xi + 2\cosh(\xi_1-\xi_2)\int_{\xi_2}^{\xi_1}\xi\tilde{g}_1(\xi)d\xi\right\}$$

$$G_n''(\xi_2) = \frac{1}{2(n-1)\delta_n}\{[\sinh(n(\xi_1-\xi_2))\cosh(n\xi_1-\xi_2) - n\cosh((n-1)\xi_1)\sinh((n+1)(\xi_1-\xi_2)$$
$$+ n^2\sinh(\xi_1-\xi_2)\cosh(\xi_1-n\xi_2)]\int_{\xi_2}^{\xi_1}\widetilde{g}_n(\xi)\cosh((n-1)\xi)d\xi$$
$$-[\sinh(n(\xi_1-\xi_2))\sinh(n\xi_1-\xi_2) - n\sinh((n-1)\xi_1\sinh((n+1)(\xi_1-\xi_2))$$
$$-n^2\sinh(\xi_1-\xi_2)\sinh(\xi_1-n\xi_2)]\int_{\xi_2}^{\xi_1}\widetilde{g}_n(\xi)\sinh((n-1)\xi)d\xi$$
$$-(n-1)[n\sinh(\xi_1-\xi_2)\cosh((\xi_1+n\xi_2) - \sinh(n(\xi_1-\xi_2))\cosh(n\xi_1+\xi_2)]$$
$$\int_{\xi_2}^{\xi_1}\widetilde{g}_n(\xi)\cosh((n+1)\xi)d\xi + (n-1)[n\sinh(\xi_1-\xi_2)\sinh(\xi_1+n\xi_2)$$
$$-\sinh(n(\xi_1-\xi_2))\sinh(n\xi_1+\xi_2)]\int_{\xi_2}^{\xi_1}\widetilde{g}(\xi)\sinh((n+1)\xi)d\xi\Big\}, \qquad (n\geq 2)$$

$$G_n'''(\xi_2) = \frac{1}{2\delta_n}\{[\sinh(n(\xi_1-\xi_2)\sinh(n\xi_1-\xi_2) + n\sinh((n-1)\xi_1)\sinh((n+1)(\xi_1-\xi_2))$$
$$-n^2\sinh(\xi_1-\xi_2)\sinh(\xi_1-n\xi_2)]\int_{\xi_2}^{\xi_1}\widetilde{g}_n(\xi)\cosh((n-1)\xi)d\xi$$
$$-[\sinh(n(\xi_1-\xi_2))\cosh(n\xi_1-\xi_2) + n\cosh((n-1)\xi_1)\sinh((n+1)(\xi_1-\xi_2))$$
$$+n^2\sinh(\xi_1-\xi_2)\cosh(\xi_1-n\xi_2)]\int_{\xi_2}^{\xi_1}\widetilde{g}_n(\xi)\sinh((n-1)\xi)d\xi$$
$$-(n-1)[n\sinh(\xi_1-\xi_2)\sinh(\xi_1+n\xi_2)$$
$$+\sinh(n(\xi_1-\xi_2))\sinh(n\xi_1+\xi_2)]\int_{\xi_2}^{\xi_1}\widetilde{g}_n(\xi)\cosh((n+1)\xi)d\xi$$
$$+(n-1)[n\sinh(\xi_1-\xi_2)\cosh(\xi_1+n\xi_2)$$
$$+\sinh(n(\xi_1-\xi_2))\cosh(n\xi_1+\xi_2)]\int_{\xi_2}^{\xi_1}\widetilde{g}_n(\xi)\sinh((n+1)\xi)d\xi\Big\}, \quad (n\geq 2)$$

where

$$\delta_n = n^2\sinh^2(\xi_1-\xi_2) - \sinh^2(n(\xi_1-\xi_2)) < 0, \qquad (n\geq 2)$$

$$\widetilde{g}_1(\xi) = -\frac{1}{\sinh^2(\xi)} \sum_{m=1}^{4} m e^{m\xi} (\coth(\xi) - m) g_m(\xi)$$

$$\begin{aligned} \widetilde{g}_n &= \frac{e^{n\xi}}{\sinh^3(\xi)} \sum_{m=1}^{4} \Big\{ \big[3\coth(\xi)(\coth(\xi) - n) + m^2 + n^2 - 1 \big] \sinh(m\xi) \\ &= m(3\coth(\xi) - 2n)\cosh(m\xi) \Big\} g_m(\xi), \qquad (n \geq 2) \end{aligned} \tag{III-21}$$

VITA

Chun Woo Lee was born on February 9, 1974 in a small town called Young-Chun, Korea. He received his B.S. in environmental engineering from Pukyung National University, Pusan, Korea. He worked as a research and teaching assistant at Pukyung National University from April 1999 to February 2000. He received his M.S. in civil engineering from Texas A&M University in August 2003

The author can be contacted at the following mail address:

1057-17 Gu-Il Apt # 1-206

Jae-Song 2 Dong, Hae-Un-Dae Gu, Pusan, Korea, 612-052

chunwoolee@neo.tamu.edu